Tino Wagner

High-resolution Kelvin probe force microscopy of active nanoelectronic devices

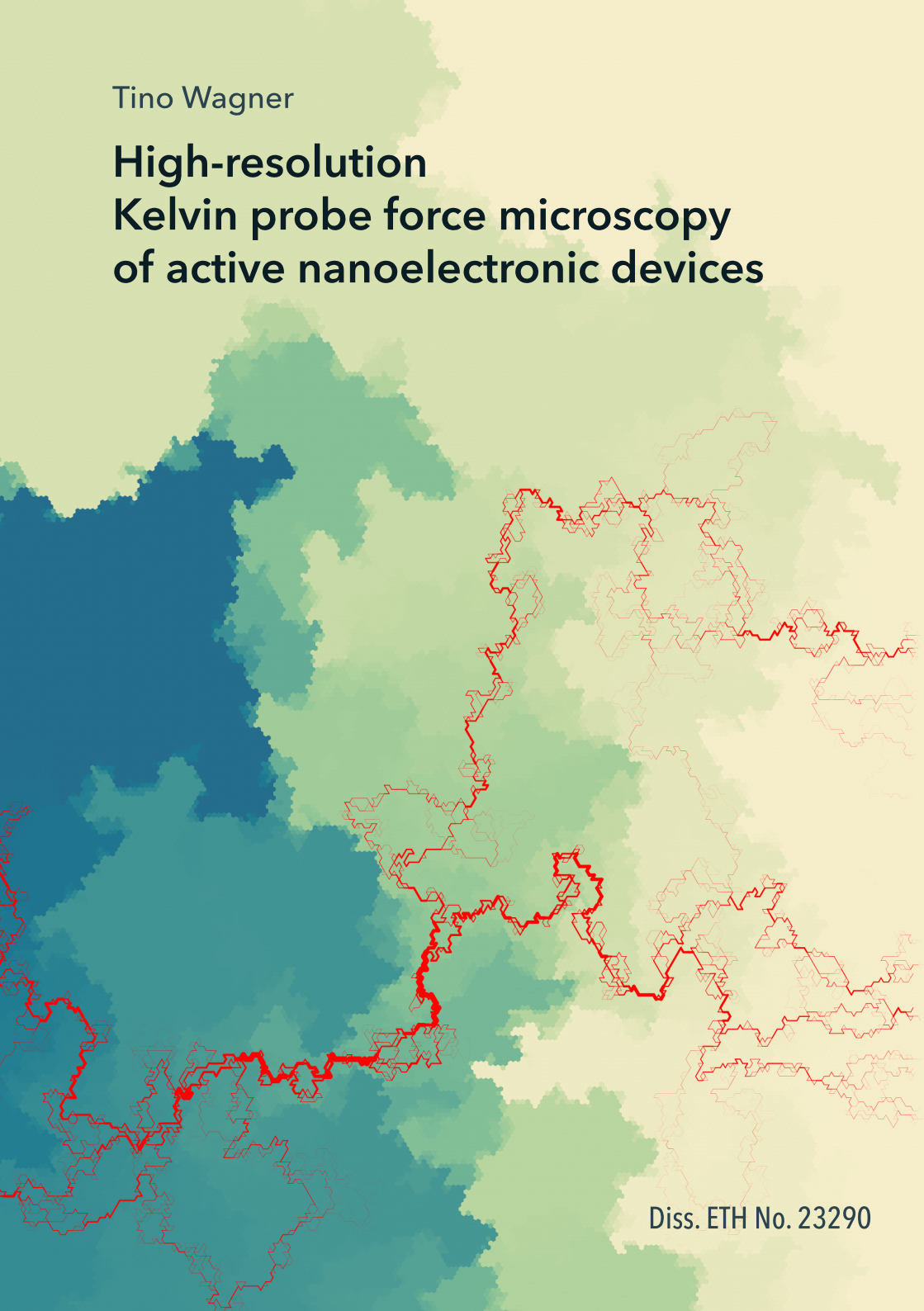

Diss. ETH No. 23290

TINO WAGNER

HIGH-RESOLUTION KELVIN PROBE FORCE MICROSCOPY OF ACTIVE NANOELECTRONIC DEVICES

DISS. ETH NO. 23290

HIGH-RESOLUTION KELVIN PROBE FORCE MICROSCOPY OF ACTIVE NANOELECTRONIC DEVICES

A dissertation submitted to attain the degree of

DOCTOR OF SCIENCES of ETH ZURICH
(Dr. sc. ETH Zurich)

presented by

TINO WAGNER
Dipl.-Phys., Technische Universität Dresden

born on 6 October 1986
citizen of Germany

accepted on the recommendation of

Prof. Dr. Andreas Stemmer, examiner
Dr. Bernd Gotsmann, co-examiner

2016

DOI: 10.3929/ethz-a-010615234

Für Mama

ABSTRACT

As electronic devices, such as transistors in integrated circuits, continue to shrink, contact resistances and local transport properties dictate device performance on a length scale of only a few nanometres. Characterisation is severely limited by macroscopic methods, which measure the total current through a device only. It has rather become necessary to accurately determine local electronic properties and potentials within devices at nanometre spatial resolution and high sensitivity.

This challenge is tackled in this thesis by Kelvin probe force microscopy, in which electrostatic forces exerted on a microfabricated cantilever with a probe tip are detected and minimised to yield the surface potential. In the past, most researchers applied force sensitive techniques for better stability on coarse topographic structures as in nanoscale electronic devices. Yet, the detection of long-range electrostatic forces also degrades resolution, and local surface potential measurements are corrupted by biased electrodes even at large distances to the probe. In contrast, frequency modulated methods are sensitive to force gradients and enable quantitative measurements with minimised long-range effects. The interactions of the probe apex thereby dominate the signal. However, the use of frequency modulated methods on structured surfaces was prone to instabilities in the past, because topography was detected in frequency modulation, too.

To enable highly resolved and quantitative investigations, a method to largely decouple surface potential measurements from topography was developed in this thesis. This is facilitated by direct detection of sidebands of the cantilever oscillation, which appear upon modulation of the force gradient. The transfer function governing the dynamics of these sidebands is discussed in detail, and it also proved useful for noise analysis. A novel Kelvin controller based on a Kalman filter was developed, capable of adjusting its sensitivity continuously during the measurement. Geometrical artefacts, introduced on structured surfaces due to varying probe–surface interactions, are mostly eliminated as a result. Surface potential and topography are acquired simultaneously for highest spatial resolution and sensitivity.

The advantages of the control scheme are demonstrated experimentally on indium arsenide nanowires. The surface potential along a wire was measured during sweeps of the current passing through the device, making it possible to determine the intrinsic channel resistance as well as individual contact resistances.

Furthermore, the local electronic properties of two-dimensional monolayers of 10-nm gold nanoparticles are investigated. Under bias condition, these nanoparticle

films exhibit a terrace-like surface potential landscape caused by structural disorder. Functional molecules in the nanometre-wide gaps of adjacent nanoparticles influence the conductivity of the nanoparticle network locally. The result of such molecular exchange protocols was visualised for the first time as part of this thesis. Individual nanoparticles are resolved in the surface potential, demonstrating the high resolution of the detection method.

Finally, the design and operation of a high-vacuum atomic force microscope is described in detail. The instrument is purpose-built for the characterisation of nanoscale electronic devices. In first measurements, the potential landscape of nanoporous fullerene networks could be resolved locally.

ZUSAMMENFASSUNG

Die fortschreitende Miniaturisierung elektronischer Bauelemente, wie beispielsweise von Transistoren in integrierten Schaltungen, hat zur Folge, dass Kontaktwiderstände sowie der lokale Ladungstransport auf einer Längenskala von nur wenigen Nanometern eine immer grössere Rolle spielen. Untersuchungsmethoden, die lediglich den Gesamtstrom durch ein Bauelement messen, stossen hier an ihre Grenzen. Es ist vielmehr notwendig geworden, den Potentialverlauf innerhalb der Bauelemente mit hoher Ortsauflösung und Empfindlichkeit zu bestimmen.

Innerhalb dieser Doktorarbeit wird hierzu die Kelvinsonden-Rasterkraftmikroskopie eingesetzt, bei der elektrostatische Kräfte, die auf einen mikrofabrizierten Federbalken mit Tastspitze wirken, detektiert und minimiert werden, um das Oberflächenpotential zu bestimmen. Auf strukturierten Oberflächen, wie dies bei elektronischen Bauelementen der Fall ist, wurde in der Vergangenheit üblicherweise auf kraftempfindliche Messmethoden zurückgegriffen. Durch die Empfindlichkeit auf langreichweitige Kräfte wird allerdings die Auflösung merklich beeinträchtigt. Lokale Potentialmessungen werden selbst in grösserer Entfernung zu spannungstragenden elektrischen Kontakten verfälscht. Hingegen ermöglichen frequenzmodulierte Methoden, empfindlich auf den Kraftgradienten, quantitative lokale Potentialmessungen ohne diese Effekte. Den Hauptanteil des Signals bilden damit lediglich die Wechselwirkungen der Messspitze nahe der Oberfläche. Allerdings war der Einsatz frequenzmodulierter Methoden auf strukturierten Oberflächen bisher sehr fehlerträchtig, da auch die Topographie frequenzmoduliert detektiert wurde.

Um dennoch hochaufgelöste quantitative Messungen zu ermöglichen, wurde im Rahmen dieser Arbeit eine Methode entwickelt, um Topographie- und Oberflächenpotentialmessungen weitestgehend zu entkoppeln. Dies wird ermöglicht durch die direkte Detektion der Seitenbänder, die bei einer Modulation des Kraftgradienten auftreten. Die Dynamik der Seitenbänder wird durch eine Transferfunktion beschrieben, die im Detail hergeleitet wird und sich als nützlich erweist, um etwa das Rauschverhalten zu analysieren. Ein neuartiger Kelvin-Regelkreis wurde entwickelt, der mittels eines Kalman-Filters stets seine Empfindlichkeit an die Messbedingungen anpasst. Geometrische Messartefakte, wie sie sonst auf strukturierten Oberflächen auftreten können, werden dadurch weitestgehend eliminiert. Messungen des Oberflächenpotentials finden zeitgleich mit den Topographiemessungen statt, um eine möglichst hohe Ortsauflösung zu erreichen.

An Indium-Arsenid-Nanodrähten werden die Vorteile des entwickelten Kelvin-Reglers experimentell aufgezeigt. Ebenfalls wurde bei verschiedenen Strömen das Oberflächenpotential entlang des Drahtes vermessen. Der intrinsische Widerstand des Kanals sowie einzelne Kontaktwiderstände werden hiermit als Funktion des Stromes zugänglich.

Als weitere aktive Nanostrukturen dienen zweidimensionale Monolagen kolloidaler Goldnanopartikel mit einem Durchmesser von 10 nm. Bei angelegter Spannung weisen diese Partikelfilme aufgrund struktureller Unordnung eine terrassenartige Potentiallandschaft auf. Durch die Integration funktionaler Moleküle in die nanometer-engen Zwischenräume benachbarter Partikel lässt sich die Leitfähigkeit des Partikelnetzwerks lokal beeinflussen. Die Auswirkungen eines solchen molekularen Austauschvorgangs wurden erstmals im Rahmen dieser Arbeit lokal sichtbar gemacht. Durch die hohe Ortsauflösung der verwendeten Messmethode können auch einzelne Partikel im Oberflächenpotential aufgelöst werden.

Abschliessend wird die Konstruktion eines Hochvakuum-Rasterkraftmikroskops beschrieben, das im Rahmen der Arbeit speziell zur Charakterisierung von aktiven Nanostrukturen entstanden ist. In ersten Messungen mit diesem Mikroskop konnte der Potentialverlauf in nanoporösen Fulleren-Netzwerken lokal aufgelöst werden.

ACKNOWLEDGEMENTS

This work would not have been possible without the continuous support, discussions, and encouragement from coworkers, collaborators, and friends.

I am deeply grateful to

- Prof. Dr. Andreas Stemmer, head of the Nanotechnology Group, for giving me the opportunity to work in his group, for his patience and guidance, and for always believing in me. I greatly appreciated the freedom he allowed me in pursuing own ideas and enjoyed the opportunity to also teach in his university course.
- Dr. Bernd Gotsmann at IBM Research in Rüschlikon, Switzerland, for his constant interest in the project, for stimulating discussions, and for agreeing to serve as a co-examiner of this thesis.
- my fellow PhD students and postdocs in the Nanotechnology Group: Hannes Beyer, Katharina Herkendell, Kristina Javor, Patrick Reissner, Dr. Khaled Kaja, Dr. Nassir Mojarad, Dr. Carlos Ruiz-Vargas, Dr. Jing-Hua Tian, Dr. Jean-Nicolas Tisserant. I really appreciated the friendly atmosphere and team spirit, as well as our activities outside work.
- our electronics engineer, Blerim Veselaj, for layout and assembly of the photodiode readout board, and for technical support.
- Hannes and Patrick for field tests of the Kalman-KFM controller on various samples.
- Patrick, for fabricating nanoparticle devices and performing the molecular exchange; Carlos, for device fabrication with graphene bottom contacts; Jing-Hua, for preparation of nanoparticle arrays with shadow mask electrodes; Khaled, for first joint experiments on these devices.
- Jean-Nicolas for preparation of the nanoporous C_{60} network, Dr. Yuriy Fedoryshyn (ETHZ) for e-beam lithography.
- Dr. Philipp Mensch (IBM) for fabrication of InAs nanowire devices.
- Dr. Fabian Menges (IBM) for joint design sessions on both our AFM setups.

– the IBM mechanical workshop for machining the custom parts of the high-vacuum AFM.

– Dr. Romain Stomp (Zurich Instruments) for joint first experiments on the frequency dependence of the sidebands, Daniel Wright (Zurich Instruments) for assistance with the real-time programming interface of the HF2 lock-in.

– financial support by the Swiss National Science Foundation (Project No. 134777).

Most of all, I am indebted to my parents, Gisela and Siegfried Wagner, for all their love and support up to this point in my life. Furthermore, I am grateful to my older siblings, René and Manuela, for their influence on me and letting me learn from their experiences. I also thank my soulmate, Nicole, for her love and all the wonderful moments we have shared.

CONTENTS

NOTATION

FREQUENTLY USED SYMBOLS

A, φ, X, Y	amplitude, phase, in-phase, and quadrature component
A_{set}	oscillation amplitude setpoint
A_{free}	free oscillation amplitude
β	modulation index
B_{th}	bandwidth for thermal noise limited measurements
C	capacitance
D^{z}	vertical deflection noise power spectral density, $D^{\mathrm{z}} = (d^{\mathrm{z}})^2$
Δf	frequency shift
F_{ts}	tip–sample force
$G(\omega)$	transfer function
k	spring constant
k_{ts}	tip–sample force gradient
$\omega = 2\pi f$	(angular) frequency
ω_0	resonant frequency
ω_{cut}	−3 dB filter bandwidth
ω_{m}	modulation frequency
p_{c}	percolation threshold
τ	time constant
U_{ac}	Kelvin modulation amplitude, *ac* tip–sample voltage
U_{ds}	drain-to-source voltage
U_{lcpd}	local contact potential difference
Q	quality factor
v_{tip}	tip velocity
ξ	correlation length
z	z tip position
$z(t), \tilde{z}(\omega)$	vertical cantilever deflection

PHYSICAL CONSTANTS

c	speed of light in vacuum, $c = 299\,792\,458\ \mathrm{m\,s^{-1}}$
e	elementary charge, $e = 1.602\,176\,565(35) \times 10^{-19}\ \mathrm{C}$
$\hbar$	reduced Planck constant, $\hbar = 6.582\,119\,514(40) \times 10^{-16}\ \mathrm{eVs}$
k_B	Boltzmann constant, $k_\mathrm{B} = 8.617\,330\,3(50) \times 10^{-5}\ \mathrm{eV/K}$
m_e	electron mass, $m_\mathrm{e} = 9.109\,383\,56(11) \times 10^{-31}\ \mathrm{kg}$

(CODATA 2014 [1])

1

INTRODUCTION

Nothing clears up a case so much as stating it to another person.
— Arthur C. Doyle, *The Memoirs of Sherlock Holmes*

For the last decades, the race towards smaller device structures for faster switching speeds and less power consumption was the main driver of innovations in microelectronics. As transistors approach dimensions of only a few nanometres today, the effects of contact resistance begin to dominate over the behaviour locally within the channel. These effects need to be separated from each other in order to detect bottlenecks and to optimise device performance. Hence, methods for local electronic characterisation on the nanoscale with both high sensitivity and spatial resolution are essential for future device improvements.

Scanning probe microscopy offers an approach to tackle this problem. To this end, forces exerted on a sharp probe moving across the surface are detected. The mapping of sample topography is possible by varying the probe–surface distance to maintain constant interaction. Electrostatic forces, also acting on the probe, depend on the surface potential caused by a difference in work function, localised charges, or voltages applied to electrodes. Focus of this thesis is the quantification of such local surface potentials by Kelvin probe force microscopy (KFM), a specialised scanning probe technique in which the electrostatic force between probe and surface is minimised.

Measurements on active nanoelectronic devices were challenging in the past due to the often large topography in real devices and the long-range averaging in KFM detection schemes usually employed under ambient conditions. This thesis presents a measurement scheme for KFM to overcome these obstacles based on stochastically optimal control and force gradient sensitive detection. The spatial resolution achieved is limited by the probe apex only, typically below 10 nm in diameter for sharp tips.

For several types of active nanoscale devices, the local electronic behaviour is investigated by KFM. Resistances of both the channel and the contacts are determined for indium arsenide nanowires, with device dimensions that would render a characterisation by four-point probe measurements inaccurate and difficult to implement. In electrically biased two-dimensional arrangements of 10 nm-diameter nanoparticles, a characteristic terrace-like potential landscape is found. The nanoscale gaps between adjacent nanoparticles provide a promising test bed for molecular electron-

ics and sensing applications. The local behaviour obtained by KFM provides a far deeper insight into transport through such nanoparticle networks than macroscopic current-voltage characteristics would allow.

STRUCTURE OF THIS THESIS

Chapter 2, "Fundamentals of atomic force microscopy", provides an introduction into atomic force microscopy. The detection of force gradients in dynamic operational modes is discussed in detail, based on the transfer of force gradient modulations into sidebands of the cantilever oscillation.

In chapter 3, "Quantitative imaging of electrostatic potentials", the two basic variants of KFM are compared, and a control and detection scheme is developed for high-resolution quantitative surface potential measurements. The effects of noise and crosstalk are discussed.

Chapter 4, "Kelvin probe force microscopy of nanowire devices", presents measurements of indium arsenide nanowires in operating condition. Because of their large topography, these devices are challenging for high resolution KFM. Contact resistances to the wire and the wire resistance itself are extracted as a function of device current from KFM line profiles.

In chapter 5, "The potential landscape of nanoparticle networks", the local charge transport through two-dimensional nanoparticle assemblies is discussed theoretically and examined in KFM measurements. The effects of local changes in conductance are visualised by KFM measurements of the same device before and after introducing conjugated molecules. Nanoparticle devices are furthermore used as a benchmark for spatial resolution, since individual 10 nm-diameter particles appear distinctly from each other in topography and surface potential.

Finally, the construction of a homebuilt atomic force microscope is described in chapter 6, "Design and operation of a high vacuum beam-deflection AFM". The operation in high vacuum allows for enhanced sensitivity and device characterisation free of environmental influences. Combined topography and surface potential imaging is demonstrated in first investigations on a calibration grating and percolating nanoporous fullerene networks.

Although this thesis contains the author's insights, developments, and results, the remainder of this work is written from a point of view encompassing both the author and his research colleagues, who influenced and contributed to this thesis by discussions or by providing samples for characterisation.

2

FUNDAMENTALS OF ATOMIC FORCE MICROSCOPY

I lost all respect for angstroms.

— Heinrich Rohrer

In 1982, Binnig and Rohrer demonstrated, for the first time, controlled tunnelling through a vacuum gap [3]. Their first tunnelling junction consisted of a platinum plate and a sharp tungsten tip that could be approached towards the surface. Only a short time later, they showed that their setup could also produce spatially resolved maps of the surface—the scanning tunnelling microscope (STM) was born [4]. To this end, the tip or sample is moved in a raster-like fashion with a piezoelectric scanner; the tunnelling current is kept constant using a feedback loop adjusting the tip height above the surface.

The exponential decay of the tunnelling current with the distance made sure that ideally only the frontmost atom would contribute to the signal. Binnig and Rohrer obtained atomically resolved real-space images of surfaces only quickly thereafter [5, 6]. But since the STM relies on tunnelling through an electrically biased tip–sample junction, it is limited to conductive surfaces and thin insulators. In 1986, the atomic force microscope (AFM) was introduced [7] to overcome this limitation. It works on the principle of detecting *forces* acting on a sharp probe rather than currents.

Consequently, the AFM is sensitive to short range chemical interactions between tip and surface, enabling imaging and spectroscopy of atoms and molecules on surfaces [8, 9]. Besides, it also detects long-range van der Waals forces, magnetic forces, and electrostatic forces [10]. Van der Waals forces allow non-destructive, non-contact mapping of topography on virtually any surface, complemented by further information about the tip–sample interaction mapped at the same time.

As a force sensor, the first AFM used an auxiliary STM together with a cantilever beam, at whose end a sharp diamond chip was glued as a tip [7]. This was quickly superseded by capacitive [11] and optical detection [12, 13] of the cantilever displacement.

Stiff piezoelectric quartz sensors ($\approx$ kN . . . MN) vibrating at sub-nanometre amplitudes enabled to boost the sensitivity to short range forces. One example is the qPlus sensor, introduced by Giessibl [8] in 2000. It consists of an ordinary nominally 32.768 kHz tuning fork as used in quartz watches, whose one prong is fixed

Parts of this chapter have been published in *Beilstein J. Nanotechnol.* **6**, 2193 (2015) [2].

and the other one carries the tip. A similar sensor, but operating at megahertz frequencies, is the length-extension resonator (LER). The deflection signal is obtained by either a current or charge amplifier, depending on the operation frequency [14].

While the high stiffness enables stable operation at tiny amplitudes, it also reduces the sensitivity to weak long-range forces. Although, for example, magnetic force microscopy (MFM) with tuning forks has been demonstrated [15], piezoelectric sensors for the detection of long-range forces are considered useful only at low temperatures or when atomic resolution is desired within the same scan. Still, these sensors have enabled unprecedented results at low temperatures, such as manipulating and imaging the charge state of single molecules [16].

For detecting long-range forces, the most successful approach today consists of microfabricated cantilevers and optical beam deflection [13]. All measurements in this work were obtained with a commercial beam deflection AFM, an Asylum Research Cypher AFM (Santa Barbara, CA, USA) operated in ambient conditions. An exception is chapter 6, where we describe the construction and operation of a homebuilt AFM for high vacuum.

Besides a mechanism for detecting forces, an AFM requires a number of supplementary parts: a coarse approach mechanism, piezoelectric scanners, and control electronics as well as a set of amplifiers. These will be discussed in detail for the homebuilt AFM in chapter 6.

The detection of forces makes the AFM an extremely versatile instrument for surface investigations on the nanoscale that extend well beyond mere maps of topography. The AFM has been used in the past to measure mechanical properties such as the elastic modulus and strength of e.g. graphene sheets [17]. Specialised modes of operation exist for obtaining the piezoelectric response of materials [18] (piezoresponse force microscopy, PFM), electrostatic forces and surface potentials [19, 20] (electrostatic force microscopy, EFM; Kelvin probe force microscopy, KFM), magnetic forces [21], and many more.

At the focus of this thesis are the local electrostatic forces between the probe and sample and how variations of the surface potential can be quantified on the nanoscale. Before we discuss how this is done in chapter 3, we look into the fundamental operating modes of an AFM.

STATIC AND DYNAMIC MODES OF OPERATION

AFMs are operated in either static or dynamic modes. Static modes, or contact modes, use the static deflection of the cantilever upon close interaction with the surface. By the cantilever spring constant, this deflection corresponds directly to the tip–sample interaction force. However, static modes operate in the regime of repulsive, short-

range forces, and lateral forces during the scan may unintentionally modify the sample. Therefore, soft cantilevers with low spring constants of less than 1 N/m are used to operate at low repulsive forces and mitigate damage.

In dynamic modes, the cantilever is excited mechanically by a dithering piezo element[1] at or near resonance. As the cantilever approaches the surface, the resonant frequency changes from free resonance, f_0, to a different frequency, $f_0 + \Delta f$. Either the frequency shift Δf or consequences of the frequency shift, such as a change in oscillation amplitude or phase, are tracked and kept constant using a feedback loop to produce a map of the topography.

In the following, we first look into the physics of the cantilever and the sensing principle. Then, we outline the two primary modes of dynamic operation: frequency and amplitude modulation. Finally, for both cases we show the impact of a modulated force gradient on the oscillation.

2.1 HARMONIC OSCILLATOR

The cantilever motion is best understood from a damped harmonic oscillator driven by an external drive, $a(t)$, and perturbed by the tip–sample interaction, $F_{\mathrm{ts}}(z, \dot{z}, t)$,

$$\ddot{z} + \frac{\omega_0}{Q}\dot{z} + \omega_0^2 z = \omega_0^2 a(t) + \frac{\omega_0^2}{k} F_{\mathrm{ts}}(z, \dot{z}, t). \tag{2.1}$$

Here, $z(t)$ is the cantilever deflection, ω_0 the eigenfrequency, k the spring constant, and Q the quality factor of the cantilever. For an oscillation with amplitude A and drive frequency $\omega_{\mathrm{d}} \approx \omega_0$, the interaction force can be approximated to

$$F_{\mathrm{ts}} \approx \langle F_{\mathrm{ts}} \rangle|_{z=z_0} + \left\langle \frac{\partial F_{\mathrm{ts}}}{\partial z} \right\rangle \Bigg|_{z=z_0} (z - z_0), \tag{2.2}$$

where z_0 is the mean tip position, and $\langle F_{\mathrm{ts}} \rangle$ and $\langle \partial F_{\mathrm{ts}}/\partial z \rangle \equiv k_{\mathrm{ts}}$ are the effective force and force gradient, respectively. Explicit expressions for the effective force and force gradient, averaged over the oscillation period, $T \approx 2\pi/\omega_{\mathrm{d}}$, are [24]

$$\begin{aligned} \langle F_{\mathrm{ts}} \rangle (z_0) &= \frac{1}{T} \int_0^T \mathrm{d}t F_{\mathrm{ts}}(z_0 + A\sin(\omega_{\mathrm{d}} t)) \\ &= \frac{1}{\pi} \int_{-A}^{A} \mathrm{d}q \frac{F_{\mathrm{ts}}(z_0 + q)}{\sqrt{A^2 - q^2}} \end{aligned} \tag{2.3}$$

1 Recently, photothermal excitation [22, 23] has become an alternative. Especially in liquid environments, the acoustical drive grows a "forest of peaks", a number of spurious resonances produced by shaking the liquid volume. Photothermal excitation periodically heats the cantilever with a laser aimed at its base, confining the excitation to the lever only. Though the situation is not as bad in air and vacuum, these environments might also benefit from a cleaner drive signal.

and

$$k_{\mathrm{ts}}(z_0) = \frac{2}{\pi A^2} \int_{-A}^{A} \mathrm{d}q \frac{\partial F_{\mathrm{ts}}}{\partial z}(z_0 + q)\sqrt{A^2 - q^2}. \tag{2.4}$$

The effective force and force gradient, as introduced here, allow one to describe the motion of the tip in the non-linear force field close to the sample with the model of a perturbed harmonic oscillator, provided the oscillation remains approximately harmonic with constant amplitude [10]. Stable operation is possible as long as $kA > \max(-F_{\mathrm{ts}})$ [10].

Equation (2.1) tells us, knowing $a(t)$ and $F_{\mathrm{ts}}(z, \dot{z}, t)$, how the deflection $z(t)$ is about to evolve. Neglecting F_{ts}, we find the transfer function from drive to deflection as

$$G(\omega) = \frac{\omega_0^2}{\omega_0^2 - \omega^2 + i\frac{\omega_0 \omega}{Q}}. \tag{2.5}$$

Operation at resonance, ω_0, produces a Q-fold amplified signal lagging 90° behind the drive. The interaction force can be included as approximated above. With a small perturbation, $k_{\mathrm{ts}} \ll k$, the resonant frequency of the cantilever changes from ω_0 to $\omega_0 + \Delta\omega$ with [25]

$$\frac{\Delta\omega}{\omega_0} = \frac{\Delta f}{f_0} = -\frac{k_{\mathrm{ts}}}{2k}. \tag{2.6}$$

2.2 AMPLITUDE AND FREQUENCY MODULATION

If the excitation is at constant amplitude at a set frequency close to resonance, the amplitude and phase of the driven oscillation follow changes in force gradient. This *would* produce an amplitude and phase modulation when moving across the surface. When the amplitude is used for topography feedback, we call this mode of detection *amplitude modulation* AFM (AM-AFM)—even though there should be no variations in amplitude anymore. The AFM tip thus traces contours of constant amplitude along the surface. Typical set points are ≈80 . . . 90 % of the free amplitude, measured well above (microns) away from the surface.

With oscillations up to 100 nm in amplitude, the tip can penetrate the short-range repulsive interactions at the closest point of approach. Since the tip is there only for a small fraction of the oscillation period, the risk of sample damage is highly reduced compared to contact mode. Lateral forces are virtually absent. But at the same time, the tip may dissipate energy during its interaction with the surface. If the dissipated energy is not compensated with an increased drive, this also results in a reduced

amplitude. This complex behaviour, the mix of conservative ($k_{ts} \rightarrow \Delta\omega \rightarrow \Delta A$) and dissipative ($\Delta Q \rightarrow \Delta A$) interactions, complicates a quantitative analysis [26].

Depending on the free amplitude and setpoint, AM-AFM can be operated in either net-attractive or net-repulsive regimes [26, 27]. But due to the highly non-linear tip–sample interaction, instabilities are possible leading to wrong height measurements. Care should be taken especially when sudden jumps in phase are observed.

The phase of the cantilever oscillation, recorded with a lock-in amplifier, offers a signal complementing the topography. It also is a mix of conservative and dissipative interaction and qualitatively gives a handle on variations of composition, friction, adhesion, and other interactions. Quantitatively, the sine of the phase is related to the tip–sample energy dissipation [28, 29].

The amplitude changes on a time scale of $\tau = 2Q/\omega_0$ until it reaches steady-state. In environments with high quality factors, such as in vacuum, this severely limits the scanning speed. However, relying on a mostly monotonous control signal, AM-AFM is easy to implement and operate, and it has found widespread use in ambient and liquid environments.

For *frequency modulation* AFM (FM-AFM), the cantilever is always excited at the momentary resonant frequency by means of a phase-locked loop (PLL) [25]. An additional feedback loop maintains a constant oscillation amplitude by adjusting the excitation. The PLL provides a frequency shift output signal, $\Delta\omega$ or Δf, for use in topography feedback. Thus, the tip traces an isosurface of constant frequency shift during a scan. Operation *at* resonance, as ensured by the PLL, retains maximum force sensitivity at all times.

Since PLL and amplitude controller directly separate conservative from dissipative interactions, a quantitative analysis of the tip–sample interaction is possible. The Δf signal can be turned into an interaction force and energy by means of the Sader-Jarvis formula [30]. The excitation signal translates to the energy dissipation per oscillation cycle. Experiments performed under different conditions with different cantilevers can be compared using the normalised frequency shift, $\gamma = \Delta f k A^{3/2}/f_0$ [10].

In contrast to AM-AFM, there is no limitation to low quality factors because the amplitude is maintained in a feedback loop, reducing transients.[2] Within the PLL bandwidth, the frequency shift responds immediately to changes in k_{ts}.

However, the PLL and amplitude controllers are prone to instabilities. Due to the non-monotonous tip–sample force over distance, the frequency shift can change its gradient with respect to distance from positive to negative, or vice versa. Depending on which branch topography feedback was performed originally, the tip may drive further into the surface rather than being retracted. This is the beginning of

2 But when the oscillation amplitude changes unexpectedly or the amplitude controller fails, it takes a time $\propto Q$ to recover. High Q is both boon and bane.

an avalanche: The reduction in amplitude because of increased dissipation is subsequently compensated by a higher drive. Still, the tip continues its travel into the surface, dissipating even more energy. Ultimately, the frequency shift will exceed the lock range of the PLL. However, when the drive frequency does not anymore match the resonant frequency, the loss in signal is again compensated by the amplitude controller.

This fundamental difficulty of FM-AFM renders non-contact operation, i.e. operation within the reign of attractive forces, a delicate venture. On rough surfaces with steep edges, stable operation demands good feedback tuning and reduced scanning speeds. To prevent tip damage, AFM controllers often implement a tip protection circuit into their feedback loop, which detects an unlocking PLL or the sudden increase in excitation, and consequently withdraws the tip.

Thus, both amplitude and frequency modulated detection schemes have their deficiencies and benefits. It depends on the sample and experimental details which mode to choose. Since both modes detect changes in force gradient, they are mostly equivalent in terms of resolution.[3] Clean separation of concerns, quantitative interpretation of the control signal, and performance with high Q-factors make FM-AFM attractive for atomic resolution imaging in ultra-high vacuum. For messy surfaces in ambient conditions, AM-AFM is usually a better choice.[4]

2.3 THE ORIGIN OF SIDEBANDS

Both AM and FM methods detect changes in force gradient. But what happens when the force gradient changes periodically? According to eq. (2.6), a modulation, e.g. an oscillating electric field, causes a frequency modulation of the resonance. Hence, a modulation at a single frequency ω_m will produce *sidebands* at integer multiples of the modulation frequency, that is, cantilever oscillations at $\omega_0 \pm \omega_\mathrm{m}$, $\omega_0 \pm 2\omega_\mathrm{m}$, etc.

For the derivation of the sideband signals and their respective amplitudes, we assume a modulation of the force gradient at the frequency ω_m:

$$k_\mathrm{ts}(z_0, t) = \hat{k}_\mathrm{ts}(z_0)\, \cos(\omega_\mathrm{m}\, t + \varphi_\mathrm{k}). \tag{2.7}$$

3 This holds only when a force gradient perturbs the harmonic oscillator, and the effects on the driven cantilever oscillation are detected. An important exception is KFM operated in amplitude modulation. Without mechanical drive, $a(t) \equiv 0$ in eq. (2.1), $F_\mathrm{ts}(t)$ instead drives the cantilever at some frequency by means of the electrostatic force between tip and surface. The amplitude detected at this frequency hence is sensitive to the force, not to the force gradient.

4 So far, there are only few research groups performing FM-AFM in ambient. One reason is the formation of a water meniscus, which adds to dissipation and contributes yet another attractive force component, pulling the tip to the surface. This can be overcome by stiff cantilevers operated at larger amplitudes.

Note that the effective force gradient as calculated above, eq. (2.4), is only valid for $\omega_m \ll \omega_d$. Then, by Fourier transformation of the equation of motion, eq. (2.1), we arrive at

$$G^{-1}(\omega)\tilde{z}(\omega) = \tilde{a}(\omega) + \frac{\hat{k}_{ts}(z_0)}{2k}\left[e^{i\varphi_k}\tilde{z}(\omega-\omega_m) + e^{-i\varphi_k}\tilde{z}(\omega+\omega_m)\right] \tag{2.8}$$

where $\tilde{z}(\omega) = \int_{-\infty}^{\infty} \mathrm{d}t\, z(t)\exp(-i\omega t)/\sqrt{2\pi}$ and $\tilde{a}(\omega)$ are the Fourier transformed deflection and drive, respectively, and $G(\omega)$ is the complex transfer function of the damped harmonic oscillator.

Equations (2.5) and (2.8) present an iterative scheme to determine the spectral components of the cantilever oscillation, where in each step $\tilde{z}(\omega)$ on the left hand side of eq. (2.8) is refined by the expressions on the right hand side. Starting from an oscillator at rest, $\tilde{z}_0(\omega) = G(\omega)\tilde{a}(\omega)$ is the carrier oscillation due to the external drive, as in the unperturbed system. Spectral components at $\omega \pm \omega_m$ emerge in the next iteration step,

$$\tilde{z}_1(\omega \pm \omega_m) = \frac{\hat{k}_{ts}}{2k} e^{\pm i\varphi_k} G(\omega \pm \omega_m)\, \tilde{z}_0(\omega). \tag{2.9}$$

This is the fundamental pair of sidebands of the force modulated damped harmonic oscillator. With $\hat{k}_{ts} \ll k$, the higher order sidebands arising in the subsequent iterations are usually negligible.

Equation (2.9) also describes the sideband amplitude transfer function when the expression is evaluated close to the sideband frequencies. With the substitution $\omega - \omega_d \to \omega$, we find

$$\frac{\tilde{z}_\pm(\omega)}{\tilde{z}_c(\omega)} = \frac{\tilde{z}_1(\omega_d \pm \omega_m + \omega)}{\tilde{z}_0(\omega_d + \omega)} = \frac{\hat{k}_{ts}}{2k} e^{\pm i\varphi_k} G(\omega_d \pm \omega_m + \omega) \tag{2.10}$$

$$\approx -\frac{\hat{k}_{ts}}{2k}\frac{\omega_0}{2}\frac{ie^{\pm i\varphi_k}}{i(\omega \pm \omega_m) + \omega_c} = \frac{\Delta\hat{\omega}}{2\omega_m}\frac{ie^{\pm i\varphi_k}}{i(\omega/\omega_m \pm 1) + \omega_c/\omega_m}, \tag{2.11}$$

where, in the last approximation, we consider only the dominant term for a drive close to the eigenfrequency, i.e. $\omega_d \approx \omega_0$ and $\omega \ll \omega_0$, and $\omega_c = \omega_0/2Q$ is the cantilever bandwidth.

For modulation frequencies well beyond the cantilever bandwidth, $G(\omega_0 \pm \omega_m) \approx -i\omega_0/2\omega_m$, and the amplitude of each sideband is $|\tilde{z}_\pm| \approx A\Delta\hat{\omega}/2\omega_m$, where A is the carrier amplitude. The latter expression also follows immediately from a narrowband frequency modulation of a carrier oscillation at ω_d. With a carrier amplitude A and the peak frequency deviation $\Delta\hat{\omega}$, a frequency modulation at ω_m produces two sidebands with amplitudes $\beta A/2$, where $\beta \equiv \Delta\hat{\omega}/\omega_m$ is the modulation index [31].

Under ultra-high vacuum conditions, large Q factors typically cause negligible cantilever bandwidths, making this approximation valid e.g. for finding the noise power spectral density of the frequency shift signal in FM-AFM [32].

Moreover, when the narrow-band conditions are not met ($\beta \gg 1$), the iterative scheme for the sideband amplitudes in eqs. (2.5) and (2.8) approaches the Bessel functions describing the sideband amplitudes in a general frequency modulation for $\omega_\mathrm{m} \gg \omega_\mathrm{c}$. With $\tilde{z}(\omega) = \sqrt{2\pi}\sum_{n=-\infty}^{\infty} \hat{z}_n \delta(\omega_\mathrm{d} + n\omega_\mathrm{m} - \omega)$, eq. (2.8) can be written as a recurrence relation:

$$G^{-1}(\omega_\mathrm{d} + n\omega_\mathrm{m})\,\hat{z}_n = \hat{a}\delta_{n0} + \frac{\hat{k}_\mathrm{ts}}{2k}\left[\hat{z}_{n-1} + \hat{z}_{n+1}\right]. \tag{2.12}$$

Then, for $\omega_\mathrm{d} = \omega_0$, $\omega_\mathrm{m} \ll \omega_0$, $Q \gg 1$, and $n \neq 0$, the above relation simplifies to

$$\hat{z}_{n+1} + \hat{z}_{n-1} = 2n\frac{\omega_\mathrm{m}}{\Delta\hat{\omega}}\,\hat{z}_n, \tag{2.13}$$

which resembles the recurrence relation $J_{n+1} + J_{n-1} = (2n/\beta)\,J_n$ [33] for the Bessel functions of the first kind, $J_n(\beta = \Delta\hat{\omega}/\omega_\mathrm{m})$. In this limit, the sidebands are the same as in frequency modulation, and β is the modulation index.

The Fourier approach for the sideband amplitudes, as presented above, also accurately models the behaviour of the sideband amplitude and phase for modulation frequencies approaching the cantilever bandwidth ω_c. In fig. 2.1a, we show the expected and experimentally measured sideband amplitudes and phases. The excellent agreement with the above model proves the validity of our derivation. Each sideband is phase-shifted by $\pm\varphi_\mathrm{k} + \arg G(\omega_\mathrm{d} \pm \omega_\mathrm{m})$.

For narrow-band frequency modulation, we can define a complex modulation index $\tilde{\beta}$ by the sideband and carrier amplitudes as $\tilde{\beta} \equiv z_+/z_\mathrm{c} - \overline{z_-/z_\mathrm{c}}$. With eq. (2.11), the *dc* response ($\omega \to 0$) of $\tilde{\beta}$ thus is

$$\tilde{\beta} = \beta\frac{ie^{i\varphi_\mathrm{k}}}{i + \omega_\mathrm{c}/\omega_\mathrm{m}}. \tag{2.14}$$

Figure 2.1b shows the amplitude and phase of $\tilde{\beta}$ for pure narrow-band FM and the harmonic oscillator as a function of $\omega_\mathrm{m}/\omega_\mathrm{c}$. The amplitude and phase only agree with the result for pure narrow-band frequency modulation when the cantilever bandwidth is negligible compared to the modulation frequency. For low modulation frequencies $|\tilde{\beta}|$ approaches $\Delta\hat{\omega}/\omega_\mathrm{c} = 2Q\Delta\hat{\omega}/\omega_0$ instead (eq. (2.14)).

To further demonstrate the validity of the sideband transfer function, we show in fig. 2.2 the response to a step in $\hat{k}_\mathrm{ts}$ from both the approximation in eq. (2.11) and from a numerical simulation of the perturbed harmonic oscillator, eq. (2.1), including lock-in amplifiers at $\omega_\mathrm{d} \pm \omega_\mathrm{m}$. Each change in the force gradient modulation

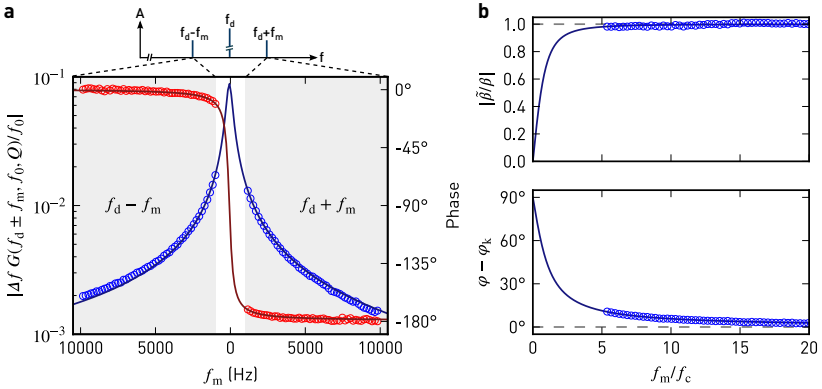

FIGURE 2.1: (a) Sideband amplitude (blue) and phase (red) relative to the carrier oscillation measured during a sweep of the modulation frequency (markers), and a fit of the harmonic oscillator (solid lines). At a constant height of ≈25 nm above the sample, the tip was driven mechanically at $f_d = \omega_d/2\pi = 70\,657$ Hz and electrically at f_m. Parameters to the least-squares fit are $\Delta\hat{f} = 33$ Hz, $f_0 = 70\,586$ Hz, and $Q = 190$. (b) Amplitude and phase of the complex modulation index for a narrow-band frequency modulation, $\tilde{\beta} \equiv z_+/z_c - \overline{z_-/z_c}$. The solid lines are a plot of the approximation in eq. (2.14). The dashed lines indicate the expected behaviour for $f_m \gg f_c$, neglecting the influence of the damped harmonic oscillator.

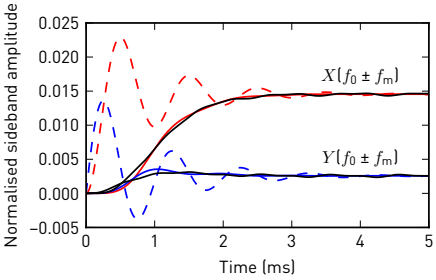

FIGURE 2.2: In-phase (red) and quadrature (blue) sideband amplitudes, normalised to the carrier oscillation amplitude A, in response to a step in the force gradient modulation amplitude. The step responses following from eq. (2.11) (dashed), show oscillations at f_m, exponentially decaying with $1/\omega_c$, which are removed by the lock-in amplifier's low-pass filter (solid, $f_{cut} = 250$ Hz, 24 dB/oct). The solid black lines show the demodulated sideband amplitudes from a direct numerical simulation of the perturbed harmonic oscillator. (Numerical parameters: $f_0 = 70\,500$ Hz, $Q = 200$, $A = 10$ nm, $f_m = 1000$ Hz, $\varphi_k = 0$, $\Delta\hat{f} = 30$ Hz)

also excites a transient oscillation at the resonant frequency of the cantilever, which appears in the sideband signal and decays exponentially with $1/\omega_c$. Therefore, the lock-in amplifier's filter settings should be set accordingly to provide sufficient rejection near ω_m.

We conclude that sidebands evolve as soon as k_{ts} gets modulated and it is not important whether the resonance frequency is actually tracked or not. There is no fundamental difference between amplitude and frequency modulated AFM. The main benefit of tracking the resonant frequency (e.g. with a phase-locked loop) is merely to keep the carrier phase constant, which would otherwise affect the sideband phases.

2.4 THERMAL NOISE AND FORCE GRADIENT SENSITIVITY

In section 2.1 we have discussed how the simple harmonic oscillator can help understanding cantilever dynamics in AFM, and how the tip–sample force translates into a frequency shift. We may now ask how small these forces may become while being able to tell them apart from measurement noise.

Because forces are detected from the cantilever deflection, the contribution of noise to this signal should be minimised. There are two main components: thermal noise of the cantilever and noise in the detection system.

Noise in the detection system is inherent to the detector. Charge or current amplifiers, as used for photodiodes, tuning forks, and LERs, employ feedback resistors (R) which add *Johnson-Nyquist noise*, $D_{ds,nyq} \propto RT$ [34, 35]. The quantum nature of charges flowing within amplifiers and photons deflected off the cantilever gives rise to *shot noise*, $D_{ds,shot}$, proportional to the flux of carriers [36]. Both sources are white, i.e. independent of frequency. Slow processes such as thermal drift add another term at low frequencies: $1/f$ noise.

The complete detection system noise power, $D_{ds}^z = {d_{ds}^z}^2$, is the sum of these contributions. The noise amplitude, d_{ds}^z, in fm $\mathrm{Hz}^{-0.5}$, depends on temperature, amplification, laser power, spot size for a given cantilever [37], and additional factors. Usually, with the comparably high frequencies and small bandwidths for AM- and FM-AFM, we can consider the detection noise to be constant.

But even if it could be eliminated, there would be noise due to the cantilever itself. Consider a cantilever without drive in equilibrium with a thermal bath at temperature T. Using the equipartition theorem, there is a contribution of $k_B T/2$ per degree of freedom to the mean energy stored in the oscillator,

$$\langle E \rangle = \frac{1}{2} k \left\langle z^2(t) \right\rangle = \frac{1}{2} k_B T. \tag{2.15}$$

Using the Wiener-Khinchin theorem, the variance of the deflection, $\langle z^2(t)\rangle$, relates to the deflection noise power spectral density, D^z_{th}, as a stationary random process,

$$\langle z^2(t)\rangle = \frac{1}{2\pi}\int_0^\infty \mathrm{d}\omega D^z_{\mathrm{th}}(\omega). \tag{2.16}$$

Assuming white noise driving the cantilever, D^z_{th} must be proportional to the cantilever transfer function $G(\omega)$,

$$\frac{1}{2}kD^z_{\mathrm{th}} = \psi G^2(\omega). \tag{2.17}$$

Solving for ψ results in $\psi = 2k_{\mathrm{B}}T/\omega_0 Q$. Thus, an expression for the thermal displacement noise is [32]

$$D^z_{\mathrm{th}}(\omega) = \frac{4k_{\mathrm{B}}T}{kQ\omega_0}G^2(\omega) = \frac{4k_{\mathrm{B}}T}{kQ\omega_0}\frac{Q^2}{Q^2\left(1-(\omega/\omega_0)^2\right)+(\omega/\omega_0)^2}. \tag{2.18}$$

At resonance, there is an amplification by Q. At $\omega = \omega_0$, we obtain thus

$$D^z_{\mathrm{th}}(\omega_0) = \frac{4k_{\mathrm{B}}T}{k\omega_0}Q. \tag{2.19}$$

Near resonance, D^z_{ds} decays with the square of the modulation frequency (cf. section 2.3)

$$D^z_{\mathrm{th}}(\omega_0 \pm \omega_{\mathrm{m}}) \approxeq \frac{k_{\mathrm{B}}T}{kQ}\frac{\omega_0}{\omega_{\mathrm{m}}^2}. \tag{2.20}$$

The total noise power is the sum of detection system and thermal noise powers,

$$D^z_{\mathrm{tot}} = D^z_{\mathrm{th}} + D^z_{\mathrm{ds}}, \tag{2.21}$$

and the total deflection noise amplitude is $d^z_{\mathrm{tot}} = \sqrt{D^z_{\mathrm{tot}}}$. Lübbe *et al.* [32] have introduced the bandwidth for thermal noise limited measurements, B_{th}, as the modulation frequency in eq. (2.20) at which D^z_{ds} coincides with D^z_{th}:

$$B_{\mathrm{th}} = \sqrt{\frac{f_0 k_{\mathrm{B}}T}{2\pi kQ}}\frac{1}{d^z_{\mathrm{ds}}}. \tag{2.22}$$

Below this frequency, thermal noise dominates and detection system noise may be neglected.

The minimum force gradient that can be discerned from noise can be obtained from the signal-to-noise ratio (SNR). Here, we consider as *signal* twice the sideband

amplitude expected from the sideband transfer function, eq. (2.11). The *noise* amplitude is determined by twice the noise *power*, integrated over a bandwidth B. For frequencies below B_{th}, we only need to consider thermal noise. The minimum detectable force gradient for thermal noise, $k_{\mathrm{ts}}^{\mathrm{min,th}}$, is obtained for unity SNR,

$$\mathrm{SNR} = \frac{2}{\sqrt{2B}} \frac{\tilde{z}_{\pm}(\omega_{\mathrm{d}} \pm \omega_{\mathrm{m}})}{d_{\mathrm{th}}^{\mathrm{z}}(\omega_0 \pm \omega_{\mathrm{m}})} \approxeq \frac{2}{\sqrt{2B}} \frac{k_{\mathrm{ts}}^{\mathrm{min,th}} A/2k}{\sqrt{4k_{\mathrm{B}}T/kQ\omega_0}} \stackrel{!}{=} 1. \tag{2.23}$$

Note here that for $\omega_{\mathrm{d}} \equiv \omega_0$, the transfer functions of signal and noise cancel each other, and thus the SNR is essentially frequency-independent. Solving for $k_{\mathrm{ts}}^{\mathrm{min,th}}$, we arrive at

$$k_{\mathrm{ts}}^{\mathrm{min,th}} = \sqrt{\frac{8kk_{\mathrm{B}}TB}{Q\omega_0 A^2}}. \tag{2.24}$$

This expression is the same as already stated in the original paper on FM-AFM by Albrecht *et al.* [25], but we arrived here using the sideband transfer function. For thermal noise limited measurements, $k_{\mathrm{ts}}^{\mathrm{min,th}}$ is reduced by using soft cantilevers with high frequencies and large quality factors at low temperatures and high amplitudes. Because for stable operation k and A are not independent [10], $k_{\mathrm{ts}}^{\mathrm{min,th}}$ scales as $A^{-3/2}$ or $k^{3/2}$. The optimal amplitude is on the order of the decay constant λ of the dominant tip–sample force [38].

For dominant detection noise, the transfer functions of signal and noise do not cancel anymore. By an SNR analysis similar to the above, we arrive at the following expression for dominant detection noise

$$k_{\mathrm{ts}}^{\mathrm{min,ds}} = d_{\mathrm{ds}}^{\mathrm{z}} \sqrt{\frac{8k^2}{A^2} \int_0^B \mathrm{d}f_{\mathrm{m}} \left(\frac{f_{\mathrm{m}}}{f_0}\right)^2} = \sqrt{\frac{8}{3}} \frac{k d_{\mathrm{ds}}^{\mathrm{z}} B^{3/2}}{f_0 A} \tag{2.25}$$

for detection noise limited systems. Noise increases much faster with bandwidth than in a thermal noise limited system [39]. The dependence on $B^{3/2}$ was first derived by Dürig, Steinauer & Blanc [40].

Thermal and detection noise in the deflection signal can be measured around ω_0 with a spectrum analyser. For thermal noise, Q and ω_0 determine the shape of the thermal peak, whereas the noise power scales with $1/k$ for a given temperature. Therefore, knowing the spring constant of the cantilever, thermal noise is often used to calibrate the sensitivity of the detection system. For cantilevers, the spring constant is usually not known precisely, since it is proportional to the cube of the cantilever thickness and thus susceptible to tolerances in the manufacturing process.

Although k can be determined likewise from a thermal fit knowing the detector sensitivity, this approach involves a measurement of the cantilever deflection during

a force or amplitude vs. distance curve on a hard surface, and calibrating the detector against the z stage.[5] This may involve a peak force upon approach that exceeds a gentle scan setpoint, possibly damaging the tip. In air, a popular non-invasive method by Sader [42, 43] exploits the effect of viscous damping, diminishing the quality factor dependent on cantilever shape. Knowing ω_0 and Q from a thermal fit, k can be obtained from the plan view dimensions of rectangular cantilevers [42]. Recently, this method was extended to cantilevers of arbitrary shape [43]. A particular result allows one to relate k to k_{test}, the spring constant of a test cantilever, via the quality factors Q and Q_{test} as well as the resonant frequencies f_0 and $f_{0,\text{test}}$ of the cantilever and test cantilevers, respectively,

$$k = k_{\text{test}} \frac{Q}{Q_{\text{test}}} \left(\frac{f_0}{f_{0,\text{test}}} \right)^{2-\alpha}, \tag{2.26}$$

where the exponent $\alpha \approxeq 0.7$ originates from the power-law dependence of the hydrodynamic function on the Reynolds number. Knowing the parameters of a single test cantilever, therefore, other cantilevers of the same type can be calibrated.[6]

2.5 CONCLUSION

In this chapter, we have introduced the principles and theory of AFM. We have shown how the harmonic oscillator provides a simple but reliable model to understand the tip motion. We also compared AM with FM topography feedback techniques. Although both are based on modifications of the resonance curve, truly quantitative interpretation of forces is only possible by FM detection.

We have provided a detailed quantitative description of the evolution of sidebands which appear upon force gradient modulations in dynamic AFM. Their direct demodulation by lock-in techniques facilitates force gradient sensitive detection of the surface potential without the complexity of a PLL, as we will show in the next chapter.

We also discussed prominent noise sources and how they ultimately pose a detection limit on the force gradient. Once again, the sideband transfer function enabled a rather straightforward approach while reproducing the results known from literature.

5 A gentle approach exploits the amplitude-dependence of the normalised frequency shift, γ, in FM-AFM to calibrate the amplitude upon small changes against the z stage [41].

6 This calibration is implemented in the software supplied with Asylum Research AFMs as the *GetReal* feature and used for the spring constants and sensitivities within this thesis.

3

QUANTITATIVE IMAGING OF ELECTROSTATIC POTENTIALS

"Data! Data! Data!" he cried impatiently. "I can't make bricks without clay."
— Arthur C. Doyle, *The Adventures of Sherlock Holmes*

The device performance of today's nanoelectronic devices, and even more so of potential future generations including nanowires or molecular junctions, critically depends on transport properties varying on a length scale of a few nanometres only in the active channel or at electrode interfaces. Methods for local electronic characterisation, providing accurate measurements with nanometre spatial resolution, are in very high demand, but have been lagging behind the technological requirements.

Kelvin probe force microscopy (KFM) is a technique that allows mapping local electrostatic potentials with an atomic force microscope [20, 44, 45]. In contrast to electrostatic force microscopy (EFM), which measures merely the effect of electrostatic forces on the oscillation of the tip, a feedback loop nullifies the electric field by adjusting a bias voltage between tip and sample. Hence, Kelvin probe force microscopy is able to *quantify* the local contact potential difference (CPD), U_{lcpd}, which contains contributions, e.g. from the difference in work function between the AFM tip and structures on the sample, dopants and trapped charges in the device, or voltages applied to electrodes.

For electronic devices on the nanoscale, KFM measurements provide a unique tool to shed light upon a variety of otherwise inaccessible properties. For example, with a constant current passing through a two-terminal device, the potential drop at the contacts directly relates to the contact resistance. To extract contact resistance through traditional four-point measurements becomes increasingly difficult for scaled devices, in which the contact length is comparable to the device length. Recently, KFM has been used to extract the surface state density and Schottky depletion region in semiconductor nanowires [46, 47] or to determine the mean free path in carbon nanotubes [48]. KFM also allows one to determine intrinsic doping of two-dimensional crystals such as graphene [49, 50], where surface potential and electronic properties depend on the number of layers.

Parts of this chapter have been published in *Beilstein J. Nanotechnol.* **6**, 2193 (2015) [2].

In this chapter, we give a comprehensive overview of KFM and discuss spatial as well as potential resolution. We also introduce a novel control scheme enabling us to improve performance while minimising topographical artefacts.

3.1 KELVIN PROBE FORCE MICROSCOPY

KFM has found widespread use in both vacuum and ambient environments. In contrast to the STM, operating with a current flow between tip and surface, KFM operates in the non-contact regime with no *dc* current flow. Still, it is able to resolve changes in the local contact potential difference, U_{lcpd}, even on a molecular or atomic scale [16, 51].

Kelvin probe force microscopy is named after William Thomson, Baron Kelvin, who noticed and measured a potential difference between two electrically connected metal discs separated by a small distance [52]. This potential difference is due to differences in work function between the two plates.

As in Lord Kelvin's experiment, the AFM tip and sample form a capacitor. The energy stored within is

$$E = -\frac{1}{2}C(U_{\mathrm{ts}} - U_{\mathrm{lcpd}})^2, \tag{3.1}$$

where U_{ts} is the voltage applied to the tip, and C is the tip–sample capacitance.[1] U_{lcpd} is the contact potential difference between tip and surface. It contains the difference in work function, $eU_{\mathrm{cpd}} = \Phi_{\mathrm{tip}} - \Phi_{\mathrm{sample}}$, but also contributions due to charges, dipoles, and voltages applied to electrodes on the surface.

The electrostatic force experienced by the tip is

$$F_{\mathrm{el}} = -\left\langle \frac{\partial E}{\partial z} \right\rangle = \frac{1}{2}\left\langle \frac{\partial C}{\partial z} \right\rangle (U_{\mathrm{ts}} - U_{\mathrm{lcpd}})^2. \tag{3.2}$$

Here, we assume that U_{lcpd} is independent of distance. The angle brackets indicate averaging over the oscillation cycle as in eqs. (2.3) and (2.4). $\langle C' \rangle$ therefore is an effective capacitance gradient. By modulating U_{ts}, also F_{el} gets modulated. The main principle behind KFM is adding such a modulation on top of a *dc* bias, which is continuously adjusted to cancel the detected electrostatic force modulation.

KFM was first implemented by Nonnenmacher, O'Boyle & Wickramasinghe [20] in an amplitude modulated scheme, detecting the electrostatic force due to the modulation directly. Later, it was extended to frequency modulation by Kitamura & Iwatsuki [54] utilising the electrostatic force gradient.

1 The energy in eq. (3.1) is negative because the work done by the voltage source has to be considered [53].

Amplitude modulated detection

Most commercial instruments for operation in air include a scan mode based on amplitude modulation KFM (AM-KFM). In this mode, the feedback loop nullifies the cantilever oscillation that is excited by a modulated electrostatic force. Hence, the KFM image is a map of voltages required to compensate the electrostatic force at every point of the scanned field. However, since cantilever and AFM tip are extended objects, this voltage does not necessarily correspond to the local contact potential difference, U_{lcpd}, but represents a weighted average over the potentials present on the entire sample surface [55]. For AM-KFM, the weights are determined by the capacitance gradient, C', between the probe and the sample. Due to the long range electrostatic force, even parts far from the surface, such as the cantilever beam, can account for a significant fraction of the signal, limiting the spatial resolution and accuracy of the measurement. Within nanoscale devices, for example, electrode potentials may completely overshadow the channel [56].

Known approaches to increase spatial resolution and accuracy of surface potential measurements include deconvolution techniques [57, 58] or the use of slightly blunt tips supported by a cantilever of minimal surface area [55]. However, deconvolution techniques require a detailed model of the AFM tip to be accurate and usually neglect the sample topography [58], whereas blunt tips inevitably reduce topography resolution on three-dimensional structures.

KFM measurements are further complicated by a strong dependence of the detected signal on the tip–sample distance. In the often-employed lift-mode schemes, each line is scanned twice: first to acquire topography, and subsequently to retrace the scanned line at a small distance, Δz, above the surface to perform KFM measurements. This enables tuning the *ac* modulation frequency for KFM to resonance to enhance the signal, and, at the same time, to reduce the contribution of van der Waals forces to the total force measured and compensated. The scan at elevated height, however, reduces lateral resolution and accuracy of the KFM data as we will detail below. To minimise such lateral averaging, single-scan methods are preferred, performing topography and KFM measurements simultaneously. An additional benefit of single-scan AFM and KFM is the inherent suppression of electrostatically induced topography artefacts present in non-compensated topography scans [59, 60]. In AM-KFM, single-scan methods can be implemented taking advantage of multiple eigenmodes of the cantilever, using one mode for topography and another for KFM. Nevertheless, the averaging effect of the cantilever beam remains.

Frequency modulated detection

An alternative approach typically applied in vacuum is based on frequency modulation [25]. To this end, the frequency of the cantilever is usually tracked by a phase-locked loop (PLL). Its output signal, the frequency shift Δf, exhibits a frequency component at the electrostatic modulation frequency, which is nullified by the Kelvin feedback loop. Frequency modulated KFM (FM-KFM) [54, 61] thus provides a map of potentials required to minimise the electrostatic force *gradient*, proportional to Δf for small mechanical amplitudes, at every point during the scan,

$$k_{\mathrm{ts}}^{\mathrm{el}} = \left\langle \frac{\partial F_{\mathrm{el}}}{\partial z} \right\rangle = \frac{1}{2} \left\langle \frac{\partial^2 C}{\partial z^2} \right\rangle (U_{\mathrm{ts}} - U_{\mathrm{lcpd}})^2. \tag{3.3}$$

Comparison of AM- and FM-KFM

As a consequence of detecting signals proportionally to C' or C'', contributions from different parts of the sample and the probe to the measured signal are weighted differently in AM- and FM-KFM. The dependence on the second-order capacitance gradient, C'', effectively eliminates the averaging contribution of the cantilever beam in FM-KFM as we demonstrate now.

Figure 3.1 shows a model calculation using typical cantilever and interaction parameters, summarising how much tip apex, cone, and beam of an AFM cantilever probe contribute to the measured KFM signal in AM and FM operation. Shown are the percentages of the contributions and corresponding weighting factors C' and C'' for AM and FM, respectively. To this end, we applied an analytic model of the electrostatic tip–sample interaction force [62] to the approximate geometry of a typically used cantilever (Olympus AC160), and we calculated C' and C'' as a function of tip–sample separation for different oscillation amplitudes (see appendix A.1). While tip apex and cone clearly dominate the FM-KFM signal, opening the avenue to high resolution quantitative imaging, the cantilever beam at a distance of 14 µm dominates the AM-KFM signal even close to the sample, which is the main reason for the notoriously low lateral resolution and poor potential accuracy in this mode. When comparing AM and FM modes, one should note that in lift-mode AM-KFM the cantilever is not oscillating anymore when the electrostatic forces are nullified, whereas the mechanical oscillation remains in multi-frequency AM-KFM and FM-KFM. Hence, for lift-mode the case $A \to 0$ should be considered, whereas in single-scan modes the oscillation applied for tracking topography remains. For best sensitivity and minimal spatial averaging, AM and FM modes need to be operated very close to the surface.

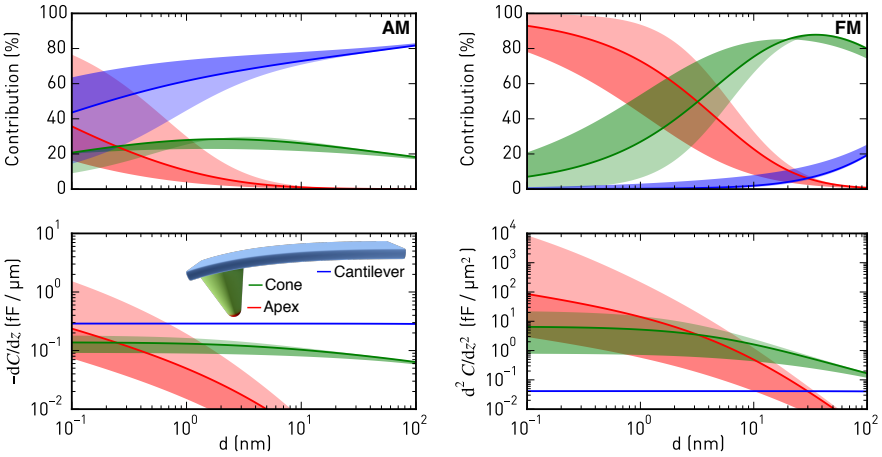

FIGURE 3.1: Contributions of apex, cone, and cantilever to the first (AM, left) and second (FM, right) order capacitance gradient as a function of distance for a mechanical oscillation amplitude of 5 nm (solid line) and an Olympus AC160 cantilever ($r_{\text{tip}} = 5\,\text{nm}$, $H_{\text{tip}} = 14\,\mu\text{m}$, $\theta = 17.5°$, and $A_{\text{lever}} = 160\,\mu\text{m} \times 40\,\mu\text{m}$). The light (dark) shaded regions indicate the range up to $A = 0.1\,\text{nm}$ (50 nm).

While the FM-KFM approach is clearly superior in terms of signal composition, several issues complicate its use in practice. First, it is often performed together with frequency modulated topography feedback that employs a PLL to determine Δf. The non-monotonous tip–sample interaction, by which Δf can change its slope between net-attractive and net-repulsive forces, can complicate stable operation of the topography feedback and may ultimately render PLL and amplitude controller unstable. On samples with coarse topography and steep features, maintaining stable FM topography feedback demands careful selection of operating parameters and slow scanning speeds. Furthermore, the choice of suitable bandwidths for topography and KFM feedback is more involved in traditional FM-AFM/FM-KFM implementations. For example, when Δf is used as an input to the lock-in amplifier detecting the electrostatic modulation, the PLL bandwidth must be wide enough to include the modulation frequency. Yet, it should be kept as small as possible for stable PLL operation and maximum noise rejection [63]. Finally, the pronounced distance dependence of C'' for apex and cone, as depicted in fig. 3.1, makes operation close to the surface more challenging, since small errors of the topography feedback produce marked changes of the effective Kelvin feedback gain. Similarly, when the tip encounters steep edges in topography, C'' may increase due to a larger effective tip–sample capacitor area, further complicating stable feedback operation. The distance depen-

dence is less pronounced at larger distances employed in lift-mode FM-KFM [56], but in addition to reduced lateral resolution, large modulation voltages are required due to weaker signals [64], which may induce band bending. Furthermore, when scanning across insulating parts of devices, such as gate oxides, not only the local dielectric constant changes, but because of their thickness also a limit is put on the minimum approachable distance in fig. 3.1. As a result, deliberately slow feedback settings to ensure stable operation are common practice.

3.2 LIFT-HEIGHT DEPENDENCE OF THE SURFACE POTENTIAL

To attain highest lateral resolution, the apex contribution to C' and C'' needs to be maximised. As shown in fig. 3.1, this is achieved for both AM- and FM-KFM by a reduction of tip–sample distance and oscillation amplitude. In lift-mode AM-KFM the oscillation amplitude is almost zero. There is no topography feedback during the lift pass, and hence a small separation to the surface is required. Lateral and vertical drift could otherwise drive the tip into the sample. Safe operation close to the surface thus requires topography feedback in most setups. For FM-KFM, the total C'' falls off quickly with distance, such that above ≈20 nm lift a good signal-to-noise ratio is only possible with increased modulation amplitudes.

In fig. 3.2, we show the topography and surface potential of a network of 10 nm gold nanoparticles. The network is electrically contacted with graphene electrodes on the left and right (dashed lines indicate electrode boundaries), and biased by a voltage of 5 V on the right. The terrace-like potential drop in such networks (see chapter 5) with distinct changes between adjacent particles is an excellent benchmark for lateral resolution. The oscillation amplitude in this case was about 10 nm. We acquired topography, fig. 3.2a, and surface potential, fig. 3.2b, in a single-scan method. After each line, the tip was forced to follow the previously acquired scan line at a distance of 5 nm while the lift-mode surface potential, fig. 3.2c, was obtained. Even with such small lift, the resolution is noticeably reduced, as detailed in the magnified insets.

Under many circumstances, U_{lcpd} obtained by an ideal tip should be independent of distance on a homogeneous surface.[2] In presence of crosstalk on the Kelvin regulation signal, however, U_{lcpd} as obtained by the feedback loop appears distance-dependent [65]. As the distance to the surface is increased, the crosstalk due to stray capacitive coupling stays approximately constant while C' and C'' are lowered. This

2 A notable exception is the existence of free charges within the tip–sample capacitor, e.g. due to charge trapped within an oxide layer. For example, image charges projected onto electrodes, including the tip, give rise to a position-dependent contribution to the total electrostatic energy [53].

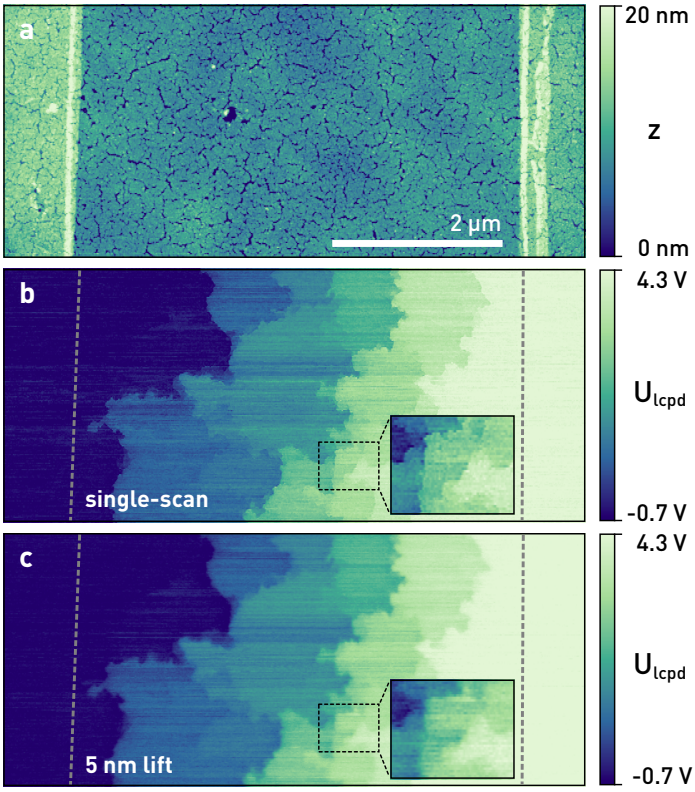

FIGURE 3.2: (a) Topography and (b) & (c) surface potential of a nanoparticle network device biased at 5 V. The lift-mode scan (c), obtained interleaved with the single-scan topography and KFM in (a) & (b) already shows degraded resolution at an elevation of 5 nm.

induces a fake distance dependence of U_{lcpd} after regulation.[3] Crosstalk of this type is largely absent in FM-KFM (cf. section 3.5), such that we did not observe any pronounced dependence on distance.

3.3 FORCE AND FORCE GRADIENTS UPON MODULATION

For Kelvin probe force microscopy, U_{ts} is modulated around a *dc* voltage,

$$U_{\mathrm{ts}} = U_{\mathrm{dc}} + U_{\mathrm{ac}} \cos(\omega_{\mathrm{m}} t). \tag{3.4}$$

Therefore, the electrostatic force F_{el}, eq. (3.2), and likewise its gradient $k_{\mathrm{ts}}^{\mathrm{el}}$, eq. (3.3), are modulated at ω_{m} and $2\omega_{\mathrm{m}}$,

$$k_{\mathrm{ts}}^{\mathrm{el}} = \left\langle \partial F_{\mathrm{ts}}^{\mathrm{el}} / \partial z \right\rangle = k_{\mathrm{ts}}^{\mathrm{el,dc}} + \hat{k}_{\mathrm{ts}}^{\mathrm{el},\omega} \cos(\omega_{\mathrm{m}} t) + \hat{k}_{\mathrm{ts}}^{\mathrm{el},2\omega} \cos(2\omega_{\mathrm{m}} t), \tag{3.5}$$

where

$$k_{\mathrm{ts}}^{\mathrm{el,dc}} = \frac{1}{2} \left\langle \frac{\partial^2 C}{\partial z^2} \right\rangle \left[\frac{U_{\mathrm{ac}}^2}{2} + (U_{\mathrm{dc}} - U_{\mathrm{lcpd}})^2 \right], \tag{3.6}$$

$$\hat{k}_{\mathrm{ts}}^{\mathrm{el},\omega} = \left\langle \frac{\partial^2 C}{\partial z^2} \right\rangle U_{\mathrm{ac}} (U_{\mathrm{dc}} - U_{\mathrm{lcpd}}), \text{ and} \tag{3.7}$$

$$\hat{k}_{\mathrm{ts}}^{\mathrm{el},2\omega} = \frac{1}{4} \left\langle \frac{\partial^2 C}{\partial z^2} \right\rangle U_{\mathrm{ac}}^2. \tag{3.8}$$

These modulations of the force gradient cause sidebands of the cantilever deflection at $\omega_{\mathrm{d}} \pm \omega_{\mathrm{m}}$ and $\omega_{\mathrm{d}} \pm 2\omega_{\mathrm{m}}$, which can be detected directly with lock-in amplifiers at the respective frequencies. The lock-in amplifiers return, relative to the reference oscillator, amplitude and phase of each sideband as well as their Cartesian projection: the in-phase component X and the quadrature component Y. In the narrow-band approximation, for modulations frequencies exceeding the the cantilever bandwidth, the in-phase components of the modulation at ω_{m} and the amplitudes at $2\omega_{\mathrm{m}}$ are

$$\begin{aligned} X(\omega_{\mathrm{d}} \pm \omega_{\mathrm{m}}) &= \pm \frac{A_0}{2\omega_{\mathrm{m}}} \frac{\omega_0}{2k} \hat{k}_{\mathrm{ts}}^{\mathrm{el},\omega} \\ &= \pm \frac{A_0}{2\omega_{\mathrm{m}}} \frac{\omega_0}{2k} \left\langle \frac{\partial^2 C}{\partial z^2} \right\rangle U_{\mathrm{ac}} (U_{\mathrm{dc}} - U_{\mathrm{lcpd}}) \end{aligned} \tag{3.9}$$

3 With crosstalk, it also matters whether the tip or the surface is modulated [65]. For nanoscale device characterisation, the only practical approach is to have both *dc* and *ac* bias on the tip, so that electrodes on the sample can be biased freely.

and

$$A(\omega_\mathrm{d} \pm 2\omega_\mathrm{m}) = \frac{A_0}{4\omega_\mathrm{m}} \frac{\omega_0}{2k} \hat{k}_\mathrm{ts}^{\mathrm{el},2\omega} = \frac{A_0}{4\omega_\mathrm{m}} \frac{\omega_0}{8k} \left\langle \frac{\partial^2 C}{\partial z^2} \right\rangle U_\mathrm{ac}^2. \tag{3.10}$$

The lock-in amplifier's reference phase offsets for the first set of sidebands at $\pm\omega_\mathrm{m}$ are chosen to maximise their respective in-phase components, taking into account the 180° phase shift of the lower sideband. Then, $X_\omega = X(\omega_\mathrm{d} + \omega_\mathrm{m}) - X(\omega_\mathrm{d} - \omega_\mathrm{m}) = \mathrm{Re}\,\tilde{\beta}_\omega A$ is the total in-phase component, which depends linearly on the applied *dc* bias. Furthermore, when U_dc matches U_lcpd, X_ω is nullified and the $\pm\omega_\mathrm{m}$ sidebands disappear.

The total amplitude of the second set of sidebands, $A_{2\omega} = A(\omega_\mathrm{d} + 2\omega_\mathrm{m}) + A(\omega_\mathrm{d} - 2\omega_\mathrm{m}) = |\tilde{\beta}_{2\omega}|A$, only depends on the *ac* modulation amplitude and the second order capacitance gradient, $C'' = \left\langle \partial^2 C/\partial z^2 \right\rangle$. This signal thus provides a handle for imaging variations in the tip–surface capacitance, surface dielectric properties [19], or lateral dopant profiling [66].

In fig. 3.3, we show experimental data of modulation indices $\tilde{\beta}_\omega$ and $\tilde{\beta}_{2\omega}$, calculated from the ω_m and $2\omega_\mathrm{m}$ sidebands, respectively, as a function of U_dc for different electrostatic modulation amplitudes, U_ac. During this experiment, the tip was positioned above a nickel electrode with amplitude modulated topography feedback enabled in net-attractive mode.

As expected from eq. (3.9), the ω_m sideband amplitudes (fig. 3.3a) vanish when $U_\mathrm{dc} = U_\mathrm{lcpd}$. While they change linearly with U_dc close to this point, there are nonlinear deviations at larger voltage offsets, which are caused by changes in C''. This is also evident from the $2\omega_\mathrm{m}$ sideband amplitudes (fig. 3.3b), showing the decrease of C'' with increasing voltage offsets. Since these sweeps are acquired with topography feedback enabled, the observed variations in C'' are most likely due to changes in the tip–surface separation: The AM topography feedback is sensitive to the static force gradient, which contains electrostatic interactions, eq. (3.6), that increase as the *dc* bias does not match the surface potential; consequently, the topography feedback retracts the tip, reducing C''.

In fig. 3.3c, we plot the ratio of the ω_m and $2\omega_\mathrm{m}$ sideband amplitudes, normalised to U_ac. As apparent from eqs. (3.9) and (3.10), this process cancels out the non-linearities and collapses the sweeps at different U_ac to a single curve.

Additionally, we show the similarly normalised amplitudes due to the electrostatic force at ω_m and $2\omega_\mathrm{m}$ in the deflection signal, which we acquired simultaneously with the sidebands at $\omega_\mathrm{d} \pm \omega_\mathrm{m}$. They show the same v-shaped relationship, with their minimum being slightly shifted with respect to the FM case. This shift is due to the

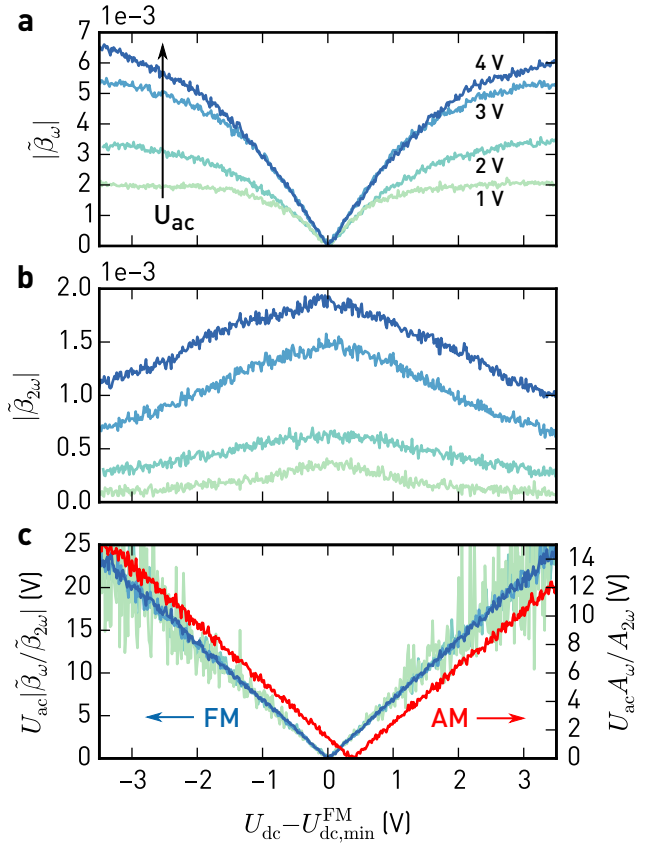

FIGURE 3.3: Modulation indices of the sidebands at ω_m (a) and $2\omega_m$ (b) against $U_{dc} - U^{FM}_{dc,min}$ for different modulation amplitudes U_{ac}. Topography feedback in amplitude modulation (net-attractive interaction) was enabled during these measurements. $U^{FM}_{dc,min}$, given by the minimum of $|\tilde{\beta}_\omega|$, is the contact potential difference found by FM detection. (c) Signals in (a) normalised using U_{ac} and $|\tilde{\beta}_{2\omega}| \propto C''$ (light green to blue, FM). Normalised electrostatic *force* (red, AM), simultaneously detected with lock-in amplifiers at ω_m and $2\omega_m$. (Parameters: A_{free} = 11.2 nm, A_{set} = 10.4 nm, Q = 500, k = 35 N/m f_0 = 302.5 kHz, f_m = 4 kHz)

different weights of contributions in the AM signal, cf. fig. 3.1. Setting the *dc* bias to the minimum obtained by AM-KFM does not guarantee to compensate the electrostatic force gradient and can cause height errors in topography. At the minimum determined from the sidebands, $|\tilde{\beta}| \propto C''$ in fig. 3.3b reaches its maximum value, corresponding to the closest approach.

3.4 NOISE LIMIT

As discussed before, best lateral resolution and least averaging is achieved for small distances with sharp tips and force gradient sensitive detection. Now, we turn our focus to the noise level expected in FM-KFM.

Although frequency shift noise was already discussed in the first FM-AFM paper by Albrecht *et al.* [25], the extension to noise in the regulated KFM signal was not available in literature until very recently. This might be due to the increased complexity of a FM-KFM setup. Displacement noise is first turned into noise at the PLL frequency shift output, and then it is turned into voltage noise by the Kelvin controller. Each component introduces another transfer function into the system. The transfer of displacement to frequency shift noise in a PLL setup was derived and experimentally verified by Lübbe *et al.* [32]. Diesinger, Deresmes & Mélin [63] similarly modelled and analysed the transfer of deflection noise through PLL and Kelvin feedback. They arrived at the Kelvin voltage noise and defined a figure of merit for different probes. As long as PLL and Kelvin feedback are stable, noise was neither increased nor were other noise sources introduced.

As we will show now, the sideband transfer function as derived in section 2.3 gives us a direct approach to a Kelvin voltage noise density as a function of ω_m. By detecting the sidebands directly, we are furthermore free in our choice of ω_m since we do not require a PLL anymore. As in the discussion about noise in FM-AFM, section 2.4, $d^\mathrm{z}_\mathrm{tot}$ is the total deflection noise density with contributions of thermal and detection noise. Using the sideband amplitude as a function of voltage error, eq. (3.6), and the sideband transfer function, eq. (2.11), we define a signal-to-noise ratio for each sideband and set it to unity

$$\mathrm{SNR} = \frac{\frac{A}{2k}\left\langle\frac{\partial^2 C}{\partial z^2}\right\rangle U_\mathrm{ac}|G(\omega_\mathrm{d}\pm\omega_\mathrm{m})|\, n^\pm_\mathrm{k}(\omega_\mathrm{m})}{d^\mathrm{z}_\mathrm{tot}(\omega_\mathrm{d}\pm\omega_\mathrm{m})} \stackrel{!}{=} 1. \tag{3.11}$$

Here, $n^\pm_\mathrm{k}$ is the (single-sided) Kelvin voltage noise density in $\mathrm{V\,Hz^{-0.5}}$ for the sideband at $\omega_\mathrm{d} \pm \omega_\mathrm{m}$, respectively.

Solving for $n_k^{\pm}$, we arrive at

$$n_k^{\pm}(\omega_m) = \frac{1}{\frac{A}{2k}\left\langle\frac{\partial^2 C}{\partial z^2}\right\rangle U_{ac}} \frac{d_{tot}^z(\omega_d \pm \omega_m)}{|G(\omega_d \pm \omega_m)|} \tag{3.12}$$

$$= \frac{1}{\frac{A}{2k}\left\langle\frac{\partial^2 C}{\partial z^2}\right\rangle U_{ac}} \sqrt{\frac{4k_B T}{kQ\omega_0} + \frac{D_{ds}^z}{G^2(\omega_d \pm \omega_m)}}. \tag{3.13}$$

In the last step, we have used the explicit expression of thermal and detection noise. The cantilever transfer function in the denominator of eq. (3.12) cancels the transfer function in d_z^{th}. For low modulation frequencies, the voltage noise is thus essentially white. For larger modulation frequencies, the voltage noise density scales with $1/|G(\omega_d \pm \omega_m)| \propto \omega_m$.

Both sidebands usually have the same sensitivity and noise for $\omega_d \approx \omega_0$. Because we add them coherently and use both of them for Kelvin feedback, the total noise density is reduced by $\sqrt{2}$,

$$n_k^{tot}(\omega_m) \approx \frac{n_k^{\pm}(\omega_m)}{\sqrt{2}} \approx \frac{1}{\left\langle\frac{\partial^2 C}{\partial z^2}\right\rangle U_{ac}} \sqrt{\frac{8kk_B T}{Q\omega_0 A^2}} \sqrt{1 + \left(\frac{\omega_m}{2\pi B_{th}}\right)^2}. \tag{3.14}$$

Here, we have approximated the transfer function for ω_m beyond the cantilever bandwidth, ω_c, and assume drive near resonance, $\omega_d \cong \omega_0$. We have also expressed the correction due to noise in the detection system by the bandwidth for thermal noise limited measurements, B_{th}, eq. (2.22).

Equation (3.14) allows us to estimate the *rms* Kelvin voltage noise for a chosen modulation frequency, ω_m, by integrating over the Kelvin lock-in and feedback bandwidth, B, around ω_m. The first square root of eq. (3.14) is $k_{ts}^{min}/\sqrt{B}$, the minimum detectable force gradient we derived in section 2.4. We can thus easily verify that n_k^{tot} is simply the force gradient noise density divided by $C'' U_{ac}$.

At modulation frequencies below B_{th} thermal noise limits the attainable potential resolution in U_{lcpd}. Above B_{th}, the noise density increases linearly with ω_m. Therefore, ω_m should be chosen as low as possible but large enough to reject variations in k_{ts} during the scan.

For a given cantilever, noise can be reduced by staying close to the surface and thereby increasing C''. Noise is also reduced by increasing the modulation voltage, although care should be taken to avoid band bending with semiconducting tips or samples.

When limited by detection noise, $n_{\mathrm{k}}^{\mathrm{tot}}$ becomes independent of the quality factor:

$$n_{\mathrm{k}}^{\mathrm{tot}}(\omega_{\mathrm{m}} \gg 2\pi B_{\mathrm{th}}) = \frac{2\sqrt{2k}}{A\left\langle \frac{\partial^2 C}{\partial z^2} \right\rangle U_{\mathrm{ac}}} \frac{\omega_{\mathrm{m}}}{\omega_0} d_{\mathrm{ds}}^{\mathrm{z}}. \tag{3.15}$$

We can therefore expect best performance for cantilevers with low spring constants, k, and high resonant frequencies, ω_0. Note that detection system limited noise scales $\propto k/\omega_0$ whereas the thermal noise is $\propto \sqrt{k/\omega_0}$; thus, large frequencies are even more so important to reduce the contribution of the detection system. Large resonant frequencies make it also possible to operate at higher bandwidths for AM topography, since transient oscillations decay faster for similar quality factors.

A future strategy to reduce Kelvin voltage noise must therefore be the use of short cantilevers with high resonant frequency but maintaining the stiffness of cantilevers employed today. The detection system needs to be adapted for these short cantilevers, typically just ≈10 µm in length, to enable operation at high frequencies and with a small laser spot diameter [67, 68].

For a given cantilever geometry and oscillation amplitude, the noise is reduced by increasing the sensitivity AC'', where C'' is averaged over the oscillation cycle[4] according to eq. (2.4). With the analytical derivations of the tip–sample force available in literature, e.g. in Hudlet *et al.* [62], we can thus plot AC'' as a function of A and distance, d. Figure 3.4a shows this sensitivity for the cantilever geometry used to compare AM- and FM-KFM, fig. 3.1. At constant amplitude the sensitivity increases by approaching the surface. At constant distance,[5] the amplitude can be chosen for optimal sensitivity. At a distance of 1 nm and an amplitude of 10 nm, we find $C'' = 8.8\,\mathrm{fF\,\mu m^{-2}}$, which is comparable to values we see experimentally.[6] With this value, we plot in fig. 3.4b the Kelvin noise density as a function of modulation frequency, f_{m}, for $Q = 500$ and $Q = 5000$. At 4 kHz we find ≈1 mV Hz$^{-0.5}$ in both cases, or ≈10 mV in a 100 Hz bandwidth. At 1000 Hz, a noise level of ≈3 mV would be feasible with $Q = 5000$. Lower *rms* noise levels could be achieved at reduced detection bandwidths, by averaging multiple samples, or at cost of lateral resolution by using slightly blunt or coated tips. While maintaining k, a tenfold increase in resonant frequency could reduce noise by another ≈70 . . . 90 %. Lastly, when limited by detection noise, $d_{\mathrm{ds}}^{\mathrm{z}}$ must be reduced.[7]

4 Because the effective C'' is coupled to the oscillation amplitude, optimising a single parameter is not enough—the product AC'' matters.

5 Under closed-loop conditions, this distance depends on Δf (or the amplitude setpoint) and details of the interaction forces.

6 For handy values we give C'' in $\mathrm{fF\,\mu m^{-2}} = 1 \times 10^{-3}\,\mathrm{F\,m^{-2}} = 1 \times 10^{-3}\,\mathrm{N\,m^{-1}\,V^{-2}}$. The latter conversion is in terms of a force gradient.

7 Note that for the fundamental eigenmode and beam deflection AFMs limited by shot noise, the SNR is maximised when the laser spot illuminates the cantilever over the full length [37].

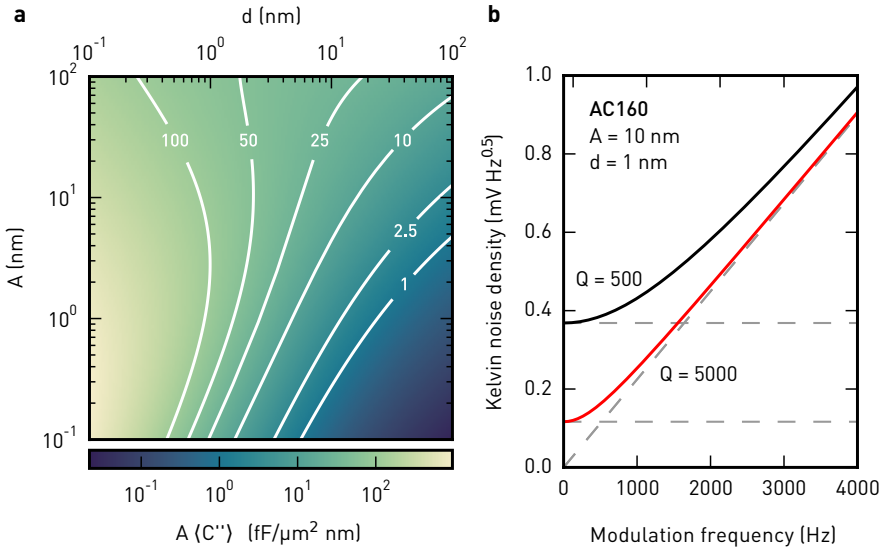

FIGURE 3.4: (a) Simulated electrostatic sensitivity, $\langle C'' \rangle A$, for the cantilever in fig. 3.1 as a function of closest approach, d, and amplitude, A. (b) Expected Kelvin noise density for this cantilever at $Q = 500$ and 5000 at an amplitude of 10 nm, a distance of 1 nm, and 1 V modulation. Asymptotes for detection noise and thermal noise limited operation are shown as dashed lines. (Parameters: $T = 300$ K, $f_0 = 300$ kHz, $k = 30$ N/m, $d_{ds}^{z} = 70\,\mathrm{fm\,Hz^{-0.5}}$)

3.5 CONTROL STRATEGIES AND CROSSTALK

There are two major methods to find the local contact potential difference at every point during the scan. *Open-loop* KFM exploits the fact that the $2\omega_m$ amplitudes do depend on C'' but not on $U_{dc} - U_{lcpd}$. As demonstrated in fig. 3.3, the ratio of the ω_m and $2\omega_m$ sidebands is independent of changes in C'' and only depends on the chosen modulation amplitude and *dc* bias,

$$\frac{X(\omega_d \pm \omega_m)}{A(\omega_d \pm 2\omega_m)} = \pm\frac{8}{U_{ac}}(U_{dc} - U_{lcpd}) = \pm K'(U_{dc} - U_{lcpd}), \tag{3.16}$$

hence U_{lcpd} can easily be determined. Note, however, that the above definition of the prefactor K' is only valid for modulation frequencies well beyond the cantilever bandwidth. In the general case, $K' = (4/U_{ac})G(\omega_d \pm \omega_m)/G(\omega_d \pm 2\omega_m)$, that is, it also depends on the resonant frequency and the quality factor, which may change while scanning. Furthermore, there may be differences in the sideband phase shift

when Q or ω_0 are not constant (cf. fig. 2.1). Together, such inaccuracies in the model easily translate into uncertainties of U_{lcpd} in an open-loop method. A PLL can reduce these effects, but then its transfer function needs to be considered as well [69], and the bandwidth must be larger than $2\omega_{\mathrm{m}}$.

In *closed-loop* KFM, the local contact potential difference is found by nullifying the in-phase components of the ω_{m} sidebands (eq. (3.9)) with a feedback loop adjusting the applied *dc* voltage [20, 44, 45, 54]. Thus, the $2\omega_{\mathrm{m}}$ sidebands are not necessary to determine the CPD, and the effect of model deviations and non-linearities is cancelled by the feedback. Furthermore, the nulling process also minimises the *dc* electrostatic force and force gradient (eq. (3.6)), reducing electrostatically induced height errors [60, 70, 71].

However, a few critical issues remain with simple Kelvin feedback loops. For example, when the sidebands are not completely nullified by the feedback, leaving a small error δ, it follows from eq. (3.9) that $U_{\mathrm{dc}} - U_{\mathrm{lcpd}} \propto \delta / C''$ [72]. C'' depends strongly on the electrostatic interactions between tip and surface and may change significantly on structured surfaces even for a well-tuned topography controller. During a scan, imperfect Kelvin feedback therefore leads to errors in the measured CPD, constituting a source of topography-induced crosstalk.

If additional apparent forces (or force gradients) are detected at the frequencies used for KFM, the Kelvin feedback does not compensate the CPD, but rather nullifies the in-phase component affected by offsets [65]. Such crosstalk is due to parasitic capacitive coupling and observed mainly in AM-KFM, where the electrostatic modulation is at high frequencies [73]. When coupling to the shaker piezo [74], cantilever resonances can amplify this effect.

Another source of crosstalk can appear when ω_{m} is set too low and the Kelvin lock-ins capture the modulation of k_{ts} induced by topography. This can happen on highly structured surfaces when the bandwidth of the topography feedback is insufficient for the scan speed. By monitoring the deflection power spectral density near the driving frequency, an upper frequency bound of the remaining k_{ts} modulations can be determined. In order to avoid crosstalk, ω_{m} should be chosen above this bound, considering both the bandwidth and filter steepness of the Kelvin lock-ins.

As already mentioned, tuning the Kelvin feedback loop itself can be a challenge because its sensitivity depends on C''. This becomes even more acute for small tip–sample distances and single-scan techniques on structured surfaces, where the tip–surface interaction is not limited to the apex.

In order to address the topography crosstalk due to C'', Lee, Lee & Prinz [75] suggested to use a feedback signal normalised to the $2\omega_{\mathrm{m}}$ sideband, thus rendering the CPD tracking error independent of C'' (cf. eq. (3.16)). However, as shown in

fig. 3.3c, the normalisation procedure may introduce additional noise when dividing by small signals, e.g. for low U_{ac}.

3.6 OPTIMAL CPD ESTIMATION AND KELVIN CONTROL

Most instruments provide a generic PID controller for Kelvin control, which compares the signal (X_ω) to a setpoint (0), yielding the error signal e. The sum of e, $\int e\mathrm{d}t$, and $\mathrm{d}e/\mathrm{d}t$, scaled by respective proportional (P), integral (I), and derivative (D) gains, is fed back into the system. In case of KFM, the resulting *dc* voltage compensates the electrostatic interactions. This standard PID feedback loop is illustrated in fig. 3.5a. Knowing the system dynamics, a multitude of tuning rules can be applied (e.g. Ziegler & Nichols [76]). In practice, however, the feedback gains are often tuned by trial and error, and the derivative part is omitted altogether [77]. In many cases, only the integral part is necessary for good tracking and to eliminate steady-state errors. Integral-only controllers are therefore prevalent for topography or Kelvin feedback.

Controllers basing their actions on an error signal only are unaware of the systems they control. Thus, they need to be retuned as soon as the system bandwidths or gains change considerably, either due to different operator settings or, more importantly during KFM scans, due to local variations of electronic properties and topography of the sample. To maintain best feedback settings at every location during a scan, we introduce a novel controller for FM-KFM based on stochastic optimal control [78]. Optimal control and model-based controllers have been successfully used before in AFM, e.g. for active damping of cantilevers [79] or fast scanning [80]. According to the separation principle [78], the optimal controller that minimises the expected error can be constructed by finding an optimal 'observer' and an optimal 'regulator'. As an observer, we use a Kalman filter [81] which continuously blends the sideband measurements at $\pm\omega_{\mathrm{m}}$ into an estimate of the contact potential difference, $\hat{U}_{\mathrm{lcpd}}$, based on a simplified model of the FM-KFM detection system. The Kalman filter is the stochastically optimal observer that minimises the state error covariance [78], taking into account both measurement noise and the uncertainties in the knowledge of its state. Adapted for KFM control, the Kalman filter minimises the estimation error variance of the surface potential, $\left\langle (U_{\mathrm{lcpd}} - \hat{U}_{\mathrm{lcpd}})^2 \right\rangle$. Since the aim of the regulator in KFM is to minimise electrostatic interactions, the optimal regulator is found by matching the *dc* bias to $\hat{U}_{\mathrm{lcpd}}$, thereby closing the feedback loop (fig. 3.5b).

Our Kalman filter design based on a model of the KFM detection system includes the sideband dynamics, eq. (2.11), the electrostatic force gradients acting on the cantilever, eqs. (3.7) and (3.8), and the transfer function of the demodulating lock-in amplifier. Since the lock-in bandwidths must be kept well below ω_{m} to avoid car-

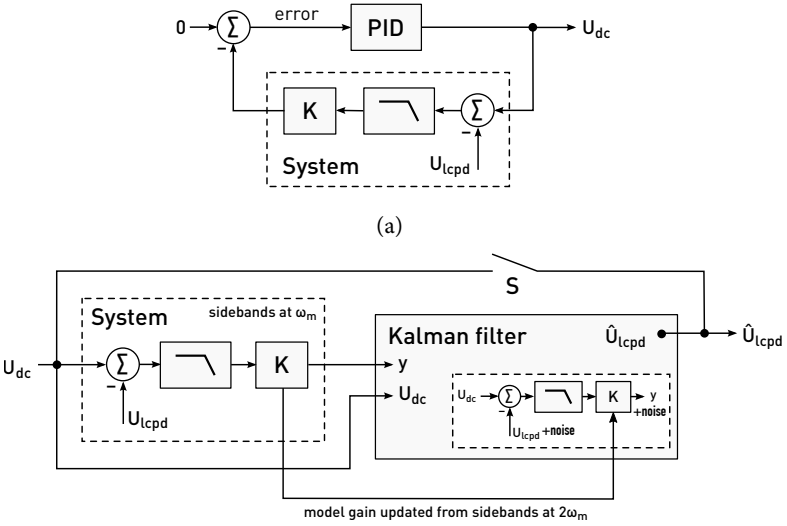

FIGURE 3.5: Block diagram of a Kelvin controller based on (a) a proportional-integral-differential (PID) controller, and (b) the Kalman filter. In the PID controller, the system output is compared to a setpoint to yield the error signal. The output signal, i.e. the sum of amplified errors and their respective integral or derivative, is fed back into the system. When the system output is nullified (setpoint 0), the controller output U_{dc} equals the surface potential U_{lcpd}.
Knowing an approximate model of the system, the Kalman filter instead estimates $\hat{U}_{\mathrm{lcpd}}$ solely based on the system output and the applied *dc* bias, U_{dc}. With the switch *S* closed, the estimated surface potential $\hat{U}_{\mathrm{lcpd}}$ is applied as the *dc* bias, corresponding to a feedback configuration.

rier and topography crosstalk, the sideband transfer functions reduce to an effective gain and phase, eq. (2.14). The lock-in transfer function can either be measured or is known from its filter properties. We focus on a particular case, the n-th order critically damped lowpass filter formed by n consecutive first order stages with a time constant τ. With these considerations, the transfer function for the lock-in in-phase components is $G(s = i\omega) = K(1 + \tau s)^{-n}$, where, following eq. (3.9), we obtain the static gain $K \propto C'' U_{\mathrm{ac}}$ and the system output $G(s)(U_{\mathrm{dc}} - U_{\mathrm{lcpd}})$.

Based on the transfer function, we find a state-space model of the system, in which we incorporate U_{lcpd} as a *hidden* state, and U_{dc} is the control signal. We further model the uncertainties of state transitions ($\dot{U}_{\mathrm{lcpd}}$) and our measurements as uncorrelated zero-mean white noise with power spectral densities V and W, respectively. Hence, U_{lcpd} follows a Wiener process or Brownian motion [78]. For a derivation of the continuous-time Kalman(-Bucy) filter [82], see appendix A.2. In discrete time, the Kalman filter is similarly found from a discrete-time state-space model [81]. In this formulation the state estimate and covariances are refined recursively as new measurements are incorporated:

At the time t, an *a priori* state and covariance estimate is found using the state and covariances at the time $t - \Delta t$, based on the system model. Then, the Kalman gain L is computed from the covariance matrices of the *a priori* estimated state and the system model. L controls the innovations process, in which the measurements at the time t are incorporated to the *a posteriori* estimate of state and covariances [83].

This recursive predictor-corrector structure allows for updates of the system parameters, such as the static gain K, at each instant of the state update. With eq. (3.16), the 2ω sideband amplitudes can thus be exploited to continuously update $K = K' A_{2\omega}$. Consequently, the observer model will follow changes in the Kelvin signal strength due to variations of C''. This strategy avoids normalisation by potentially noisy C'' signals [75], yet changes in C'' do not affect closed-loop performance. We demonstrate this in fig. 3.6, where we compare step responses of the closed-loop Kalman observer and PI controller. As soon as the gain K drops, the noise level increases with a PI controller, whereas the Kalman estimate remains clean.

To further elucidate the performance of the controller, we plot in fig. 3.7 its −3 dB closed-loop bandwidth, normalised to the −3 dB filter bandwidth, as a function of the normalised noise power spectral densities $\tilde{V}$ and $\tilde{W}$ of state transitions and observations, respectively. As the noise at the output, $\tilde{W}$, increases for a fixed $\tilde{V}$, the bandwidth is reduced (fig. 3.7a). The ratio $\tilde{V}/\tilde{W} \propto (\tau K)^2 \approx K^2/\mathrm{BW}^2$ resembles a signal-to-noise ratio (SNR), which increases for large K and small filter bandwidths BW. The closed-loop bandwidth is a function of this SNR. Therefore, in addition to avoiding divisions by small signals, the Kalman filter improves noise performance by bandwidth adjustments. For normalised closed-loop bandwidths $\lesssim 1$, the band-

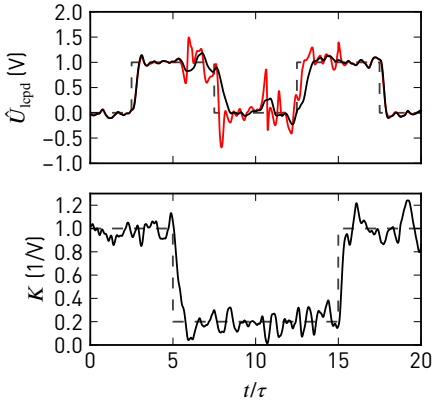

FIGURE 3.6: Closed-loop response of the Kelvin observer (black) and a proportional-integral controller (red) to steps in U_{lcpd} and K. Both controllers incorporate the separately measured static gain, K, and are tuned for similar step responses at high K. Noise in K and at the inputs is artificial white noise lowpass-filtered with $\tau f_{\mathrm{cut}} = 1$ and the filter order $n = 4$, as in the simulated system.

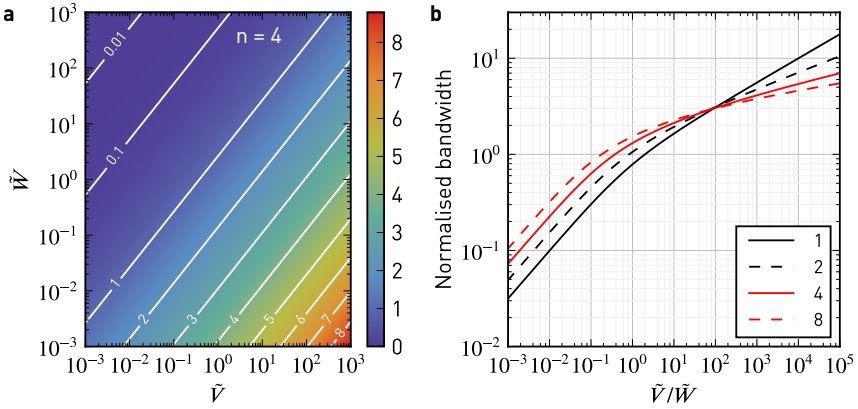

FIGURE 3.7: Normalised closed-loop bandwidth (−3 dB) of the steady-state Kelvin observer as a function of the normalised power spectral densities $\tilde{V} = \tau V$ and $\tilde{W} = W/\tau K^2$ for different orders of the low-pass filter, n. (a) Two-dimensional map for $n = 4$. As the observation noise density, $\tilde{W}$, increases for a fixed transition noise density, $\tilde{V}$, the closed-loop bandwidth is reduced. (b) Closed-loop bandwidth normalised to the bandwidth of the corresponding n-th order low-pass filter.

width is adjusted following $\sqrt{\tilde{V}/\tilde{W}}$ (fig. 3.7b). Larger bandwidths are not desired, since they would counteract the lock-in lowpass action.

Implementation

The setup is shown in fig. 3.8. We implemented the Kalman-filtering Kelvin controller as a real-time program on the digital signal processor (DSP) of a digital lock-in amplifier and PLL (HF2, Zurich Instruments), which demodulates the sidebands at $\omega_\mathrm{d} \pm \omega_\mathrm{m}$ and $\omega_\mathrm{d} \pm 2\omega_\mathrm{m}$ as well as the carrier signal at ω_d. Since the implementation of the Kalman filter is integrated into the lock-in, all signals are available without additional digital/analogue/digital conversions, avoiding additional offsets that might affect the feedback accuracy. The Kalman filter is implemented as a reusable component in C++ using the Eigen template library for linear algebra [84], allowing us to perform offline tests with the same code that is compiled for the DSP. In its current state, our custom FM-KFM controller can work at sampling rates of up to 7200 Sa/s.

Since the sideband signals are detected individually, we do not depend on the Δf signal as in a typical FM-KFM setup. Therefore, the Kelvin feedback remains the same for AM and FM topography feedback schemes. For example, on samples with coarse topography one may use AM topography feedback to avoid instabilities typically experienced with FM operation. In vacuum, this may require additional application of active Q control [85, 86] to lower the Q-factor of the cantilever.

3.7 CONCLUSION

In this chapter, we have introduced Kelvin probe force microscopy as a quantitative technique to obtain the surface potential with high lateral and potential resolution.

The force and force gradient sensitive KFM detection schemes were compared. We emphasised why detection of force gradients is important especially for the characterisation of nanoscale electronic devices. Furthermore, we have shown that operation close to the surface is important to localise the detection volume underneath the tip apex.

We have derived the expected voltage noise density for different Kelvin modulation frequencies. For a model cantilever, we computed the expected sensitivities as a function of oscillation amplitude and distance. Directions for proper choice of ω_m were given, and we concluded that the use of high frequency cantilevers with low spring constants will enable improved noise figures.

We also derived the sideband amplitudes originating from the Kelvin modulation in FM-KFM. Here, we note that the sideband transfer function also explains the higher resolution obtained by heterodyne amplitude-modulated KFM [87]. In this

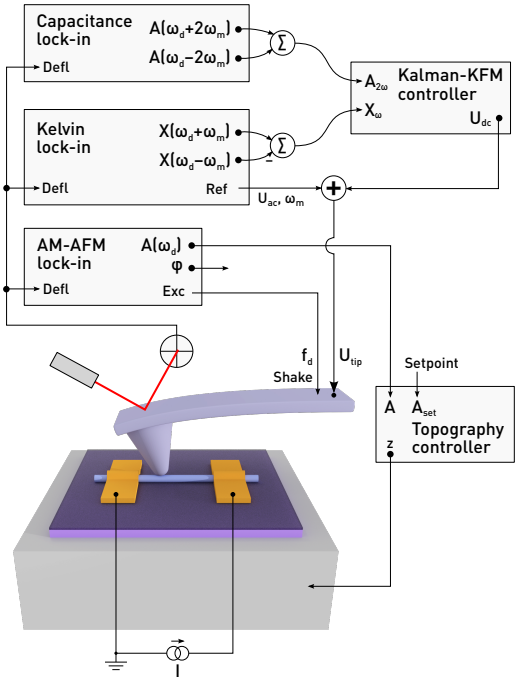

FIGURE 3.8: Schematic of the modified KFM setup. For topography feedback, the cantilever is excited at a constant frequency ω_d close to resonance. Lock-in amplifiers at $\omega_\mathrm{d} \pm \omega_\mathrm{m}$ and $\omega_\mathrm{d} \pm 2\omega_\mathrm{m}$ detect sidebands of the cantilever oscillation which contain information about the surface potential and tip–sample capacitance. Both contributions are used by the Kalman-KFM controller for the CPD estimate.

technique, the cantilever is driven mechanically at ω_0 and electrically at $\omega_\mathrm{m} = \omega_1 - \omega_0$, where ω_0 and ω_1 are the cantilever's lowest two eigenfrequencies. Accordingly, the sideband at $\omega_0 + \omega_\mathrm{m}$ coincides with the cantilever's second eigenmode, resulting in an amplified signal proportional to the electrostatic force gradient instead of the electrostatic force.

Direct demodulation of sidebands as well as knowledge of the sideband transfer function made it possible to introduce a Kalman filter for Kelvin control. Similarly, Magonov & Alexander [88] demonstrated a setup in which the modulated force gradients are detected from the phase output of the carrier oscillation lock-in, requiring ω_m to be within its bandwidth. With direct sideband detection, the detour via

a phase modulation is avoided, and ω_m can be chosen independently of the lock-in bandwidth to achieve best separation from topography.

We have discussed benefits of the Kalman-KFM controller, how it can adjust its model to the changing sensitivities during the scan, and how this helps to reduce feedback errors. The Kalman filter maintains stable feedback at the expected noise levels without operator intervention. At the same time, we would like to point out that *using* the Kalman-KFM controller is not more complicated. Since it automatically incorporates lock-in filter settings and the system sensitivity, the only parameters left to tune are the noise power spectral density of the U_lcpd transitions and sideband observations. Because the latter is easily determined from a power spectrum near the sidebands, the controller performance can be tuned in practice using the transition noise only.

We still see several aspects for further improvement of KFM feedback. For example, the dynamics of U_lcpd are currently modelled as white noise within our scheme. Since successive lines in AFM scans only change slightly, information from the previous line could be incorporated, similar to a feed-forward controller [71]. Other state estimators could also be integrated, including H-∞ filters for minimising the worst-case error [83].

4

KELVIN PROBE FORCE MICROSCOPY OF NANOWIRE DEVICES

The beauty of a living thing is not the atoms that go into it, but the way those atoms are put together.

— Carl Sagan

In this chapter we demonstrate the Kalman-KFM controller from section 3.6 on active devices made of indium arsenide (InAs) nanowires. Such devices exhibit some of the most typical and relevant issues hindering reliable KFM measurements in the past: a combination of large topography with a multitude of different materials, including oxides prone to charging.

Oftentimes the contact resistances between the nanowire and metal contacts are uneven and large, obscuring the electrostatics of devices. Traditional four-point measurements are limited at sub-micron length scales because the contact length can become comparable to the channel dimensions. For such samples, KFM appears to be an ideal tool to characterise the electrostatics in order to optimise device performance, for example as field effect transistors or as thermoelectrics.

We have mentioned before that FM-KFM measurements on nanoscale devices are normally challenging. In the past, most measurements were therefore conducted primarily with AM-KFM in lift mode or at the second eigenmode. By taking care of convolution effects, it was still possible to investigate Schottky junctions in silicon (Si) nanowires [47], and to measure the surface state density [46] and sub-bands [89] of InAs nanowires. Issues with large-scale averaging with AM-KFM were also noticed for example by Quitoriano *et al.* [90].

When device dimensions approach the dimensions of the probe, stray coupling to electrodes, particularly unscreened gates, also needs to be addressed in FM-KFM. For this situation, Fuller *et al.* [91] demonstrated an experimental approach to determine capacitive coupling coefficients from the tip to different parts of a nanoscale device.

We now first demonstrate the performance of the Kalman-KFM controller on an InAs nanowire. Then, on another nanowire, we obtain one-dimensional profiles of the surface potential at different bias currents. We will show how static surface potential offsets and measurement noise in such a constellation can be addressed by

Parts of this chapter have been published in *Beilstein J. Nanotechnol.* **6**, 2193 (2015) [2].

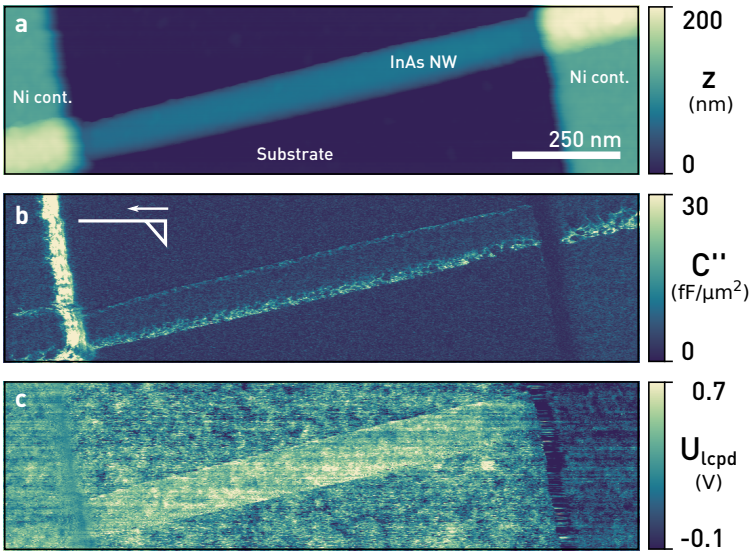

FIGURE 4.1: (a) Topography, (b) tip-sample capacitance gradient, C'', and (c) local contact potential difference, U_{lcpd}, of an InAs nanowire at a bias current of 1.4 µA. U_{lcpd}, determined by the Kelvin observer, exhibits no crosstalk. The inset in (b) indicates the tip shape and fast scan direction. (Scan parameters: A_{free} = 8.6 nm, A_{set} = 7.2 nm, Q = 390, k = 26 N/m, f_0 = 304.2 kHz, f_{m} = 4 kHz, U_{ac} = 1 V, f_{cut} = 100 Hz, n = 4, v_{tip} = 800 nm/s)

a least-squares profile reconstruction, allowing us to separate bias dependent and inhomogeneous contact resistances from properties of the channel.

4.1 PERFORMANCE OF THE KALMAN-KFM CONTROLLER

Figure 4.1 shows a scan of a 70-nm diameter indium arsenide nanowire with nickel (Ni) contacts (height ≈120 nm), obtained at a bias current of 1.4 µA in ambient conditions using a commercial AFM (Cypher, Asylum Research). The experimental setup was already depicted in fig. 3.8. Here, steep edges at the electrodes necessitated AM topography feedback.

Figure 4.1b displays the simultaneously acquired C'', calculated from the $2\omega_{\mathrm{m}}$ sideband amplitudes, eq. (3.10). To ensure highest lateral potential resolution, we used highly doped silicon AFM tips (Olympus AC160TS-R3) without a metal coating, which are sharp and not symmetrical at the apex (schematically depicted in the inset). This explains the increased C'' on the edge of the left electrode.

Figure 4.1c shows U_{lcpd} as estimated by the Kalman-KFM controller. Since its gain is continuously updated using the $2\omega_{\mathrm{m}}$ sidebands, crosstalk due to changes of C'' is absent from the scan. Near the left electrode edge the measured U_{lcpd} displays less spatial variation because also the sides of the tip are in close proximity to the electrode edge, increasing their contribution to the tip–sample capacitance and widening the KFM point spread function. Even though the Kalman-KFM controller remains stable and works unaffected by the increased C'', reaching up to seven times the mean value of the scan, the geometry of both tip and sample fundamentally limit the attainable resolution. The disturbances remaining on the edge of the right contact are due to imperfect topography feedback and accidental switches from net-attractive to net-repulsive tip-sample interactions. Most importantly, edge effects are absent at the boundaries of the nanowire. Long-range potential averaging due to the cantilever beam is absent due to the gradient-sensitive FM detection.

For an extraction of contact resistances, the voltage profile due to applied current needs to be separated from additional offsets in U_{lcpd}, such as spatial variations in work function. These can be obtained from a scan at zero bias (not shown). Knowing the potential drop at the contacts, the bias current, and assuming uniform material or transport properties, for the nanowire device in fig. 4.1 we hereby obtain a contact resistance of 40 kΩ at the left electrode, 150 kΩ at the right electrode, and a channel resistance of 50 kΩ.

In fig. 4.2, we compare the performance of our Kalman-KFM controller with a standard integral controller. Both controllers are tuned for optimised closed-loop performance on the nanowire. The integral controller exhibits ringing artefacts at the electrode edge, indicated by an arrow in fig. 4.2a, since the controller's gain margin is exceeded due to the increased C''. Such feedback oscillations should be avoided particularly in single-scan techniques, because they may perturb the topography controller. Next to the nanowire, where C'' is slightly reduced because of the gate oxide, the bandwidth of the feedback loop drops due to a lower gain.

As shown in fig. 4.2b, with the Kalman-KFM controller the feedback performance and image quality remain consistent during the scan. The error signal (X_ω) is almost featureless and its standard deviation reduces by about 30 % on average (excluding edge effects). Better tracking is also apparent from the power spectral densities of the error signals, depicted in fig. 4.3. For given lock-in filter bandwidths, the Kalman-KFM controller can nullify the $\pm\omega_{\mathrm{m}}$ sidebands faster and better than the integral controller, without adding to the noise level or introducing feedback artefacts.

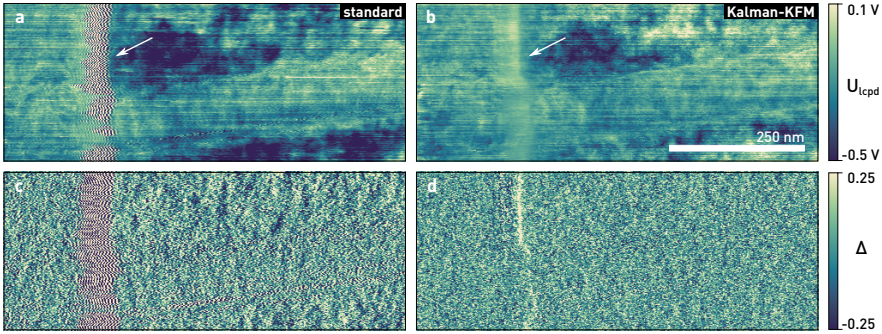

FIGURE 4.2: (a), (b) Kelvin and (c), (d) error signal of an InAs nanowire similar to the device shown in fig. 4.1, measured with a standard integral controller, (a) & (c), and the Kelvin observer, (b) & (d). Feedback oscillations, as indicated by the arrow, are absent in the Kalman control scheme, while the standard deviation of the error signal also decreases from 0.19 to 0.13. (Scan parameters: A_{free} = 11.2 nm, A_{set} = 9.6 nm, Q = 500, k = 35 N/m, f_0 = 304.5 kHz, f_m = 4 kHz, U_{ac} = 2 V, f_{cut} = 50 Hz, n = 4, v_{tip} = 250 nm/s; all images show raw data)

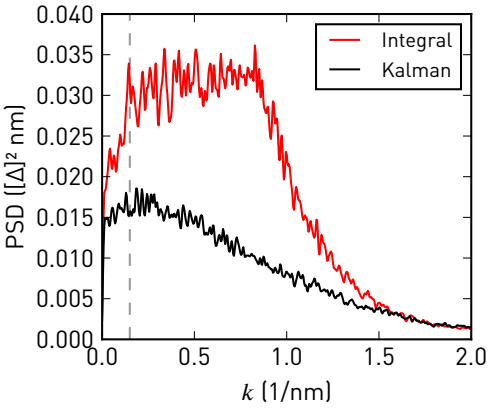

FIGURE 4.3: One-dimensional power spectral densities of the error signals in fig. 4.2 (c) & (d). Integral feedback works well at low spatial frequencies, k, but is unable to follow higher-frequency modulations. Kalman-KFM control consistently shows a lower error signal at all frequencies. In both cases the roll-off at high k is due to the Kelvin lock-in bandwidths.

4.2 POTENTIAL PROFILING AND CONTACT RESISTANCES

Field effect transistors are three-terminal devices in which a voltage applied to the gate electrode tunes the carrier density within the active channel, thereby modulating the conductance.[1] The flow of current between source and drain thus depends on electrode biases with their respective polarities.

In the semiconductor industry, device characterisation is done mostly from *output* and *transfer characteristics*, measuring current through the channel while sweeping the source–drain or gate bias, respectively. As devices become smaller, contact resistances play an increasing role, and the implementation and interpretation of four-point measurements gets more difficult.

We will now demonstrate how KFM measurements can enable a much deeper look into the channel behaviour than what is achievable by traditional transfer and output characteristics. In fig. 4.4 we show a measurement of an InAs nanowire with a diameter of 60 nm.

In addition to topography and surface potential at a single bias, shown in fig. 4.4a, we recorded surface potential profiles during sweeps of the two-terminal current. During continuous line scans along the nanowire, the current thereby assumed 50 different values from −37 µA to 38 µA. The measured surface potential is thus a function of position and current, $U_{\mathrm{lcpd}}(x, I)$, and shown in fig. 4.4b for selected currents. We can see that the measured U_{lcpd} on the left electrode stayed constant as the current I was swept, since this electrode was grounded. This again documents the reduction of long-range averaging in FM-KFM compared to AM-KFM, where an influence of applied voltages can be seen even on remote electrodes due to capacitive coupling of the cantilever beam. Changes of U_{lcpd} were observed only within the channel and at the right contact, which was biased. However, differences in work function between the InAs nanowire and the Ni contacts as well as spatially fluctuating charge traps in the passivation oxide[2] add a position-dependent offset voltage, $U^0_{\mathrm{lcpd}}(x)$. For device measurements, we are only interested in the effect of externally applied currents or voltages on U_{lcpd}. The offset therefore needs to be inferred, for example, from a profile measurement at zero bias. However, $U^0_{\mathrm{lcpd}}(x)$ can weakly depend also on voltage, since the population and depletion of traps is bias-dependent [48].

Having a complete set of profiles at different biases enables us improve upon this offset correction. Instead of subtracting simply the zero-bias profile, we determine

1 transistor ≙ *trans*fer res*istor*

2 Between recording the data in fig. 4.4a & b, both obtained with AM topography feedback and the Kalman-KFM controller, we tried to perform FM topography instead. Unfortunately, this procedure was not as gentle as it should be—PLL and amplitude controller did not track properly at wire boundaries and contacts, and the biased tip injected charges locally into the passivation oxide on top of the nanowire.

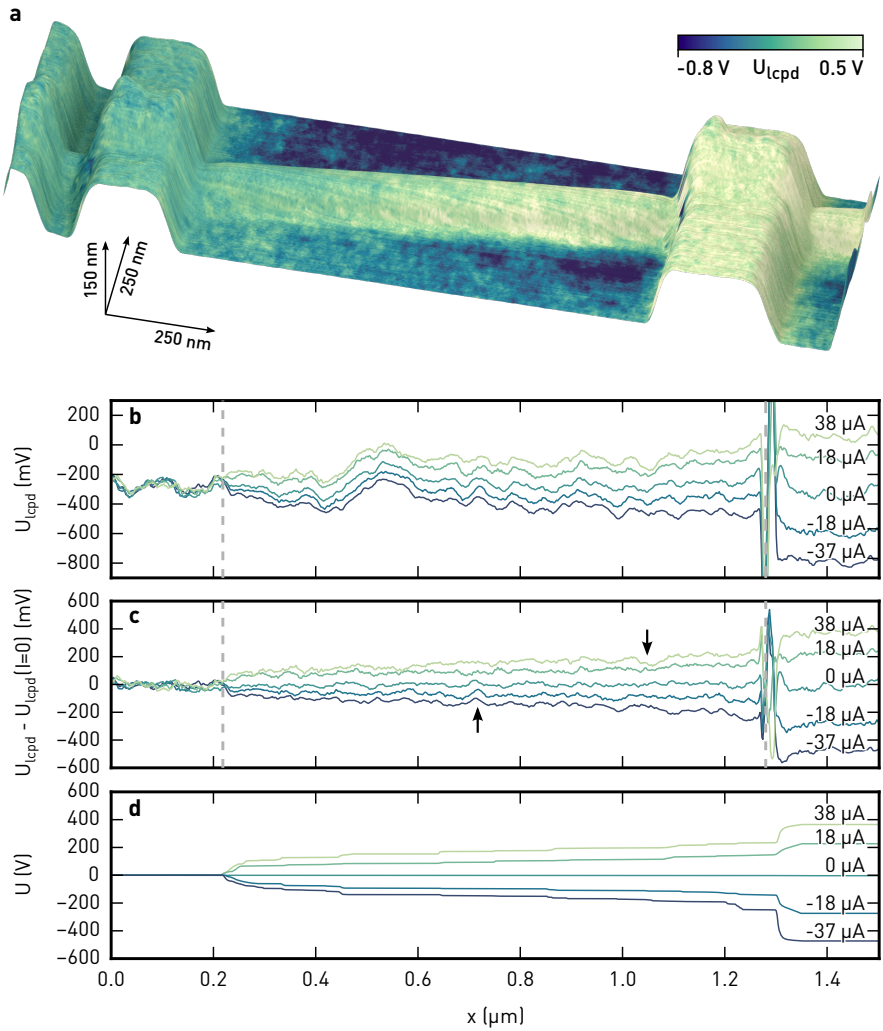

FIGURE 4.4: (a) Topography of a 60 nm InAs nanowire with superimposed surface potential at a current of 38 µA. (b) Surface potential along the wire at different source-drain currents. Due to trapped charges within the passivation oxide, there is an additional position-dependent voltage offset. (c) shows the induced voltage drop along the wire, where these position-dependent offsets have been eliminated by a constrained least-squares fit. The arrows indicate prominent deviations from a monotonous potential profile. (d) Profiles resulting from the fit. (Scan parameters: $A_{\mathrm{free}} = 8.5\,\mathrm{nm}$, $A_{\mathrm{set}} = 7.7\,\mathrm{nm}$, $Q = 500$, $k = 40\,\mathrm{N/m}$, $f_0 = 323.2\,\mathrm{kHz}$, $f_{\mathrm{m}} = 4\,\mathrm{kHz}$, $U_{\mathrm{ac}} = 2\,\mathrm{V}$, $v_{\mathrm{tip}} = 250\,\mathrm{nm/s}$)

an average $U^0_{\mathrm{lcpd}}(x)$ by a constrained least-squares fitting procedure, described in detail in appendix A.3. The measured surface potential is hereby decomposed as

$$U_{\mathrm{lcpd}}(x, I) = U^0_{\mathrm{lcpd}}(x) + U(x, I), \tag{4.1}$$

where $U(x, I)$ is the voltage profile induced by the applied current. The least-squares method ensures that the estimated offset $U^0_{\mathrm{lcpd}}(x)$ reduces the potential fluctuations due to traps on average. In fig. 4.4b the effect of $U^0_{\mathrm{lcpd}}(x)$ is very prominent, showing correlated features in every line profile. For $U(x, I)$ we need to postulate a functional dependence of the voltage on current, e.g. as a power series. We also require the voltage profile to increase (decrease) for increasing (decreasing) bias to the right electrode. This constraint to the fit ensures the potential to drop when power is dissipated, thereby preventing unexpected non-monotonic voltage profiles. One should carefully check that the resulting potential profiles faithfully reproduce the input data. For the fits shown here, we chose a non-linear dependence of $U(x, I)$ in every wire segment with up to 4th order corrections and different coefficients for positive and negative currents.[3]

Figure 4.4c shows the offset-corrected profiles, in which the correlated offsets are mostly removed. Remaining deviations from a monotonous potential profile (indicated by the arrows) hint at additional bias-dependent charge trapping in the passivation oxide, not addressed in the model. The profiles $U(x, I)$ reconstructed from the fit, shown in fig. 4.4d, enable a clear view onto both channel effects and potential drops at electrode boundaries.

With the data in fig. 4.4c & d, we now are able to perform virtual four-point probe measurements along the nanowire: Figure 4.5a is the two-terminal output characteristic, fig. 4.5b is the average voltage gradient of the wire only as a function of current, and fig. 4.5c & d are the resistances of the left and right contact, respectively.

Again, we find different contact resistances on both sides. Furthermore, whereas the left contact resistance is approximately symmetric around zero bias, the contact resistance on the right is clearly asymmetric. These contact effects could already be anticipated from the profiles in fig. 4.4c & d.

The mostly linear potential gradient within the wire as a function of current hints at largely ohmic behaviour. From a linear fit we extract $\langle \mathrm{d}U/\mathrm{d}x \rangle / I = 3.1\,\mathrm{k\Omega\,\mu m^{-1}}$, and multiplying by the wire cross-section, we find the specific resistance $\rho = 8.8\,\mu\Omega\,\mathrm{m}$ and conductivity $\sigma = 1/\rho = 1140\,\mathrm{S\,cm^{-1}}$.

Fuller *et al.* [48] used the average potential gradient, $\langle \mathrm{d}U/\mathrm{d}x \rangle$, to extract the mean free path, λ_{mfp}, within a single-walled carbon nanotube. The absence of contact ef-

3 There are limitations to the technique presented here. For example, we do not consider a bias-dependent buildup of charges or negative differential resistances along the wire. These effects would need to be addressed by extensions of the model.

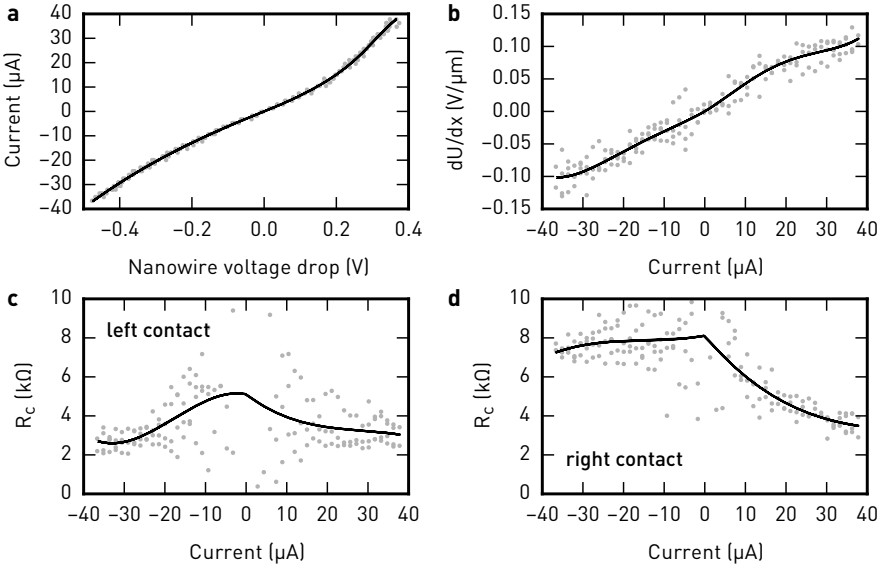

FIGURE 4.5: Extracted nanowire characteristics from the measurement shown in fig. 4.4. (a) Current through the nanowire vs. electrode voltage difference, (b) mean potential gradient within the wire, and contact resistances of the (c) left and (d) right contacts of the wire. The grey points are offset-corrected measurements from several sweeps. The solid lines use a non-negative least-squares fit of the potential profile at different currents.

fects in KFM measurements enabled this calculation. We can perform a similar analysis for our 60 nm nanowire as follows.

From the Landauer-Büttiker formalism, the total resistance, R_{tot}, of a quantum wire is [92]

$$R_{\mathrm{tot}} = \frac{h}{2e^2}\,\frac{1}{M}\left(1+\frac{1-\mathcal{T}}{\mathcal{T}}\right) = \frac{h}{2e^2}\,\frac{1}{M}\left(1+\frac{L}{\lambda_{\mathrm{mfp}}}\right), \tag{4.2}$$

where $h/2e^2 = 1/G_0 = 12.9\,\mathrm{k\Omega}$, M is the number of modes, and $\mathcal{T}$ is the mean transmission per mode. While the first term is a contact resistance independent of the wire length L, the second term is the resistance of the pure wire. By the latter, we can relate λ_{mfp} to the average potential gradient $\langle \mathrm{d}U/\mathrm{d}x\rangle = \Delta U/L$ at the current I by

$$\lambda_{\mathrm{mfp}} = \frac{1}{MG_0}\,\frac{I}{\langle \mathrm{d}U/\mathrm{d}x\rangle}. \tag{4.3}$$

The number of transverse modes M is related to the dimensions of a nanostructure and the Fermi wavelength, λ_f, of carriers in the material [92, 93]. For estimating the number of modes, we impose periodic boundary conditions.[4] For a two-dimensional shape of area A and perimeter P, the number of transverse energy eigenstates between wavevectors k and $k + \mathrm{d}k$ is [94]

$$\mathrm{d}N(k) = \left(\frac{A}{2\pi}k - \frac{P}{4\pi}\right)\mathrm{d}k. \tag{4.4}$$

At the Fermi level $E_f = \hbar^2 k_f^2/2m_{\mathrm{eff}}$ a mode can propagate for $|k| < k_f$. Hence, we need to count each energy eigenstate twice for the number of modes,

$$M(k_f) = 2\int_0^{k_f} \mathrm{d}N(k) = \frac{Ak_f^2 - Pk_f}{2\pi}. \tag{4.5}$$

We approximate the Fermi wavelength by the thermal de Broglie wavelength, $\lambda_{\mathrm{th}} = h/\sqrt{2\pi m_{\mathrm{eff}} k_B T}$. For InAs the effective mass of electrons is $m_{\mathrm{eff}} = 0.023 m_e$, and thus we get $\lambda_{\mathrm{th}} = 28.4$ nm at 300 K. From the topography scan, we find a nanowire diameter of ≈60 nm. Using eq. (4.5), $A = \pi d^2/4$, and $P = \pi d$, we thus find ≈15 propagating modes.

Using eq. (4.3) and the gradient extracted above, we can determine the mean free path to $4.2\,\mu\mathrm{m}/M \approx 280$ nm. This value is in good agreement with the ≈125 nm measured at 94 K for an InAs nanowire with 20 nm diameter[5] extracted by Philipp Mensch [95], who also fabricated the nanowire shown here. He obtained the mean free path from current–voltage characteristics at different segment lengths, requiring a number of purposefully designed contacts to the wire, whereas by KFM we could extract λ_{mfp} directly from a single two-terminal device.

With M propagating modes, we can estimate from the first term in eq. (4.2) a total contact resistance of $12.9\,\mathrm{k\Omega}/M \approx 0.86\,\mathrm{k\Omega}$.[6] The higher resistances seen in fig. 4.5c & d for both contacts and their bias dependence hint at further contributions of a Schottky barrier.

4.3 CONCLUSION

We have tested the performance of the Kalman-KFM controller on an InAs nanowire device with rough surface and abrupt height variations, which pose severe challenges

4 For a 1-dimensional channel of width W, one expects $M = W/(\lambda_f/2)$ modes [93].

5 Note that the 20 nm should only accommodate a single mode, removing the error in the estimation of M.

6 This assumes a contribution of M equivalent modes to the contact resistance. In general, the transmission of each mode at the contacts and within the wire needs to be regarded, leading to differently quantised conductances [96]. For this reason, the estimate should rather be seen as a lower bound.

to both traditional single-scan and lift-mode FM-KFM setups. Since direct sideband demodulation allowed us to perform FM-KFM irrespective of the topography feedback, we could perform these scans with amplitude modulation in air. Compared to standard integral feedback, the Kalman-KFM controller was demonstrated to track the surface potential better and without adding to the noise level, while it reduced feedback artefacts at the same time.

We have demonstrated in detail how KFM makes it possible to separate inhomogeneous and bias-dependent contact resistances from intrinsic channel properties. This was facilitated by profiles of the surface potential under different bias conditions from which we inferred position-dependent offsets. Such offsets, caused by local charging or differences in work function in heterostructures, are inevitable in every measurement of the surface potential.

For this two-terminal device, we extracted both contact resistances and the channel conductivity, and we could estimate the mean free path within the wire. Future investigations on wires with smaller diameter at different temperatures could shine light on the different scattering mechanisms.

Using KFM for device characterisation promises great opportunities for the future. For example, the backgate was kept at ground in our study. But similar to the extracted output characteristics in fig. 4.5a & b, transfer characteristics could be obtained. The influence of the gate electrode on the carrier density would furthermore be seen also in U_{lcpd}, because it embodies differences in the Fermi level of tip and surface [50].

High resolution measurement of potential profiles will also prove beneficial in combination with scanning thermal microscopy (SThM) [97]. Each resistive component along the wire causes a directly accessible voltage drop ΔU at the current I, thereby dissipating power as $I\Delta U$. The effects of this Joule heating are directly imaged in SThM and can be separated from Peltier effects in thermoelectrics [98], opening the avenue to combined high-resolution quantitative thermometry and potentiometry of nanostructures.

5

THE POTENTIAL LANDSCAPE OF NANOPARTICLE NETWORKS

> *But see that the imagination of nature is far, far greater than the imagination of man. No one who did not have some inkling of this through observations could ever have imagined such a marvel as nature is.*
>
> — Richard P. Feynman, *The Meaning of It All*

As transistors continue to shrink to mere nanometres in dimension, they approach the limits of traditional semiconducting materials. The number of atoms within the channel becomes countable, and thus we cannot treat the channel as a bulk material anymore. Discrete levels rather than energy bands now govern the electronic world.

In a pioneering thought experiment, Aviram & Ratner [99] suggested the use of molecules as fundamental building blocks for electronic devices already in 1974. But only recently this challenge could be tackled also experimentally. While chemists can produce tailored molecules in industrial quantities, integration into functional devices also requires electrical contacts.

On a small scale, but with single-molecule precision, this was enabled for example in mechanically controlled break junctions [100] or by STM [101]. On a larger scale, a viable route could be one- or two-dimensional arrangements of colloidal gold nanoparticles formed by self-assembly. They promise to provide a molecular breadboard, in which different kinds of molecules may be inserted into the nanometre-sized gap between adjacent nanoparticles [102, 103].

Until now, electronic transport through such arrangements of nanoparticles has been studied mostly by current measurements through macroscopic contacts on either side of the network [104–106]. The current obtained thereby, however, averages over hundreds to thousands of junctions, potentially obscuring the local behaviour within the network.

In contrast, Kelvin probe force microscopy allows us to measure voltage drops within the nanoparticle networks down to the level of individual junctions. We will shortly see that the potential landscape often exhibits rather distinct terraces that appear because of inevitable disorder in the network or in the molecular interconnects.

The typical experimental setup for experiments in this chapter is illustrated in fig. 5.1. Devices consist of 10 nm-diameter gold nanoparticles synthesised in aqueous solution [107]. The nanoparticles were then capped with alkanethiols (octane-

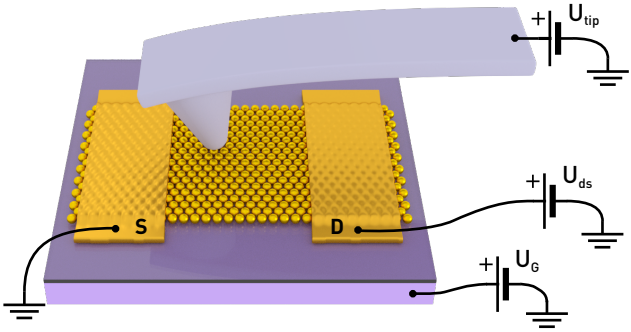

FIGURE 5.1: Schematic of a nanoparticle network device. The nanoparticle network with fabricated source and drain electrodes rests on a silicon wafer capped by silicon dioxide. Current flow within the network is induced by externally biasing the drain against the grounded source by U_{ds}. A voltage on the back-gate, U_g, may be used to stimulate charge injection into the network. The voltage on the AFM tip, U_{tip}, is the sum of an *ac* modulation and a *dc* bias for performing KFM.

or dodecanethiol) and suspended into chloroform [108] for the self-assembly of a two-dimensional nanoparticle film on the liquid-air interface [109]. The film was subsequently transferred by micro-contact printing [110] using polydimethylsiloxane (PDMS) onto a silicon (Si) wafer piece covered by a 60 – 90 nm thin layer of thermally grown silicon dioxide (SiO_2). Electrical contacts were fabricated either by shadow-mask evaporation of gold on top of the printed network, or by pre-patterning the substrate with graphene electrodes [111].

Outline

We will first introduce a simple resistor model to understand the formation of terraces within nanoparticle networks. Then, we demonstrate their observation by KFM in different devices as a function of source–drain bias, and we also investigate transients after injection of charges.

We estimate by KFM the contact resistance for devices with graphene contacts, and we simulate current injection from graphene to the nanoparticle network. We then show how the potential landscape observed by KFM allows us to render current flow within the networks visible by a numerical reconstruction algorithm. We compare the potential landscape and reconstructed currents for networks before and after introducing conjugated molecules.

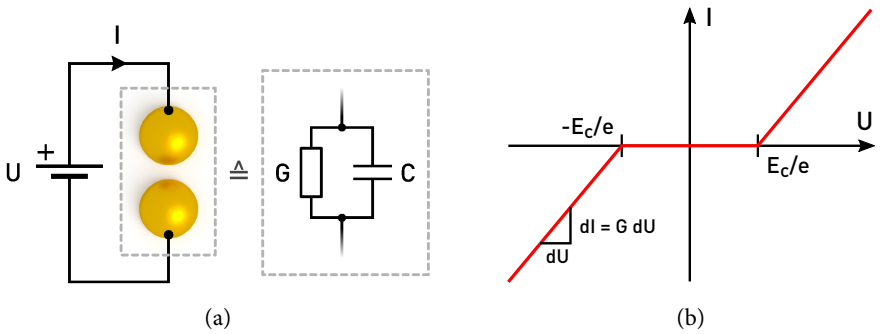

FIGURE 5.2: Schematic of Coulomb blockade in a system of two nanoparticles. (a) The equivalent circuit consists of a tunnel conductance G and the mutual capacitance C in parallel. (b) Expected current as a function of bias voltage, U. Current flow is inhibited for $|U| < E_c/e$, where E_c is the single-electron charging energy of the particle system.

Finally, we showcase particle-resolved surface potential and topography, and discuss future opportunities for KFM on nanoparticle network devices.

5.1 EVOLUTION OF POTENTIAL TERRACES IN RANDOM RESISTOR NETWORKS

Let us begin with a model for a single junction of two nanoparticles of radius r. The situation is illustrated in fig. 5.2a. The small vacuum gap between the particles presents an energy barrier determined by the work function. Only by quantum mechanical tunnelling can electrons at the Fermi level therefore overcome this barrier and travel from either particle to the other. With an applied bias voltage, U, between the particles, a net electron current will form that depends exponentially on separation, s, as $I \propto \exp(-2\kappa s)$, where κ is a decay constant and depends on the work function [3, 112]. For fixed separation and barrier height, we expect ohmic behaviour for the junction. Therefore we identify it by the resistance R or the conductance $G = 1/R$.

Until now we have neglected the effects of single-electron charging. The small size of the nanoparticles results in a small self-capacitance, $C = 4\pi\epsilon_0\epsilon_r r$, of ≈2.2 aF for 10 nm-diameter particles on SiO_2 ($\epsilon_r \approx 3.9$).[1] From the electrostatic energy of an isolated particle, $E = Q^2/2C$, we see that an energy of ≈40 meV is required to add a single electron.[2] In the general case of more than one particle, the change in total

1 $4\pi\epsilon_0 \approx 0.1113$ aF/nm
2 $e^2/2 \approx 80$ meV aF

electrostatic energy needs to be considered for every tunnelling event. Importantly, there is a contribution of the mutual capacitance between neighbouring particles, and the capacitance between each particle and its environment, e.g. a backgate electrode.[3] When the energy change due to a single-electron event, $E_c \approx e^2/2C$, becomes larger than the thermal energy $k_B T$, we expect no tunnelling at low bias. Only when the externally applied voltage exceeds a threshold, $U_t = E_c/e$, current flow is allowed and the linear current–voltage relationship with $dI/dU = G$ is established. This situation with suppressed current flow below a threshold is called *Coulomb blockade* (fig. 5.2b). Coulomb blockade and single-electron tunnelling can only be observed when the electrons are sufficiently confined to the particles. With the energy-time uncertainty principle, $\Delta E \Delta t \geq \hbar/2$, an energy uncertainty, $\Delta E \approx e^2/2C$, and the time scale of a tunnelling process, $\Delta t \approx RC = C/G$, we must demand $G \ll e^2/\hbar = \pi G_0$, where G_0 is the conductance quantum.

Two-dimensional nanoparticle networks consist of thousands of such tunnel junctions. Middleton & Wingreen [115] have modelled the collective transport in regular arrays and predicted the two-terminal current as $I \propto (U/U_t - 1)^\zeta$, where the threshold voltage U_t is a function of the linear system size, and ζ is the conductivity exponent that in general depends on dimensionality and the network.[4] Below U_t, electrons can propagate only through a fraction of the array, leading to a charge front moving with the applied voltage. Only after the charge front has reached the other electrode, the current-voltage relationship is linear again. Experimentally, the current–voltage relationship was confirmed at low temperatures in regular well-ordered arrays [104] and cellular networks [106]. The exponents ζ herein depend on the microscopic structure of the networks.

Disorder in the nanoparticle arrays was considered already in the early work by Middleton & Wingreen [115] as random parasitic charges localised in the substrate which induce offset charges $\in (0, e)$ on the nanoparticles (*quenched charge disorder*). Accordingly, these fractional charges locally shift the voltage threshold for tunnelling. *Structural disorder*, i.e. variations in the particle separation s, induces a wide distribution of interparticle conductances, G, because of the exponential dependence on s. As pointed out by Parthasarathy, Lin & Jaeger [104], a large variance in G is thus almost a certainty, even in well-assembled arrays.[5]

3 The capacitance between a sphere (radius r) and the backgate plane quickly approaches the self-capacitance of a sphere for large distances $d \gg r$. To our knowledge there is no closed-form expression for the mutual capacitance of two adjacent particles in a network. But we can estimate it by the capacitance between two spheres at separation s using an analytical expression by Lekner [113]. For $r = 5\,\text{nm}$ and $s = 2\,\text{nm}$, we find $C \approx 1.4\,\text{aF}$, where we assume $\epsilon_r = 2.7$ for an alkanethiol environment [114].

4 See Zabet-Khosousi & Dhirani [102] and Suvakov & Tadić [116] for reviews on charge transport in nanoparticle assemblies.

5 Normally distributed size and separation of adjacent nanoparticles causes a log-normal distribution of conductances in tunnel junctions. Further irregular structural disorder effectively disconnects particles.

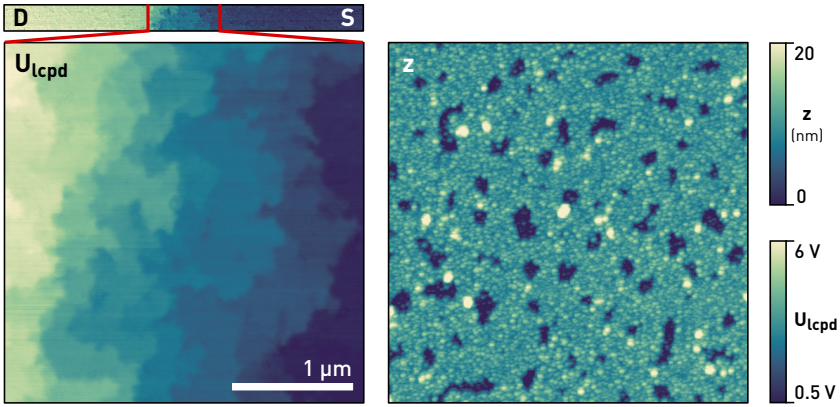

FIGURE 5.3: Surface potential and topography of a nanoparticle network device at $U_{ds} = 7.5$ V. Within the 15 µm long channel between the electrodes, indicated above, the main potential drop is in the middle. The potential drop exhibits characteristic terraces which we explain by disorder.

At temperatures above zero, there is always a finite probability for an electron to overcome the tunnelling threshold. Furthermore, it has been observed that the threshold voltage in an array decreases with temperature, since in case of quenched charge disorder more and more junctions can overcome their thresholds due to thermal fluctuations alone [117, 118].

At room temperature, experiments with $2r \approx 10$ nm nanoparticles show for these reasons mostly ohmic behaviour under all bias conditions [105]. While the Coulomb blockade is lifted, conductance due to tunnelling is still extremely sensitive to distance and environment.

In fig. 5.3 we show a FM-KFM scan of a 10 nm-nanoparticle network device, measured in air at room temperature. An intriguing feature is the terrace-like potential drop along the channel. We see in the topography that this network has many holes on large scale, and we also expect disorder on a microscopic level.

To understand the formation of terraces in such devices, we introduce the simplified model of a resistor network in which ohmic resistors connect adjacent nodes. Writing Kirchhoff's current law for each node i in the network graph leads to

$$-I_i^{\text{in}} = \sum_{j,i\neq j} I_{i\to j} = \sum_{j,i\neq j} G_{ij}(U_j - U_i) = \sum_{j,i\neq j} G_{ij}U_j - U_i \sum_{j,i\neq j} G_{ij}, \qquad (5.1)$$

where the sum is over all adjacent nodes j, $G_{ij} = G_{ji}$ is the conductance facilitating their connection, U_j is the node potential, and I_i^{in} is an additional net current

flowing into node i. We assume that the currents in the system originate only from electrodes, i.e. nodes that are fixed in their potential, such that $I_i^{\text{in}} = 0$ for all non-electrode nodes in the system. Treating electrode nodes separately with an index ν, we obtain a linear system of equations for the node potentials and the net incident electrode currents:

$$\sum_{j,i\neq j} G_{ij}U_j - U_i\left(\sum_{j,i\neq j} G_{ij} + \sum_{\nu} G_{i\nu}\right) = -\sum_{\nu} G_{i\nu}U_\nu \tag{5.2}$$

$$\sum_{i} G_{\nu i}U_i + I_\nu^{\text{in}} = U_\nu \sum_{i} G_{\nu i} \tag{5.3}$$

For a system of linear independent equations, one electrode needs to be *grounded* and therefore removed from the system of equations. Knowing all involved conductances and electrode potentials, this system can be solved for the node potentials and incident electrode currents.

In order to model a realistic nanoparticle network, we consider a hexagonally close packing, with nodes forming an equilateral triangular lattice. Each node i is connected to its neighbours j via the conductance G_{ij}.[6] This situation is illustrated in fig. 5.4a. We introduce disorder into the system by choosing G_{ij} for adjacent nodes randomly to be be either conducting, G_{h}, with a probability p, or poorly conducting, G_{l}, with a probability $1-p$. This is motivated by the exponential dependence of the tunnelling conductance on distance—conduction in junctions with only a slightly larger separation is exponentially suppressed. Therefore, G_{h} is a typical interparticle conductance, whereas G_{l} controls the leakage current which is likely to be present in any sample measured at room temperature under ambient conditions.[7] The outer nodes, spanning a rectangular area on either side of the lattice, are connected to source and drain electrodes, respectively, via the conductance $G_{i\nu}$.

For conductances randomised with $p = 0.38$ ($G_{\text{h}} = 1\,\text{S}$, $G_{\text{l}} = 1\times10^{-10}\,\text{S}$, $G_{i\nu} = 0.1\,\text{S}$) and a hexagonal lattice of 100×100 nodes, we show the simulated node voltages U_i and edge currents $|I_{ij}|$ in fig. 5.4b. Nodes are mapped to a greyscale from black (source) to white (drain potential) according to their voltage. Currents are drawn as red lines connecting adjacent nodes, whereas $|I_{ij}|$ determines their thickness. Likewise, we encircle nodes connected to the source or drain electrode in red as a function of current injected or sourced from a nearby electrode.[8]

6 G_{ij} is zero for non-adjacent nodes i and j. It can be seen as a weighted adjacency matrix of the network graph.

7 In the limit of $G_{\text{l}} \to 0$, the randomisation of conductances could produce nodes with no conducting path to an electrode, whose potential is undefined by the system in eqs. (5.2) and (5.3). At nonzero G_{l}, there are no such floating nodes.

8 Creation of model networks of arbitrary shape and size, calculation of node potentials using eqs. (5.2) and (5.3), as well as their visualisation, is implemented in Python using graph-tool [119] and SciPy [120].

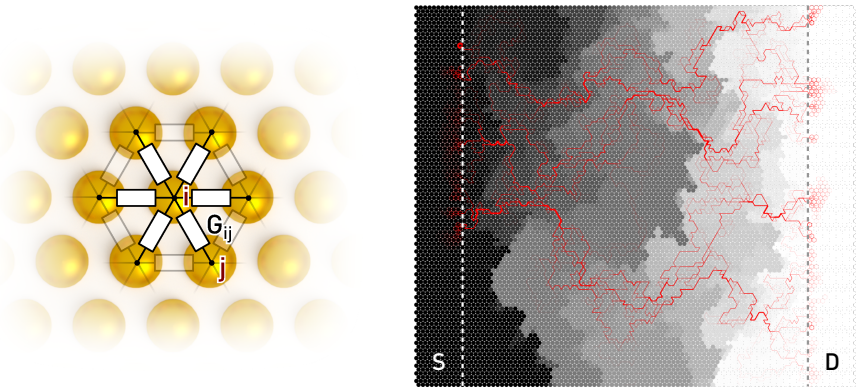

(a) (b)

FIGURE 5.4: (a) Schematic of interlinked nanoparticles forming a two-dimensional network of resistors. The neighbouring particles i and j are linked by the conductance G_{ij}. (b) Calculated node potential and currents visualised in a hexagonal network of 100×100 particles with randomised conductances ($p = 0.38$). Electrode boundaries are indicated by the dashed lines.

Qualitatively, we observe a terrace-like drop of the potential from drain to source. The main current through this network is carried by only a few dominant pathways. Many junctions are passive and could be removed without large influence on the total current through the device. This simple network of random resistors reproduces the terraces observed in the KFM measurement of the real biased nanoparticle array, fig. 5.3.

Why is this the case? As it turns out, by randomising resistances in the network, we have tacitly turned our problem into one of *percolation theory*—dealing with diverse topics such as the spread of forest fires, gelation, or oil fields. More specifically, percolation theory describes the formation of clusters in randomly occupied, multidimensional lattices. Let us neglect all low conductances in the network. Let us also neglect electrodes and currents. Instead, in the language of percolation, we now call edges in our network graph *bonds*, and nodes *sites*. A bond is *occupied* when it is conducting, or *empty* otherwise.[9] A *cluster* is the set of sites in which each member is connected to another member by at least a single occupied bond.[10]

9 See Stauffer & Aharony [121] for an excellent introduction to many aspects of percolation theory.

10 Here we describe *bond percolation* on a graph. Similarly, there is *site percolation* when instead of bonds we occupy sites and consider them connected if a neighbouring site in the lattice is also occupied.

As we increase the relative number p of occupied bonds in a lattice, starting from zero, an increasing number of clusters is formed and fused together. When we cross the percolation threshold, p_c, the system undergoes a phase transition and there is at least one *spanning* or *infinite* cluster, i.e. one connecting one edge and its opposing edge of the lattice. p_c is only well-defined in a lattice of infinite size, because for finite size there is a nonzero chance that a spanning cluster is found for $p < p_c$ but also a nonzero chance not to find one for $p > p_c$.

Near the phase transition at p_c, certain observables go to zero or approach infinity by simple power laws with *critical exponents*. These exponents are universal in the sense that they *only* depend on dimension but not the chosen lattice [121]. For example, the fractal dimension d_f relates the number of sites, or *mass* M, of the spanning cluster within a radius L as $M \propto L^{d_f}$.[11] Another exponent, ν, describes the divergence of the *correlation length*, ξ, the *rms* average distance of two sites belonging to the same cluster [121]. Near p_c, ξ diverges as $\xi \propto |p - p_c|^{-\nu}$.

Random resistor networks have been studied extensively in the framework of percolation. In a seminal paper, Last & Thouless [124] studied the conductivity of a sheet of colloidal graphite paper as they punched an increasing amount of holes into it. They could show that as p_c is reached from above, the conductivity is *not* simply proportional to the mass of the spanning cluster, as was suspected before.

In fig. 5.5 we show a similar but numerical experiment for our hexagonal lattice. The current between drain and source is proportional to the conductance. At $p = 1$ the resistor network is not random and reaches its maximum conductance. By lowering p, the current first decreases linearly. Near the percolation threshold at $p_c \approx 0.35$, the current slowly approaches zero (governed by yet another critical exponent [125]). Below p_c current flow comes to a halt since the network is lacking a spanning cluster.

The insets in fig. 5.5 show the node potentials and dominant current paths for different p. Close to the percolation threshold at $p = 0.35$, there is only a single percolating path through the network. With increasing p, the number of paths and therefore the current increases. The terrace-like potential landscape that is prominent near the percolation threshold is smoothed as more well-conducting current paths become available.

In case of an infinite hexagonal lattice and bond percolation, the exact value for p_c is $2\sin(\pi/18) \approx 0.347$ [126]. We see from fig. 5.5 that for finite but nonzero G_l and lattice size, there is a phase transition near the percolation threshold above which the current increases linearly with p, since there is an increasing amount of well conducting paths for the current.

11 *Fractals* are self-similar structures at every scale. They are ubiquitous in nature and display a fractional Hausdorff dimension [122]; for example, the length of a coastline depends on the scale of measurement [123].

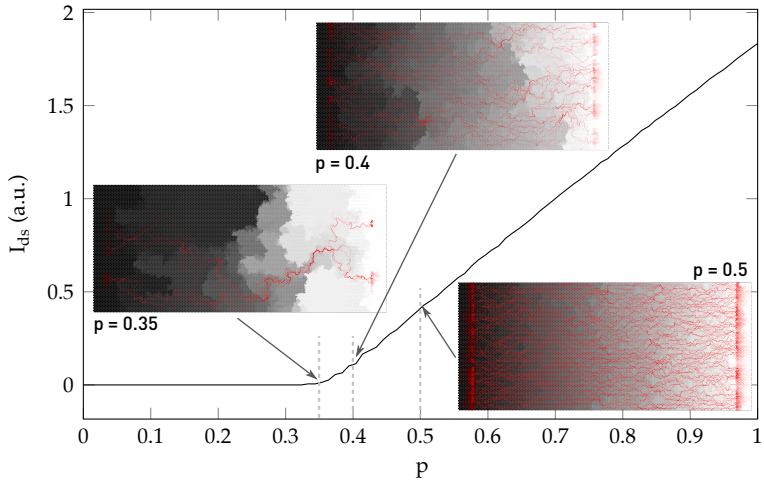

FIGURE 5.5: Source-drain current through a hexagonal network of 200×100 particles at a varying fraction of good connections, p. The insets show the node potentials with superimposed dominant current paths.

Well above p_c in the linear regime of I_{ds} vs. p, conduction in a random resistor network can be explained by an *effective medium theory* [127], in which each resistor in the network is replaced by an effective conductance as a function of p.

If it is not the mass of the spanning cluster near p_c, what else determines the conductance? Many bonds in this cluster will carry no current, since they are dangling, or dead ends. These dangling bonds can thus be removed from the cluster without influencing the total current. At p_c, most of the cluster mass consists of such dead ends.

We can illustrate conduction as the random walk of electrons starting their journey at the source electrode and trying to find a path to the drain. Electrons travelling into dead ends need to return by the same path as they entered—thus there is no net current into dead ends. After removing them from the spanning cluster, we arrive at the *backbone* for current flow.

The analogy from conduction to random walks is already contained in Kirchhoff's current law. We see from eq. (5.1) that an electron at internal nodes i, without external current, is at the potential U_i,

$$U_i = \frac{\sum_{j,i\neq j} G_{ij} U_j}{\sum_{j,i\neq j} G_{ij}} = \sum_{j,i\neq j} \left(\frac{G_{ij}}{\sum_{k,i\neq k} G_{ik}} \right) U_j = \sum_{j,i\neq j} p_{ij} U_j, \tag{5.4}$$

where we have introduced $p_{ij} \equiv G_{ij} / \sum_{k,i\neq k} G_{ik}$, the probability to move from node i to j. The conductance G_{ij} gives the rate of choosing the path $i \to j$, and for a probability we have to normalise by the total rate from i to all neighbours. We see from eq. (5.4) that node voltages in the network are a weighted average over their neighbour node potentials. It can be shown that the node potential U_i, normalised by the applied voltage, corresponds to the probability for an electron starting at i to reach the positive rather than the negative electrode in a random walk [128, 129].

This new view on the node potentials motivates the origin of a terrace-like potential landscape. All dead ends in the spanning cluster acquire the potential of their only source node. At the percolation threshold we have a spanning cluster but only a single shortest path through the network, avoiding dead ends. Most nodes within the cluster thus lighten up as terraces.

Terraces are hence the result of the weak and fractal nature of the spanning cluster. Removal of only few bonds can already break it into pieces. This led to the picture of a nodes–links-blobs model for its structure [121, 130, 131]. In a finite-size problem above p_c, we can split the spanning cluster of length L into boxes of size ξ, the correlation length. Each box then contains often only a single chain of bonds connecting opposite edges (*links*), but sometimes there are multiple connecting chains (*blobs*).

The correlation length ξ thus determines the terrace size. Since ξ diverges with an exponent ν, terraces grow exponentially as p approaches p_c from above. At length scales well above ξ, microscopic details such as the lattice type become irrelevant.

With experimentally observed potential terraces, we can estimate the correlation length for our device. For a device length L much larger than ξ, the network appears homogeneous, and it can be described within an effective medium theory. But as device dimensions continue to shrink, the structure of the network and its spanning cluster becomes important. Electrons then meander through the network along fractal pathways.[12]

Percolation and properties of random resistor networks were studied extensively since the advent of cheap programmable computers in the 1980s. There was an intense effort to determine critical exponents numerically, or to verify and falsify predictions. Resistor models with exponentially-wide distributed [134] or zero-bias suppressed conductors [135] have been studied; resistors breaking upon overcurrent were modelled in random fuse networks [136]. More recently, random resistor networks were also used to explain the minimal conductivity in graphene at the Dirac point [137].

12 In two dimensions, the minimum path $d_{\min}$ is fractal with a dimension of ≈1.13 [132, 133].

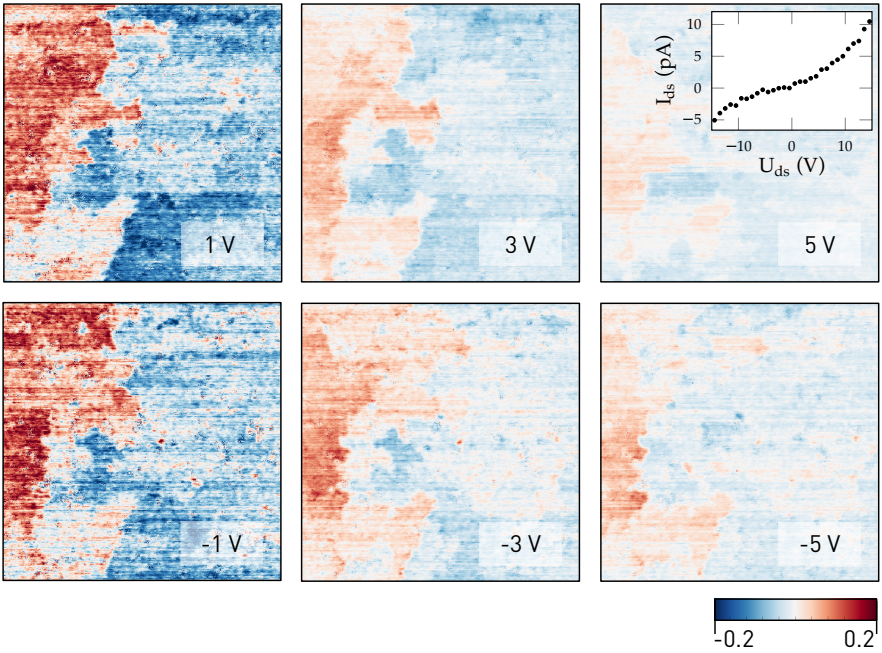

FIGURE 5.6: Differences between the normalised U_{lcpd} at a given U_{ds} and the normalised U_{lcpd} at $U_{\mathrm{ds}} = 7\,\mathrm{V}$. The inset shows an I_{ds}-U_{ds} curve obtained after the KFM measurements. All scans show the same area as in fig. 5.3.

5.2 SOURCE-DRAIN POTENTIAL MAPS AT DIFFERENT DEVICE BIASES

With a basic understanding of the formation of terraces, we now look back onto the network device shown in fig. 5.3 and study its dependence on the applied source-drain voltage, U_{ds}. For ohmic resistors bridging the network, of course, a normalised surface potential defined as $(U_{\mathrm{lcpd}}(U_{\mathrm{ds}}) - U_{\mathrm{lcpd}}(0\,\mathrm{V}))/U_{\mathrm{ds}}$ should be independent of the applied voltage. We show in fig. 5.6 differences between the normalised surface potential at U_{ds} and $U_{\mathrm{ds}}^0 = 7.5\,\mathrm{V}$ for $U_{\mathrm{ds}} = \pm 1\,\mathrm{V}$, $\pm 3\,\mathrm{V}$, and $\pm 5\,\mathrm{V}$.

Although the overall shape of terraces is unchanged, some of them move to higher or lower levels as $|U_{\mathrm{ds}}|$ is reduced. At $|U_{\mathrm{ds}}| = 1\,\mathrm{V}$ we find an increased potential drop between a region with terraces on the left, and another region on the right side of the device. The increased voltage drop at low $|U_{\mathrm{ds}}|$ hints at a reduced differential conductance between the two rather well-connected clusters on the left and right. Within these big clusters, the bias dependence appears to be much weaker.

In accordance with the observation of bias-dependent terraces, we find a zero-bias suppressed current–voltage relationship in the macroscopic $I_{ds} - U_{ds}$ measurement taken after performing the KFM investigations (inset of fig. 5.6). We think that strong structural disorder in this network has reduced the coupling between adjacent nanoparticles, revealing signs of a temperature-broadened Coulomb blockade. However we could not observe moving charge fronts as predicted by Middleton & Wingreen [115] for regular arrays, since the blockade is well-localised in our disordered device. In contrast, we have experienced purely ohmic behaviour for well-ordered 10 nm-nanoparticle arrays at room temperature.

5.3 MAPPING OF LOCAL CHARGE ACCUMULATION AND DEPLETION TIMES

KFM not only allows for spatial and potential resolution, but also for temporal resolution. U_{lcpd} can change over time e.g. upon adsorption of molecules, since these may form an additional dipole layer on the surface. U_{lcpd} also changes whenever localised charges redistribute, or when electrode voltages are subject to changes.

Time-resolved measurements of the surface potential are thus a powerful tool to investigate carrier dynamics. In traditional KFM setups, time resolution depends on the bandwidths for lock-in detection and the control system, with typical time constants on the order of 1 – 10 ms. Pump-probe techniques are capable of resolving changes even on a nanosecond time scale [138]. To this end, the system is repeatedly and coherently pumped by an electrical or optical pulse, and the time-averaged response within a probe window is tracked by the KFM feedback. Not employing a nulling feedback loop, electrostatic force microscopy (EFM) techniques are also capable of resolving time constants down to a temporal resolution of ≈100 ns [139, 140]; however, the detected signal is potentially a mix of changes in surface potential and tip–surface capacitance.

Here we are interested in charging dynamics of nanoparticle networks. In preliminary experiments we have observed transients in the measured surface potential after a change of the backgate voltage, U_g. Figure 5.7a shows U_{lcpd} vs. time after setting U_g to 1, 0, 2, and 0 V with the AFM tip resting in the middle of the device shown in fig. 5.3, at $U_{ds} = 0$. For constant gate potential, the surface potential is constant over time. Immediately after changing U_g, however, U_{lcpd} changes by $\approx \Delta U_g$, and then exponentially approaches a terminal value. For this device, time constants τ are on the order of seconds.

We can understand the underlying process as follows. The nanoparticle network and the backgate electrode form a capacitor, $C_g = \epsilon_0 \epsilon_r A / d_{ox}$. Nanoparticles underneath the AFM tip are connected to the grounded electrodes via an effective current path with the resistance R. There are equal but opposite charges on the capacitor

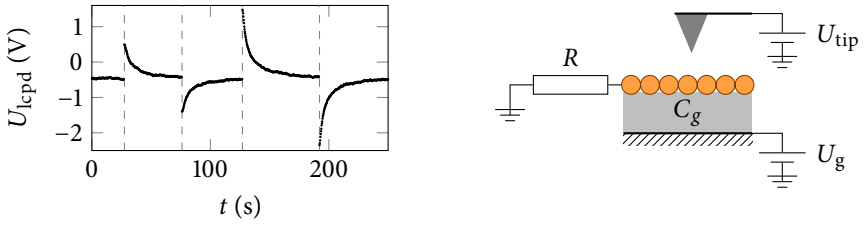

(a) (b)

FIGURE 5.7: (a) Transients in the surface potential after changing U_{g} from 0 V to 1 V, 0 V, 2 V, and back to 0 V. (b) Equivalent circuit diagram.

plates. A change in U_{g} causes a charge flow into the network until a steady state is reached. From this understanding of the system, sketched in fig. 5.7b, we expect the surface potential to change as $\Delta U_{\mathrm{lcpd}} = \Delta U_{\mathrm{g}} \exp(-t/\tau)$, where $\tau = RC$ is the time constant. It thus takes time for carriers in the film to accumulate and thereby screen the backgate potential.[13]

We can roughly estimate C_{g} and R for the orders of magnitude. The capacitance from film geometry is $C_{\mathrm{g}} \approx 1 \times 10^{-13}$ F. The total film resistance at low bias is $R \approx 10\,\mathrm{T\Omega}$, thus we expect $\tau \approx 1\,\mathrm{s}$ if there was only one path through the network, or proportionally more with an increasing number of parallel paths. However, the gate oxide is likely to be imperfect, with many defects and localised trap states within the oxide bandgap. These provide additional sites for tunnelling or thermally driven hopping [141]. The population of traps is also a slow process, thus care has to be taken to exclude their influence.

Keeping the geometry unchanged, the time constants obtained should change with the type of majority carrier and the differential resistance $\mathrm{d}U/\mathrm{d}I$ at U_{ds} for a single current path. If electrodes on both sides of the network are kept at ground, we expect the largest time constants in the centre.

In fig. 5.8a we show topography and surface potential of a different nanoparticle network. As seen in the topography, the network appears more disordered and sparse in the centre region, and there are two holes in the upper region of the scan. These defects in the network were probably caused by incomplete transfer from the stamp in micro-contact printing. The surface potential again exhibits terraces. In

13 The transient behaviour can deviate from a purely exponential decay in real systems or more sophisticated models. The real network is rather a transmission line formed by the conductances and mutual capacitances of adjacent nanoparticles, and the capacitances of each nanoparticle to the backgate electrode. However, given the number of unknowns in a disordered network, major additional insights are not expected at this point.

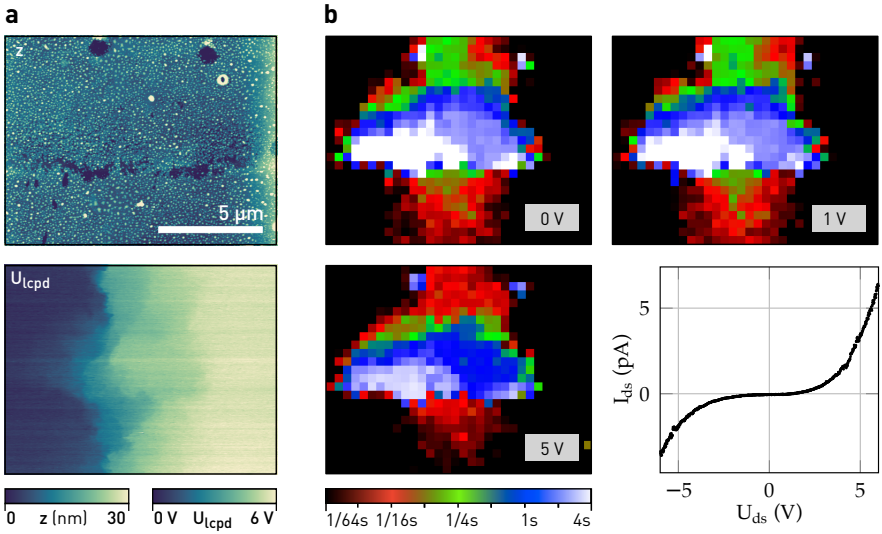

FIGURE 5.8: (a) Topography and surface potential at $U_{ds} = 5\,V$. (b) Maps of time constants at different U_{ds}, extracted from fits of the local transient behaviour. Due to the non-linear I_{ds}-U_{ds} characteristic of this device, the local charge accumulation and depletion times change with applied bias.

fig. 5.8b we show maps of time constants at different U_{ds}. These were obtained on a grid of 32×32, where for each pixel the backgate was driven by a 0.2 Hz square wave with an amplitude of 2 V for 2.5 periods. The time constants are averages of exponential decays fitted to the data.

The top two maps of τ at $U_{ds} = 0\,V$ and 1 V both look similar. In the array's sparse centre region, the time constants of >1 s are considerably larger than elsewhere in the film. Regions where backgate oxide is exposed display the longest decays, hinting at population of traps and thus charge accumulation in SiO_2 near the surface. Regions with better quality of the nanoparticle film show time constants of 1/4 s or less. Charge accumulation and depletion is consistently faster near the electrodes, as expected. Again, this device exhibited a strong suppression of current flow for low bias. The map of τ for U_{ds} above the threshold shows reduced time constants in all parts of the network. For example, the upper network region changed by a factor of four from $\tau \approx 1/4$ s to $\approx 1/16$ s, indicating a fourfold increase in conductance.

With better film quality, time constants are further expected to decrease, and due to the limited Kelvin feedback bandwidth the mapping as shown here becomes too slow. A viable alternative is the pump-probe technique mentioned above, allowing

one to take snapshots of the surface potential as a voltage pulse propagates through the network.

5.4 CONTACT RESISTANCE IN DEVICES WITH GRAPHENE ELECTRODES

A recurring problem with the fabrication of nanoparticle devices is facilitating stable electrical contacts with low resistance to the network. In the devices shown before, these were added after deposition of the network via a shadow mask. Such contacts often are more than 50 nm in height to ensure continuous contact and enable wire bonding. As we have shown in [111], single-layer graphene (SLG) makes coplanar bottom contacts to nanoparticle networks possible. To this end, we transferred graphene obtained by chemical vapour deposition onto a Si wafer capped with 90 nm SiO_2. By standard optical lithography, graphene was patterned into electrode structures, and pads suitable for wire bonding were added by e-beam evaporation of 5 nm titanium and 60 nm gold. The nanoparticle networks are subsequently printed onto the prepatterned substrate. With contacts only one atom thick, the nanoparticle network is not broken at the electrode interface. Since the network is added only in the last step of device fabrication, it is never covered by resist and stays chemically pristine. The contacts also allow for high-resolution scanning probe microscopy, because unlike with metal top contacts there are no steep edges at electrode boundaries.

We have characterised such contacts by the transmission line method (TLM), in which contact resistance is inferred from macroscopic measurements of the two-terminal resistance with different channel length [142]. We have further measured the contact transfer length using scanning probe lithography, by repeatedly cutting the network on top of an electrode and thereby reducing the effective contact length and area [111].

In fig. 5.9 we show an optical micrograph as well as topography and surface potential of a nanoparticle device with graphene electrodes. Compared to previous nanoparticle devices shown in this thesis, this device showed only the expected ohmic behaviour at room temperature, owing to better film quality.

The device exhibits two large outer electrodes used as source and drain, and two inner electrodes that are shorted with a graphene bypass (see fig. 5.9a). An equivalent circuit diagram is overlaid in fig. 5.9b. R_C is the contact resistance from network to graphene, R_N is the resistance of a unit length of the nanoparticle array, and R_G is the resistance of the graphene bypass. The middle region, bypassed by the graphene shortcut, is roughly four times the channel length of 1.5 µm. Between the network on top of the bypass, the potential difference $U_2 - U_1 \equiv \Delta U$ should be close to zero for a

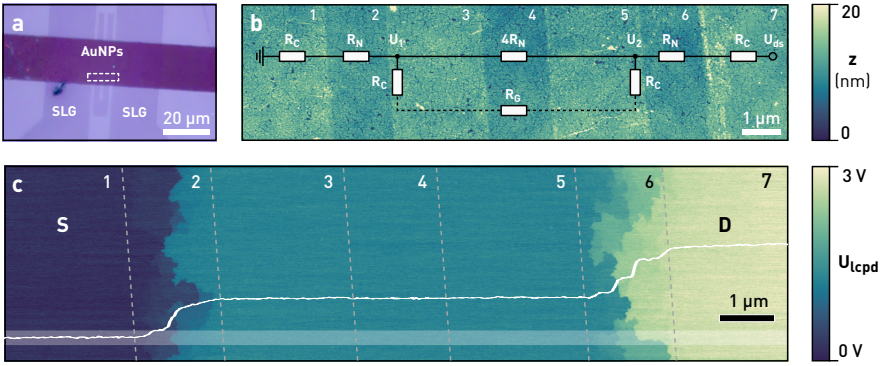

FIGURE 5.9: (a) Optical micrograph of a nanoparticle device with a graphene bypass electrode. (b) Topography and (c) FM-KFM image of the region indicated in (a). The graphene bypass remains floating during the measurement. The equivalent circuit diagram is overlaid in (b). The potential profile, averaged across the shaded rectangle, is superimposed in (c).

contact resistance negligible compared to the network resistance. With $\alpha = R_C/R_N$ and assuming $R_G \ll R_C$, we find

$$\frac{\Delta U}{U_{ds}} = \frac{\alpha}{1 + (\alpha^2 + 5\alpha)/2} = \alpha + \mathcal{O}(\alpha^2). \tag{5.5}$$

The measured U_{lcpd} at $U_{ds} = 2.5\,V$ shown in fig. 5.9c exhibits terrace-like potential drops in areas 2 and 6, but no drop in-between the bypassed region. With the *rms* noise level of ≈60 mV in this measurement, we arrive at an upper bound of $R_C/R_N \approx 1/50$.

The applied voltage splits roughly symmetrically between the left and right area with 1.1 V and 1.4 V, respectively. Thus, the nanoparticle array seems to be of similar conductivity in both areas, even though their terrace sizes indicate conduction near the percolation threshold.

In fig. 5.10, we display topography and surface potential of a different area within the right gap of the device (area 6 in fig. 5.9c). The terraces appear crisp and well-defined with many small dents and protrusions. We can determine an estimate of the correlation length from a line-by-line analysis of the potential drop within the network. To this end, we separate terraces within a scan line by a chosen threshold and assign each terrace the average *rms* distance of two member pixels.[14] These distances, averaged over all lines and terraces, provide an approximate cluster radius

14 For a terrace of length L, the average *rms* distance l_{rms} of two points taken from a uniform distribution is $l_{rms}^2 = L^2 \int_0^1 dx \int_0^1 dy (x-y)^2 = L^2/6 \approx (0.4L)^2$.

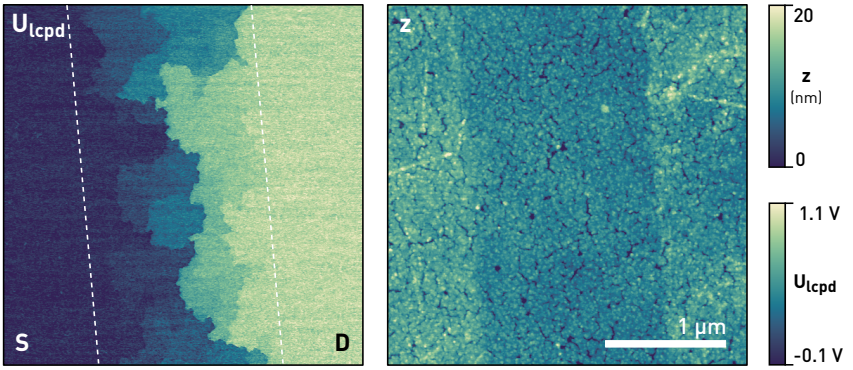

FIGURE 5.10: Surface potential and topography within the right gap of the device shown in fig. 5.9.

or linear extent $\tilde{\xi}$. For fig. 5.10 we find $\tilde{\xi} = 190 \pm 70$ nm, where the error is the standard deviation of extracted terrace radiuses. The error hereby reflects the spread in terrace size, not a measurement imprecision.

To establish reliable electrical contacts to disordered nanoparticle networks, one should aim for contact lengths larger than $\tilde{\xi}$. Thereby, current injection is spread over several terraces. Current injection into the network further depends on the contact transfer length as a figure of merit. Taking into account the upper bound of R_C/R_N found above and by monitoring the increase in resistance after cuts in scanning probe lithography, we estimate transfer lengths L_T between 200 nm and 400 nm for our devices [111]. L_T is related to the contact resistivity, ρ_c, and sheet resistance, R_s, by $L_T = \sqrt{\rho_c/R_s}$. From the transmission line model, the contact resistance R_c is expected to be $R_c = R_0 \coth(d/L_T)$, where $R_0 = R_s L_T/W$ is the minimum attainable contact resistance for long contact lengths d and widths W.

Both ρ_c and R_s can be expressed in terms of an equivalent resistor network as introduced before. In a lattice, in which adjacent particles are connected by resistances R_{pp}, and particles in contact with graphene electrode are connected by R_{pg}, the transfer length can be expressed as $L_T = \alpha d_{pp}\sqrt{R_{pg}/R_{pp}}$, where α is a scaling factor due to the choice of lattice.[15] The distance between adjacent nanoparticles, d_{pp}, was determined by SEM to be ≈14 nm. For a hexagonal lattice, we find R_{pg}/R_{pp} of 160

15 Network resistance and the bond-forming resistors are related by $R_N = \gamma R_{pp} L/W$ for large lengths L and widths W, thus $R_s = \gamma R_{pp}$. For the contact resistivity ρ_c, we assume that each particle occupies a hexagonal unit cell given by the particle–particle distance d_{pp} and is connected to graphene by R_{pg}. Therefore, $\rho_c = R_{pg}\sqrt{3}d_{pp}^2/2$, and using the expression of the transfer length, $\alpha^2 = \sqrt{3}/2\gamma$. In hexagonal lattice, $\gamma = 1/\sqrt{3}$ due to symmetry; hence, $\alpha = \sqrt{3/2}$.

and 630 corresponding to transfer lengths of 200 nm and 400 nm, respectively. This resistance ratio needs to be treated as an effective value for disordered real networks.

By solving Kirchhoff's current law on each node in a model network, eqs. (5.2) and (5.3), we can simulate current injection into disordered networks by randomly assigning low resistances R_{pp} with a probability p, or high R_{pp} with a probability $1 - p$. A simulation as such thus resembles a two-dimensional discrete transmission line model including structural disorder. The current injected from each modelled particle is mapped in fig. 5.11 for both choices of transfer length and a well-ordered ($p = 1$) and disordered ($p = 0.4$) network.

In a well-ordered network, the injected current vanishes exponentially with distance from the electrode edge. This is not the case with disordered networks. Current injection there is limited by locally well-connected clusters of particles on the order of the correlation length. To achieve the same transfer lengths as in the well-connected case, R_{pg}/R_{pp} can reach 2000 and 10800 for $p = 0.4$ and transfer lengths of 200 nm and 400 nm, respectively, assuming constant R_{pg} for all nanoparticles connected to electrodes. Although the distribution of resistances is expected to be more complicated in real networks, this simple binary percolation model shows qualitatively how structural disorder affects current injection.

5.5 CURRENT PATHS IN DEVICES BEFORE AND AFTER MOLECULAR EXCHANGE

In the previous measurements we have attributed the variation in interparticle conductances mostly to structural disorder. Now we consider the case of a fixed structure, with inherent disorder, after modulating the conductance of a number of junctions.

Arrays made of gold nanoparticles are a suitable test bed for molecular electronics. After assembly and deposition on a substrate, molecules of interest can be brought into the array by a molecular exchange process [103, 105, 143, 144]. To this end, the device is immersed in solvent (e.g. ethanol or tetrahydrofuran, THF) with excess thiolated molecules. During immersion, it is assumed that the molecules penetrate the alkanethiol ligand shell around the nanoparticle and attach to gold via their thiol endgroup. At the same time, bound ligands can detach and leave into the solvent. After some time (few hours at room temperature) the reaction reaches an equilibrium after which the surface coverage does not change anymore. It is also assumed that the geometry does not vary during the exchange process.[16]

16 In control experiments without addition of thiolated molecules to the solvent, we could still observe increased conductance. At this stage, we cannot exclude at least a partial influence of the solvent in the experiments reported here. Details will be reported by Patrick Reissner *et al.*

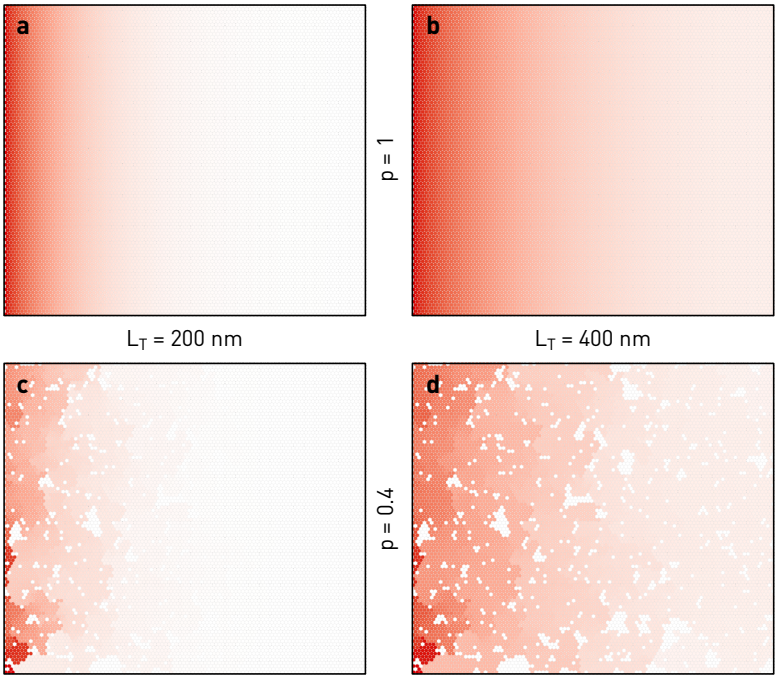

FIGURE 5.11: Simulation of current injection from a graphene electrode held at constant potential into a nanoparticle network on top. In each case, the electrode edge is on the left side. The red colour shade visualises the normalised current injected per particle. In (a) and (b), the simulation is shown for a perfect hexagonal network for different transfer lengths L_T. For the same transfer lengths, the simulation is shown in (c) and (d) for a network close to the bond percolation threshold of a hexagonal lattice, with only 40 % of the particles being well connected ($p = 0.4$).

After such treatment of a nanoparticle device we expect changes of the interparticle conductances G_{ij}. Since the voltage drop per junction is on the order of only 10 mV in devices with 100 particles in series at 1 V, and thus well below a typical HOMO–LUMO gap of ≈1 eV, transport is typically still in the tunnelling regime. One mechanism for increased conductance after exchange is the lowering of tunnel barriers. If conjugated molecules are added, their delocalised π orbitals can act as sites for hopping conduction [145]. An electron sitting on one nanoparticle thus is presented with alternative ways for moving to neighbour nanoparticles via multiple tunnelling processes of shorter distance. Highest conductance is expected when a conjugated dithiolated molecule interlinks two nanoparticles via covalent sulfur–gold bonds, therefore acting as a molecular wire [146]. However, this requires particle separations matching more or less accurately the length of the inserted molecule as well as the binding of the two thiol moieties. For this reason, mono-thiolated terphenylthiol (TPT) was chosen in our study.

Kelvin probe force microscopy provides the unique chance to look into the potential landscape of nanoparticle networks, and to observe local changes after molecular exchange. Optical methods to study local behaviour, for example scanning photocurrent microscopy [147], remain limited by diffraction. Scanning probe techniques based on local current measurement through the tip (STM, conductive AFM) would disturb the potential landscape in biased devices. In contrast, the nulling process in KFM ensures no *dc* current flow, and thereby minimises coupling from tip to surface. High-resolution AFM and KFM may furthermore help understanding the molecular exchange process itself, by independently probing the topographic stability of the arrays and electronic effects before and after the exchange.

Reconstruction of current paths

Images of a potential landscape are not straightforward to interpret in terms of current flow through the network. We have seen before how one can find the potential in networks of arbitrary resistors and voltage sources. In this case, the current through each resistor is given by Ohm's law, $I_{i\to j} = G_{ij}(U_j - U_i)$.

Without detailed knowledge of every resistor in the network, the potential drop observed by KFM thus provides only part of the solution. In the one-dimensional case, as in nanowires (see chapter 4), the current through a chain of resistors must be constant and equal to the current driven through the terminals of the device. Hence, large potential drops correspond to large resistances.

In two dimensions, the situation is more delicate. There are many configurations of resistors that result in the same observed potential drops for a fixed current driven

through the network.[17] Without further information about the network, we have to rely on a method that selects one distribution of resistances out of many.

As discussed, the size of terraces in a random resistor network is related to a correlation length. They appear flat because the nodes within are well-connected. We are rather interested in how current flows from terrace to terrace. Therefore, instead of modelling the microscopic structure of the nanoparticle network, we only consider a *model network* in which nodes are placed at equal distances below the average terrace size.

For this model network, we now find a realisation of resistors that is able to match the measured potential drop. Knowing the voltages on all nodes and the current into the electrodes, the linear system of equations in eqs. (5.2) and (5.3) can be formally rewritten as $\mathbf{A}g = -I^{\text{in}}$, where g is the conductance vector with components $g_k = G_{ij} = G_{ji}$ for each edge k connecting the nodes i and j, and $\mathbf{A}$ is a coefficient matrix determined by node voltage differences and the network topology. As mentioned above, this system of N_{nodes} equations for N_{edges} unknowns is underdetermined in most non-trivial cases. Out of all possible realisations, it is possible to find a least-squares set of non-negative conductances:

$$\text{minimise} \quad (\mathbf{A}g + I^{\text{in}})^2 \tag{5.6}$$

$$\text{subject to} \quad g_k \geq 0 \quad \forall k \tag{5.7}$$

We perform this optimisation using CVXOPT [148]. Note that there are no distributions or conditions imposed on the g_k other than positivity, eq. (5.7). Based on the found conductances, we calculate node potentials and current flow between nodes in the model network as described in section 5.1.

While in general finding the *true* underlying distribution of resistors is impossible, we can justify and interpret the least-squares approach physically. Due to eq. (5.6), current flow in the network is minimised, and thus we expect to find a realisation of the observed potential drop using a minimum number of conductive links.[18] Starting from an empty network, resistive connections are added in order to match the observed potential drops between the nodes. When no potential drop is observed, no resistors are added. We thereby arrive at a realisation of the conduction backbone, similar to the backbone discussed for random resistor networks (see section 5.1). As more junctions become conducting, also the number of junctions in the backbone

17 Consider for example a square lattice of equal resistors in which current flows from one side to the opposing side, and thus the potential falls smoothly in-between. Half of the resistors carry no current at all since they feel no difference in potential. After removing all of these, the lattice is turned into parallel lines of resistors—keeping all potentials unaltered.

18 To illustrate the reconstruction, we use a simplified picture of either conducting or insulating links. The least squares method in eqs. (5.6) and (5.7) does not assume such a binary distribution.

will grow. The backbone consists of only a few paths through the network near the percolation threshold, whereas for a perfect array, in which all junctions conduct equally, it would span the whole device.

Experimental observation of molecular exchange

We now show a measurement of the same region in a device with 10 nm nanoparticles before and after molecular exchange of 1-octanethiol (C8) with 1,1',4',1"-terphenyl-4-thiol (TPT). The initial C8 ligand shell around the nanoparticles keeps them from agglomerating and acts as a spacer during film formation. The average gap size of neighbouring nanoparticles thus corresponds to roughly twice the length of octanethiol (1.2 nm, according to Merck Molecular Force Field [149] calculations). From the exchange, we aim to homogenise the current density across the nanoparticle film, in addition to increasing the global conductance of the device. Therefore, a conjugated molecule with a length slightly larger than the starting molecule was chosen, TPT (length ≈1.45 nm). While there is no possibility of bridging adjacent nanoparticles, the π orbitals provide additional sites for hopping transport. Additionally, as TPT is roughly 20 % longer than C8, larger overlaps between TPT molecules attached to neighbouring nanoparticles might be possible. This could provide more conductive paths across larger gaps, also since π-π coupling can be significant [150, 151]. Furthermore, in comparison to thiolated alkanes, lower tunnelling decay coefficients have been reported for para-phenylene oligomers [152], which could contribute to increased conductance after molecular exchange. Thus, when nanoparticle junctions become less resistive, we expect a smoother potential profile between the electrodes.

In fig. 5.12a & b we show KFM images of the network before and after exchange with TPT,[19] respectively. Again, we use graphene to facilitate coplanar bottom contacts. With the source electrode grounded, a voltage of 5 V is applied to the drain electrode on the left. The surface potential undergoes a dramatic change. Many more potential steps are seen post-exchange, making the resulting terraces smaller in area, and also resulting in a decrease of the potential difference between adjacent terraces. The correlation length, estimated as in section 5.4, decreases from 390 ± 210 nm to 230 ± 80 nm, indicating smaller terraces with more uniform size. Furthermore, the global transport characteristics of this device exhibit a higher conductance after molecular exchange, with the total device resistance (including contact resistance) decreasing from 6.5 GΩ to 2.1 GΩ. In both scans the topography as observed by AFM remained virtually unchanged. Due to predominantly tunnelling transport in the

19 For molecular exchange, the sample was immersed in an ethanolic solution of 1 mM TPT under a nitrogen atmosphere and subsequently rinsed in ethanol. The process was done overnight for at least 12 h to ensure a saturation in the increased network conductivity.

network, however, even a slight rearrangement of nanoparticles could change conductance.

From the experimentally obtained potential maps, we reconstructed the distribution of node conductances in a model network of 64 × 73 nodes arranged in a hexagonal lattice. The node potentials calculated from eqs. (5.2) and (5.3) closely match the measured potential landscape. Figure 5.12c & d show the potential and currents in this model network. As in the simulations shown before, the magnitude of the current between individual nodes is drawn as lines of increasing thickness, while the node voltages are shown in greyscale. In these potential reconstructions, we find an increase in the number of current paths after molecular exchange with TPT. The total current in the device is thus more evenly distributed among an increased number of network junctions. This increase in the number of conducting junctions is also evident in the histograms of node-to-node conductance, shown in fig. 5.12e & f, corresponding to the model networks in fig. 5.12c & d. The spatial distribution corresponding to the two prominent peaks in these histograms, each spanning several orders of magnitude of possible conductance values, is shown in the insets.[20] From the integration of the high conductance peaks, we can estimate that a fraction of 18 % and 82 % junctions belong to the backbone before and after exchange, respectively. Therefore, conduction is improved in most parts of the network, leading to a more even distribution of current paths. When compared to the random resistor network model, the system is thus further above the percolation threshold after exchange.

In fig. 5.13 we show topography and KFM of a small area within a different nanoparticle network, before and after exchange with TPT. The 10 nm-diameter nanoparticles are clearly resolved in both cases. While the nanoparticle film features some discontinuities, not all of them form terraces in the surface potential. After introducing TPT the overall potential landscape is smoothed again. The geometric arrangement of the particles remained unchanged, indicating that the molecular environment is likely to be responsible for the changed surface potential post-exchange.

5.6 REACHING THE RESOLUTION LIMIT: PARTICLE-RESOLVED POTENTIAL IMAGING

The nanoparticle devices shown before in this chapter had channel lengths of more than 1 µm, well beyond the typical grain size or correlation length of few hundred nanometres. Accordingly, there is only little variation of the potential drop on each

20 Interestingly, the histograms show two peaks with nearly log-normal distributed conductances. At the moment it is not clear whether these distributions are really a result of the distance dependence of tunnelling current, or whether they are merely a byproduct from the least-squares reconstruction. No external assumptions or limitations on possible distributions are imposed for the conductance reconstruction.

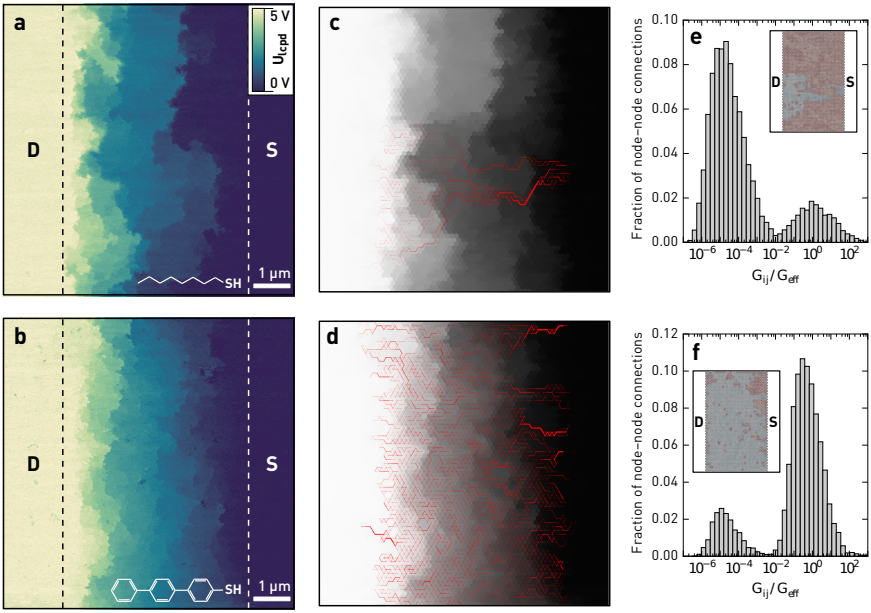

FIGURE 5.12: (a) KFM image of a network before molecular exchange, with a total device resistance of 6.5 GΩ. The nanoparticles in the network are capped with 1-octanethiol molecules. (b) KFM image of the same region after molecular exchange with TPT molecules, with a total device resistance of 2.1 GΩ. (c) and (d) show the reconstructed potential landscape for a model network based on the experimentally obtained data in (a) and (b), found through non-negative least squares reconstruction. (e), (f) Histograms of the node-to-node conductance G_{ij} normalised to the effective two-terminal device conductance G_{eff} for the networks shown in (c) and (d). A map of the node-to-node conductance in the network is shown in the insets (blue corresponds to higher conductance).

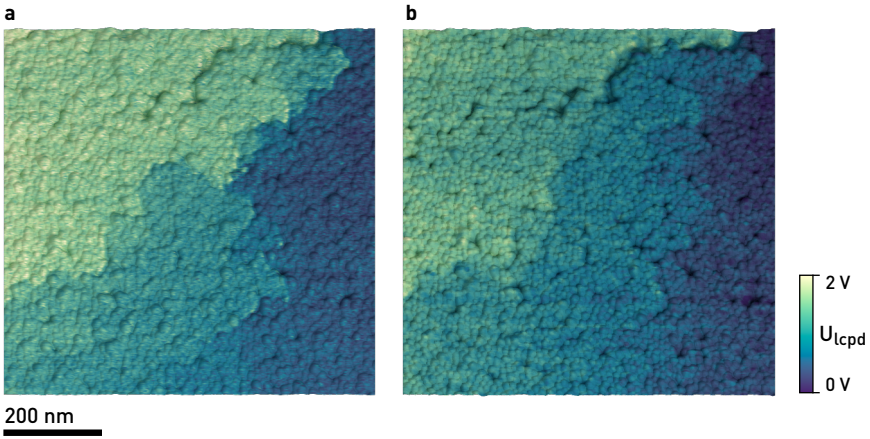

FIGURE 5.13: Topography and superimposed surface potential within the junction of the same device (a) before and (b) after molecular exchange with TPT. In both cases, the source-drain bias is 5 V.

terrace. When the channel length is scaled down to just a few hundred nanometres, where the film is well-ordered and uniform, a larger voltage drop per junction is expected.

The graphene bottom contacts, as introduced before, are suitable for scanning probe lithography and local anodic oxidation [153]. By this technique, graphene is either cut or locally oxidised to graphene oxide by the AFM tip. Figure 5.14 shows a device produced by this technique.[21] A trench was locally oxidised into a graphene strip electrode, resulting in an insulating area of ≈400 nm width and a two-terminal resistance in excess of 100 GΩ. Instead of a transfer of the nanoparticle film by micro-contact printing, the film was scooped directly from the liquid-air interface after self-assembly. The scooped nanoparticle network thus covered the complete sample. Not relying on a stamp as in micro-contact printing, this also minimised the number of defects in the network.

The topography shows the nanoparticle network, again resolving each of the 10 nm nanoparticles in hexagonally close-packed domains. A few defects and bilayer regions are also visible. Owing to better film quality, the potential drops smoothly with only a few notable terraces. Most of these terraces appear near defects in the film. In other areas, the differences in the interparticle conductance are not large enough to cause big steps. The inhomogeneity of the potential drop still indicates meandering current flow through the network.

21 This device was fabricated and measured by Jan Scharnetzky within the scope of his master's thesis [154].

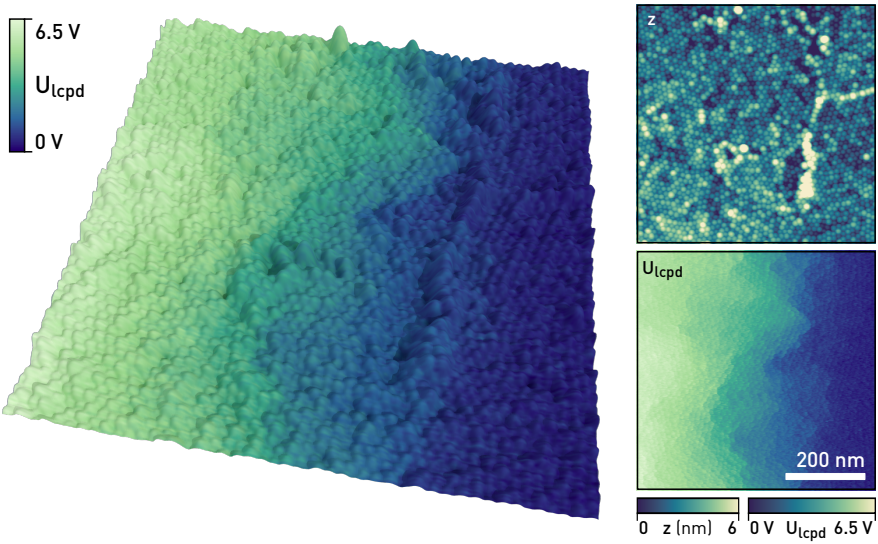

FIGURE 5.14: Particle-resolved surface potential of a nanoparticle network device biased at 6 V, superimposed on the topography scan ($600 \times 600\,nm^2$). The contacts were prepared by local anodic oxidation of the graphene strip used as a bottom contact. The patterned gap width is ≈400 nm. The nanoparticle network shows hexagonally close-packed crystalline domains and only few defects or double layers. Largest drops of the surface potential appear near defects, while individual particles exhibit constant potential. Topography and surface potential of the same scan are shown as individual maps on the right.

The KFM image, obtained with the Kalman-KFM controller and AM-AFM topography feedback in a single scan, shows constant surface potential on top of each nanoparticle. Potential drops between individual nanoparticles appear well-defined and sharp, owing to the force gradient sensitive detection.

5.7 CONCLUSION

In this chapter we have demonstrated how Kelvin probe force microscopy can be used to gain a deeper understanding of the microscopic transport in nanoparticle networks. At room temperature, when the thermal energy exceeds the charging energy, and for this reason the effects of Coulomb blockade are smoothed, junctions between adjacent nanoparticles can be modelled as ohmic resistors. Due to structural disorder in the deposited networks and predominantly tunnelling conduction, resistances are expected to vary over a broad range. The surface potential observed in devices measured in air and at room temperature exhibits a terrace-like potential drop from drain to source. We have interpreted the terraces by a comparison with percolation in random resistor networks.

For devices with non-linear current–voltage characteristics, we could localise the change in differential conductance by KFM. We also measured time constants for charge accumulation and depletion from the time dependence of the surface potential after each change of the backgate potential. By spatial mapping of time constants, we found short decay times in well-connected parts of the network, and large decay times for increasing effective resistance or traps in the oxide underneath the film.

We showed how KFM aids in the evaluation of new types of contacts, such as in bottom-contact graphene electrodes. In our case, graphene electrodes applied to nanoparticle networks have enabled higher resolution measurements by AFM and KFM, since they do not add large topography. For our geometries, we only observed negligible contact resistance in comparison to the nanoparticle network resistance.

We have further shown KFM on a nanoparticle network before and after molecular exchange. After introducing more conductive molecules, potential terraces became more numerous and smaller in size. We could reconstruct a possible realisation of a model network reproducing the measured potential terraces. This allowed us to show dominant current paths through the network. We expect that KFM will prove very valuable for studying molecular electronics on nanoparticle breadboards. Functional molecules, changing their conductance as a result of optical stimulation or gas adsorption, are available for sensing applications [155, 156]. KFM on the breadboards provides a method to track induced changes in the conductance locally.

We have also shown that FM-KFM is capable of resolving individual particles in the surface potential. The particles are detected as islands of constant surface potential and are not related to crosstalk from the topography.

The observation of spatially resolved transport is important for any device with local disorder or tailored functionalisation. It provides valuable information about percolation and local conductivities. Previous studies on local charge transport in similar device structures were based on EFM [157, 158]. The EFM signal however is a function of both the tip–surface capacitance and the surface potential, while in KFM we obtain the surface potential directly. Thereby, we are able to interpret our measurements directly in terms of the voltage drop across the device, which is only possible with further assumptions in EFM. Spatially varying transport is found also in a multitude of other structures. For example, similar terrace-like images could also be seen by EFM already in macromolecular networks of poly-hexylthiophene (P3HT) [159].

Many more effects remain to be explored by KFM on nanoparticle networks. At low temperatures, or when thermally activated transport is excluded, KFM could be used to observe theoretically predicted moving charge fronts as a function of source–drain bias [115]. Another interesting aspect is the use of KFM in combination with local optical excitation. By locally lifting the Coulomb blockade with a laser beam, the conductance of the excited area is expected to increase [147]. KFM would directly map the resulting change in surface potential.

6

DESIGN AND OPERATION OF A HIGH VACUUM BEAM-DEFLECTION AFM

I'd ask my friends to come and see
An octopus's garden with me.
— Ringo Starr, *Octopus's Garden*

Under ambient conditions, quantitative interpretation of Kelvin probe force microscopy measurements is restricted to surfaces and devices which are inert and remain unaffected by air and water. However, many metals and semiconductors grow a native oxide under exposure of O_2, molecular compounds likely degrade in air, and ambient water adsorbs onto surfaces. Whether quantitative measurements are still possible under these circumstances depends on experimental details. For example, passivated nanoscale devices, being covered by a protective oxide layer, can still be investigated in ambient; gold nanoparticle arrays, as shown, are stable for weeks before they degrade.[1]

Since U_{lcpd} sensibly depends on the work functions of surface and probe, measurements are offset by the electrostatic potential caused by surface charges and interfacial dipole layers. Surface contaminations, such as adsorbed water, thereby shift or shield the measured surface potential possibly as a function of time [161, 162]. The tip work function, inferred from measurements of a reference surface, is not guaranteed to stay constant for subsequent investigations. Meaningful work function measurements of unknown surfaces are complicated for this reason.

A vacuum environment is highly beneficial for quantitative KFM. Without ambient viscous damping, the cantilever quality factor can reach 10k–100k for minimising the contribution of thermal noise to force gradient measurements.

In this chapter, we describe the construction of a custom AFM for electrical characterisation of nanoscale devices in vacuum. Ultra-high vacuum (UHV) setups reach ultimate pressures of 10^{-9} mbar and below using copper gaskets, bakeout, and a separately pumped airlock. We aimed for a high vacuum (HV) setup instead because of the flexibility gained in construction and handling. Sealed with Viton® rubber gaskets, we achieve pressures below 10^{-6} mbar by pumping overnight. For highest sensitivity to electrostatic forces, we built the AFM around an optical beam deflection with a fibre-coupled 785 nm diode laser and a custom high frequency four-quadrant

1 Nonetheless, surface coverage of water can enable electrochemical processes as a side effect of applied voltages [160].

photodiode readout. Laser alignment and sample positioning is eased by an integrated optical microscope.

6.1 SYSTEM OVERVIEW AND MECHANICAL DESIGN

Our vacuum setup is shown in fig. 6.1. For isolation of building and ground vibrations, the vacuum chamber is mounted on a frame made of $80 \times 80\,\mathrm{mm}^2$ aluminium extrusions (item, Switzerland), seated on air-damped pistons of an optical table (63-500, TMC, USA). For additional decoupling from people walking around in the lab, we placed the table on pedestals filled with quartz sand, which sit on concrete ground below the elevated lab floor tiles.

The AFM is housed inside a 1.4301 stainless steel modular vacuum chamber (Pfeiffer Vacuum, Germany), fixed to a base plate with a DN160 ISO-K bottom flange used for pumping. For easy access to the AFM and convenient sample and probe exchange, the upper part of the cylindrical vacuum chamber (DN250, height 225 mm) is equipped with a quick-lock door (DN160) and window. Below, a ring (DN250, height 100 mm) with eight DN40-KF ports allows the connection of feedthroughs or extensions.[2] For electrical signals, two ports provide 4 coaxial SMA feedthroughs each (Huber+Suhner, Switzerland). One port couples in the optical fibre for the laser. A DN100 flange on the back side is equipped with multi-pin feedthroughs (LEMO, Switzerland) for power supply and positioners.

To enable optical microscopy with the objective lens inside the vacuum chamber, an antireflective-coated window with 45 mm free aperture is integrated into the top cover of the chamber (VACOM, Germany). Reflected light illuminator, tube lens, and digital camera are mounted on top.

The vacuum chamber is equipped with three pumps. For rough pumping down to $\approx$1 mbar we use a membrane pump (MVP 070-3, Pfeiffer Vacuum) with a pumping speed of $3.8\,\mathrm{m}^3\,\mathrm{h}^{-1}$. Not relying on oil, the dry pumping principle ensures a vacuum clean of additional hydrocarbons. After rough pumping, a turbomolecular pump (HiPace 300, Pfeiffer Vacuum; $260\,\mathrm{L\,s}^{-1}$) reduces pressure to 1×10^{-6} mbar and below. Since both these pumps couple mechanical vibrations to the chamber, we turn them off during measurements, and an ion getter pump (300L, Gamma Vacuum, USA; $300\,\mathrm{L\,s}^{-1}$) takes over. To this end, both turbomolecular and ion pump can be partitioned off the chamber using gate valves (VAT, Switzerland). The chamber pressure is monitored using a combined Pirani/cold cathode vacuum gauge (PKR 251, Pfeiffer Vacuum) for a full range of 1000 down to 5×10^{-9} mbar.

In fig. 6.2 we show the mechanical setup inside the vacuum chamber. All custom parts are machined from aluminium. As with every scanning force microscope, we

2 For its eight arms and friendly look, the AFM was nicknamed *Octopus*.

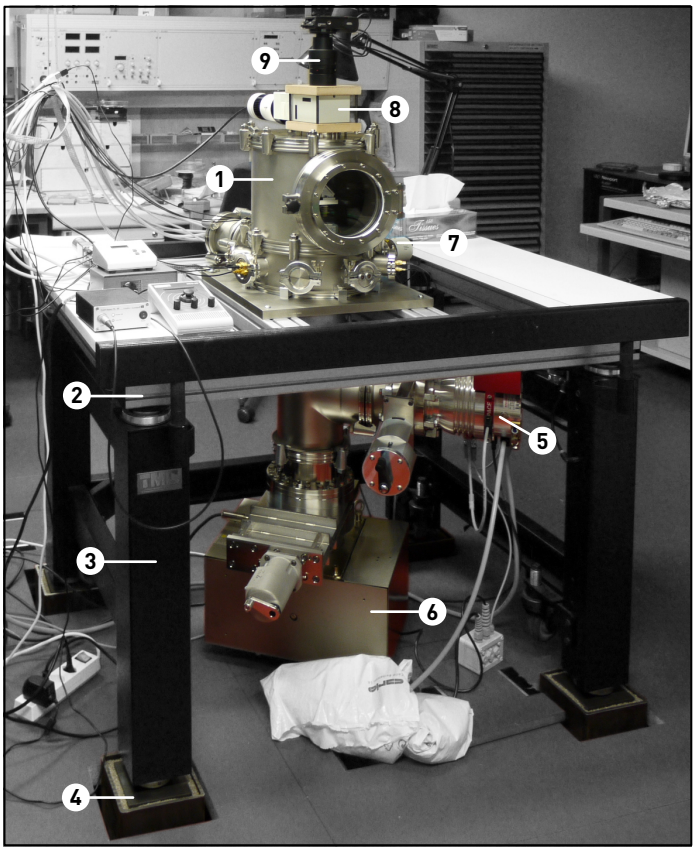

FIGURE 6.1: *Overview of the homebuilt AFM.* The modular vacuum chamber (1) is equipped with a quick-lock door for convenient access to the microscope housed inside. Eight DN40-KF ports allow mounting of electrical or optical feedthroughs. The chamber is fixed on a frame made of aluminium extrusions (2), resting on the pistons of an optical table (3), which is placed on pedestals filled with quartz sand (4). Both the turbomolecular (5) and ion pump (6) can be partitioned off the chamber via gate valves. A combined Pirani/cold cathode gauge (7) monitors pressure. Reflected light illuminator (8), tube lens, and digital camera (9) enable optical microscopy.

need a probe, a mechanism to move this probe in three axes relative to the surface of a sample, and a handle on forces acting on the probe. Our system is based on microfabricated cantilevers with a sharp tip at the end of their beam. By the cantilever stiffness, forces acting on the tip translate into a deflection, which we detect by the displacement of a laser beam reflected off the cantilever. In our setup, all elements related to probe and optical beam deflection form the AFM head assembly, which is mounted on a linear stage for coarse approach vertically down to the sample. Because the vertical axis must be as rigid as possible, we use a stepper-driven linear stage (3) with a threaded spindle and a vertical load capacity of 5 kg (PLS-85, PI miCos, Germany). Full steps on the stepper motor correspond to ≈5 µm linear movement, with 26 mm travel in total. A stepper motor controller capable of 64 microsteps is used for smooth adjustments (SMCI12, Nanotec, Germany).

The sample is mounted on a flexure-guided piezo scanner (2) with closed-loop control over $10 \times 10 \times 10\,\mu m^3$ (Nano-HS3, MadCityLabs, USA). The noise floor of its piezoresistive position sensors is at $1\,pm\,Hz^{-0.5}$ below 1 kHz, thereby making accurate low-noise topography measurements possible. The scanner is mounted on a *xy* stage driven by linear stick-slip positioners (1) (SLC-2460, SmarAct, Germany) for coarse positioning the sample below the AFM probe (35 mm travel range in both directions).

The AFM head comprises a 20× objective lens (6) for optical microscopy. Cantilevers are mounted on a custom probe holder (4), which is easily removable through the front chamber window for tip replacement. Once mounted to its base, the probe holder can be positioned in three axes via linear stick-slip drives (5) (SLC-1730, SmarAct). Guided by the integrated optical microscope, the laser spot can thereby be focused and positioned precisely on the cantilever beam.

The optical beam deflection setup is mounted on top of the head bracket (c). We describe it in detail in the next section. The optical fibre enters the fibre collimator, mounted for fine adjustments of ±0.25 mm in a *xy* flexure translation mount (8) (CP1XY, SM1A1, AD12F; Thorlabs, Germany), and leaves through a beam splitter cube and $\lambda/4$ plate to a notch beamsplitter mirror (7) at 45°. The latter is clamped inside a custom mount, which can be moved in one axis along a slotted hole for coarse position adjustments. These adjustments are done only once, aided by the flexure stage, in order to set the incident angle of the laser spot onto the cantilever beam. Ultimately, the deflected beam from the cantilever reaches the four-quadrant photodiode mounted on the photodiode readout circuit board (10). For centring the beam on the photodiode, we use a tip/tilt adjustable mirror (9) with stick-slip drive (STT-12.7, SmarAct), mounted on a bridge-like support whose coarse alignment is facilitated by slotted holes.

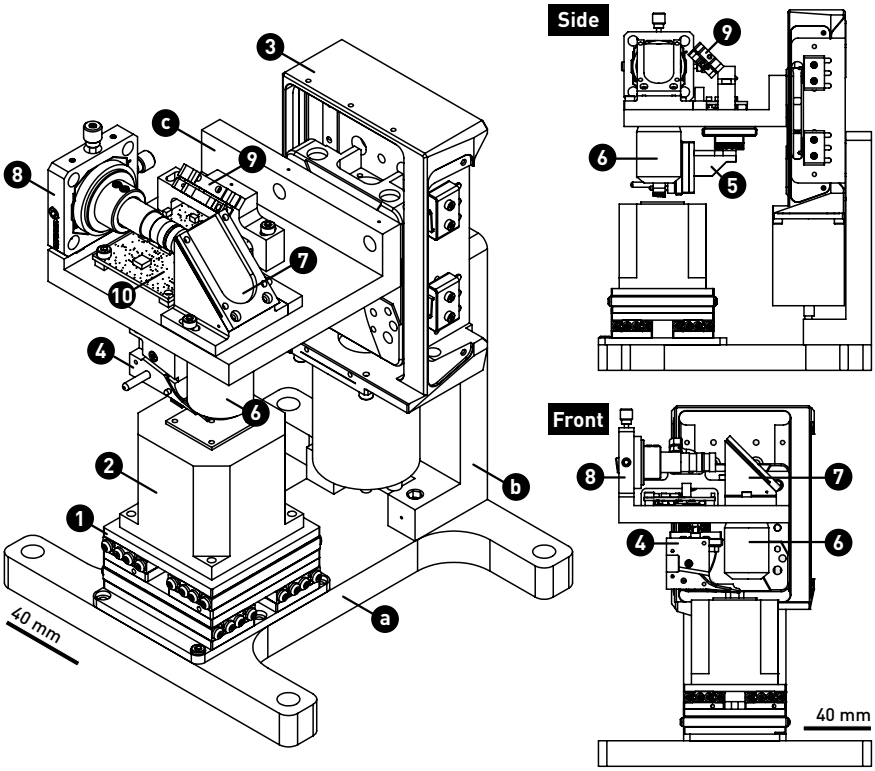

FIGURE 6.2: *Isometric, side, and front view of the mechanical setup within the vacuum chamber.* Optical beam deflection and probe holder form the AFM head assembly, which is fixed onto a vertical positioner for coarse approach to the sample, mounted on top the *xyz* piezo scanner.
Sample stage: (a) base plate, (1) *xy* stick-slip coarse positioner, (2) *xyz* piezo scanner ($10 \times 10 \times 10\ \mu m^3$); *Coarse approach:* (b) angle bracket, (3) *z* stage with stepper motor; *Head assembly:* (c) angle bracket, (4) probe holder, (5) *xyz* stick-slip coarse positioner, (6) 20× objective lens, (7) notch beamsplitter mirror at 45°, (8) *yz* alignment stage with fibre collimator, beamsplitter cube, and $\lambda/4$ plate, (9) tip/tilt mirror with stick-slip drive for centring the reflected laser spot on the (10) four-quadrant photodiode, soldered to the readout circuit board.

The functional parts of an AFM are easily identified in fig. 6.2. Each element is ready for future extensions. For example, the scanner could be exchanged, or a probe holder for tuning forks or length-extension resonators could be introduced. Besides optical beam deflection, cantilevers could also be excited photothermally.

6.2 OPTICAL BEAM DEFLECTION

The optical beam deflection setup is schematically depicted in fig. 6.3. We are using the light of a near-infrared laser diode (1) at 785 ± 15 nm (51nanoFCM, Schäfter+ Kirchhoff, Germany). For reduced coherence length and minimised mode-hopping noise, the laser diode is modulated at radio frequencies. It allows operation at constant power of up to 10 mW (with < 0.1 % *rms* power noise below 1 MHz). The linearly polarised Gaussian beam is coupled into a polarisation-maintaining optical fibre (NA = 0.13) and enters the vacuum chamber via a feedthrough. At its end, the fibre is polished at 8° for reduced back-reflection into the optical path (FC-APC connectors).

The fibre enters the fibre collimator (2) (60FC-4-M5-10, $f' = 5.1\,\mathrm{mm}$, S+K), leaving as a Gaussian beam of $\varnothing_{\mathrm{beam}} = 1.09 \pm 0.05\,\mathrm{mm}$ diameter ($1/e^2$ of Gaussian intensity distribution). The beam passes through a polarising cube beamsplitter (3) (5PF-C-750-L, S+K) and a $\lambda/4$ plate (5WP-4-780-L, S+K), both of which are fixed to the collimator. The $\lambda/4$ plate, rotated by 45° to the linear polarisation, alters the beam to be circularly polarised.

The beam hits a notch beamsplitter mirror (4) (NFD01-785-25x36, Semrock, USA) at 45°, reflecting only within a narrow band around the laser wavelength. The infinity-corrected 20× objective lens (5) (LMPLFLN20x, Olympus, Japan; $f_{\mathrm{obj}} = 9\,\mathrm{mm}$, NA = 0.4, working distance 12 mm) focuses the incident beam onto the cantilever (6) placed underneath. Thereby, a laser spot of $\varnothing_{\mathrm{spot}} = 8.3 \pm 0.4\,\mu\mathrm{m}$ diameter is obtained.[3] Upon reflection on the cantilever, the circular polarisation changes handedness, and the beam returns back through the objective lens.

Ideally, the laser beam should hit the cantilever surface perpendicularly. Because the cantilever is mounted at an angle of $\alpha_0 \approx 12°$ in our case, to counteract approximately the tilt of many commercial tips, the beam has to enter the back focal plane of the objective at a distance h to the optical axis, where $h = f_{\mathrm{obj}} \sin\alpha_0$. These adjustments are possible by translating the notch beamsplitter mirror or the flexure translation mount of the fibre collimator. By the same principle, any deviation in the cantilever tilt angle translates the reflected beam with respect to the incident beam. For example, a force exerted on the cantilever bends the cantilever locally, and the incident beam is thereby reflected at a slightly different angle. When the cantilever is

3 $\varnothing_{\mathrm{spot}} = 4\lambda f_{\mathrm{obj}}/\pi\varnothing_{\mathrm{beam}}$, assuming a Gaussian beam profile [163].

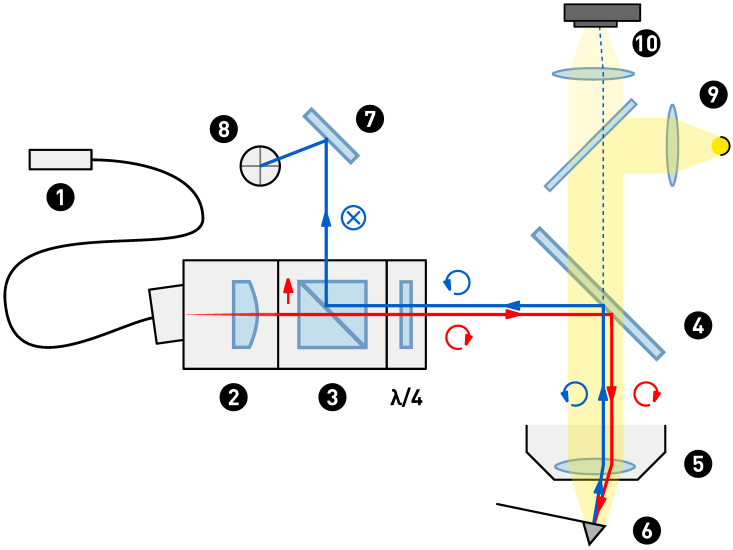

FIGURE 6.3: *Setup of optical beam deflection and light microscope.* Light from the 785 nm laser diode (1) enters the vacuum chamber via a single-mode optical fibre, is collimated (2) for a Gaussian beam of 1.1 mm diameter. The linearly polarised beam passes through a beamsplitter cube (3) and $\lambda/4$ plate. Now circularly polarised, it is reflected by a notch beamsplitter mirror (4) and focused by the 20× objective lens (5) onto the cantilever (6) for a spot size of ≈9 µm. The reflected beam returns with reversed handedness to the $\lambda/4$ plate, polarising it linearly but perpendicularly to the original light. The returning beam is deflected by the polarising beam splitter and positioned by a tip/tilt mirror (7) onto the four-quadrant photodiode (8). Displacements of the reflected beam, caused by changed cantilever inclination, hereby modulate the quadrant currents, which the photodiode readout amplifies and turns into vertical and horizontal deflection signals. For optical microscopy, white LED light (9) is directed through the objective lens, and the reflected image of surface and tip is projected onto the CMOS sensor of a digital camera (10).

deflected by Δz at a distance L from the cantilever base, the reflected beam is thereby shifted by $\Delta h = 2f_{\mathrm{obj}}\Delta z/L$, travelling back from the objective lens. With the spot positioned at the end of the cantilever, near the tip, and a cantilever of length L, this provides an optical amplification of the cantilever deflection.

The deflected beam passes through the $\lambda/4$ plate again and is converted by to linear polarisation. Due to its reversed handedness, however, the linear polarisation is at right angle to the original beam polarisation. Therefore, the beam leaves the polarising beamsplitter (3) cube sideways through a hole drilled into the case. The tip/tilt mirror (7) (05D20BD.2, Newport, USA; broadband dielectric mirror 700 – 950 nm) directs the beam onto the four-quadrant photodiode (8) (SD 085-23-21-021, Advanced Photonix, USA).

The photodiode is soldered to the readout circuit board in order to keep wires short, and to minimise stray capacitance and noise sources coupling in. For optimum shielding of critical signals, the circuit board features 6 layers, several of them used as ground planes. No solder mask is used, in order to reduce the amount of outgassing inside the chamber. The circuit itself is based on a translinear four-quadrant readout designed by Raoul Enning for his PhD thesis in our group [68]. The photodiode currents are first copied by bipolar current mirrors. The sum and normalised vertical and horizontal signals are then obtained directly by arithmetic using these copies and bipolar current mirrors. The conversion of the resulting currents into voltages is done at the final stage using operational amplifiers, configured as transimpedance amplifiers. Bandwidths of up to 20 MHz and shot noise limited operation are feasible [67].

For the Gaussian beam profile in our setup, we can calculate the expected photodiode and readout response as follows. The beam profile is given by

$$S(x,y) = S_0 \exp\left(-\frac{2}{w^2}(x-x_0)^2\right)\exp\left(-\frac{2}{w^2}(y-y_0)^2\right), \tag{6.1}$$

where w is half the beam width determined by the decay of the intensity to $1/e^2$, thus $\varnothing_{\mathrm{beam}} = 2w$. S_0 is related to the total beam power by $S_0 = 2P_{\mathrm{tot}}/\pi w^2$. For the powers incident on each quadrant, we need to integrate $S(x,y)$ over each quadrant area. Assuming that each quadrant occupies a quarter of the two-dimensional space (thus, in the limit of a photodiode large in size compared to the beam diameter), the change in the vertical power difference by small displacement of the beam, Δh, is [164]

$$\Delta P_{\mathrm{v}} = P(\text{upper quadrants}) - P(\text{lower quadrants}) = P_{\mathrm{tot}}\sqrt{\frac{2}{\pi}}\frac{2\Delta h}{w}. \tag{6.2}$$

Since in our system the vertical deflection signal is normalised by the incident power, the output voltage is

$$U_\mathrm{v} \propto \frac{\Delta P_\mathrm{v}}{P_\mathrm{tot}} = 2\sqrt{2\pi}\left(\frac{\varnothing_\mathrm{spot}}{L}\right)\left(\frac{\Delta z}{\lambda}\right), \tag{6.3}$$

where we have expressed Δh and w by the cantilever deflection Δz and the spot size on the cantilever, $\varnothing_\mathrm{spot}$. For maximum sensitivity, the laser spot should fill the cantilever as far as possible, without loss of light [164].[4,5]

Ideally, detection noise is only limited by the discrete nature of photons with an energy $\hbar\omega = hc/\lambda$ (*shot noise*). During the time Δt an average number $\langle n\rangle = P_\mathrm{tot}\Delta t/\hbar\omega$ of photons is expected to hit the detector. Using Poisson statistics, i.e. assuming independent events, the variance σ_n^2 equals the expected number $\langle n\rangle$, and therefore the signal-to-noise ratio behaves as $\sqrt{\langle n\rangle} \propto \sqrt{P_\mathrm{tot}}$.[6] Hence, there is a tradeoff between high laser power, reducing detection noise, and heating of the cantilever, increasing thermal noise.

A beam deflection AFM is thus both limited by diffraction and shot noise. Additional noise contributions from the photodiode readout are minimised in our implementation using arithmetic with photodiode currents and a low noise output stage. The capability of operating at high frequencies and the small spot size below 10 µm enable the use of short cantilevers, which are crucial for low noise and high bandwidth detection for KFM, as discussed in section 3.4.

For optical inspection during AFM operation, sample positioning, and to aid laser spot alignment onto the cantilever, illumination and observation components of an optical microscope are set up outside the vacuum chamber. An LED white light source (9) (pe-100wht, CoolLED, United Kingdom) is coupled into an illuminator for reflected light microscopy (U-KMAS, Olympus). The tube lens (10) (U-TLU, Olympus) and C-mount adapter (U-CMAD3, U-TV1X; Olympus) project a real image of the surface and tip onto the CMOS sensor of a digital camera (α5100, Sony, Japan).

4 Note that this expression is independent of the focal length of the objective lens. Although the deflection on the photodiode is enhanced by the optical lever $\propto f_\mathrm{obj}/L$ mentioned above, the beam width also depends on f_obj.

5 There sensitivity given here assumes a rigid cantilever, rotating in total as a result of forces acting on the tip. This is only an approximation to the first eigenmode in Euler-Bernoulli beam theory. For the sensitivity at higher eigenmodes, the exact deflection curve of the cantilever must be regarded instead.

6 Using $\Delta P_\mathrm{v}/P_\mathrm{tot} = 1/\sqrt{\langle n\rangle}$ and relating Δt to the bandwidth B as $\Delta t = 1/2B$, we can estimate the shot noise contribution to the deflection power spectral density as $d^z_\mathrm{ds,shot} = \sqrt{\hbar c\lambda/2P_\mathrm{tot}}\, L/\varnothing_\mathrm{spot}$. At 785 nm and 1 mW, we expect $d^z_\mathrm{ds,shot} = 3.5\,\mathrm{fm\,Hz^{-0.5}}\, L/\varnothing_\mathrm{spot}$.

6.3 OPERATION

For AFM operation, we employ a commercially available scan controller (Nanonis RC4, SC4; Specs, Switzerland). The x, y, and z scan signals are fed into the high-voltage amplifier and closed-loop controller (Nano-Drive, MadCityLabs). We command the x and y axes as setpoints in the closed-loop feedback. For faster response of the topography feedback, the z piezo is driven without closed-loop feedback. Instead, we record the z position sensor readings along with the scan.

For dynamic AFM operation, we employ a high frequency lock-in amplifier and PLL (HF2, Zurich Instruments). It generates the sinusoidal drive signal for the shaker piezo and also applies the tip voltage for our Kalman-KFM controller, implemented as a real-time program running on the instrument. The detected resonant frequency shift (FM-AFM), or the amplitude (AM-AFM), is fed into the scan controller for topography feedback.

In fig. 6.4a, we show the front view of the measurement chamber. After venting, the front door can be opened for quick exchange of sample and probe. The probe holder, depicted closer in fig. 6.4b, is fixed in place by a single screw in the middle, guided by two dowel pins (on the lower and upper right). The holder can thus be easily detached and pulled from the base for probe exchange outside the chamber. Electrical connections from the probe holder to its base are established via spring-loaded pins (813-S1, PreciDip, Switzerland). The shaker piezo is a 3 mm × 4 mm × 0.5 mm plate cut from lead circonate titanate (PZT) ceramics (PIC-255, PI Ceramic, Germany). The piezo is glued with conductive epoxy between two pieces of copper-clad FR4 circuit board, 0.35 mm thick, for electrical contacts and insulation, and glued with epoxy to the holder. The cantilever, placed on top of this stack, is held in place by a beryllium copper (CuBe) leaf spring, which also provides the electrical contact to the probe. To reduce crosstalk and diminish electromagnetic pickup, we use twisted pair magnet wires for the piezo connections, and we shield the probe connection in a coaxial cable.

After inserting the probe holder, the optical microscope and the xyz positioners at the base of the probe holder are used to put the cantilever beam in focus and under the laser spot. The vertical and horizontal beam deflection outputs are centred using the tip/tilt mirror. The inset in fig. 6.4b shows an optical micrograph of cantilever (AC160, Olympus) and laser spot in focus above a device.

Samples are mounted magnetically on top of the scanner and positioned using the xy linear stage. For electrical contacts to nanoscale devices we use a probe card with 2 × 7 CuBe needles (IBM), which are placed on lithographically defined contact pads and clamp the wafer piece.

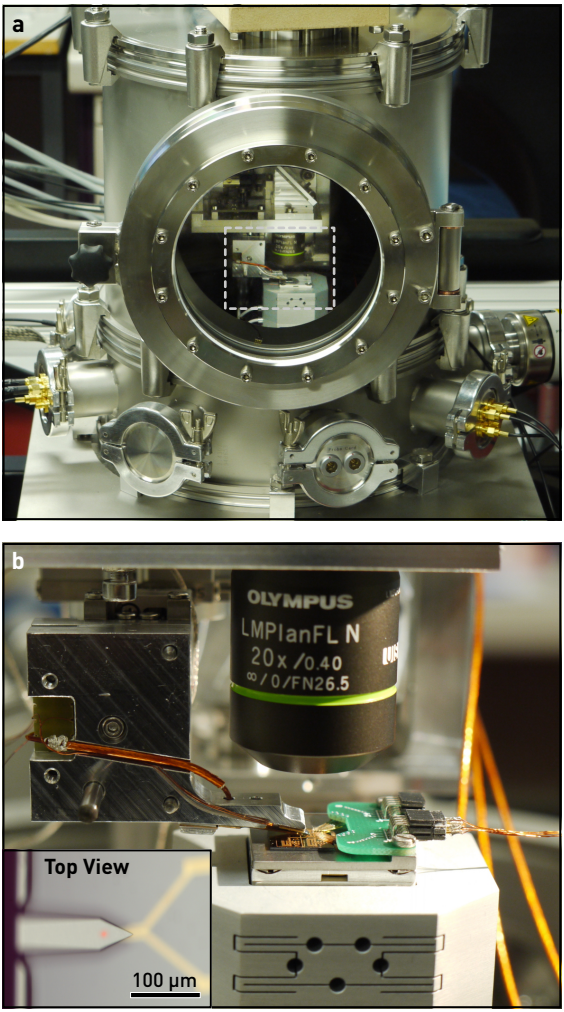

FIGURE 6.4: (a) Front view of the vacuum chamber with the AFM setup inside. After venting, the quick-lock door on the front can be opened for sample and probe exchange. (b) Close-up view of probe holder, objective lens, and the closed-loop piezo scanner. The probe holder is mounted on a *xyz* stick-slip linear stage for moving the cantilever to the laser spot position. For convenient probe exchange, the holder is fixed in place by a single screw and two dowel pins used as linear guides. Samples are mounted atop the scanner magnetically. Wafer pieces with nanoscale devices are electrically contacted by a probe card with beryllium copper needles. The inset shows cantilever, laser spot, and surface as seen through the optical microscope.

The chamber is evacuated by turning on the prevacuum and turbomolecular pump (the gate valve of the latter opened). Below ≈1 mbar the turbomolecular pump's rotational speed increases to 1000 Hz, and the chamber pressure is reduced further to below 10^{-6} mbar. We show an exemplary pumpdown curve in fig. 6.5.

The ion pump can be added after reaching pressures of below 10^{-5} mbar; otherwise its pumping speed and life time might be reduced, making a bake-out and regeneration of the cathode elements necessary. Adding the ion pump further decreases pressure, due to the increased pumping speed, as shown in the inset of fig. 6.5. After closing the turbomolecular pump's gate valve, both mechanical pumps can be turned off, and the ion pump alone can maintain the pressure in the chamber. The ion pump has no moving parts and only needs a high *dc* voltage for operation, thereby minimising vibrations for high-resolution scanning probe microscopy. The ion pump is kept running at all times, even after venting the main chamber to atmospheric pressure, by closing its gate valve.

In fig. 6.6a, we show the power spectral density of the vertical deflection signal over time. Initially, both mechanical pumps were shut down; only the ion pump maintained the pressure. After 10 s, we switched on the prevacuum and turbo pump. As a consequence, the turbo pump frequency increased linearly over time to 1000 Hz at $t = 170$ s. Due to the mechanical coupling of the turbo pump to the vacuum chamber, slight imbalances in its rotors also cause vibrations in the beam deflection. Thus, we can identify the turbo pump frequency in the power spectral density of the vertical deflection signal as a peak moving up to the terminal rotational speed of the pump. Several overtones are also seen.

While the turbo pump increases its rotational frequency, it excites structural resonances of the setup. We can identify them by plotting the excited amplitude over the turbo pump's momentary rotational frequency, as shown in fig. 6.6b. At the moment, we use no additional measures to isolate our AFM setup. Any acoustical noise coupled to the AFM base is likely to cause an effect when different parts of the setup oscillate at dissimilar phase. Some of the peaks between 300 Hz and 500 Hz might correspond to structural resonances of the aluminium extrusions used for frame construction.

Vibrations from both mechanical pumps also excite broadband acoustical noise, which is shaped by mechanical resonances of chamber and setup (fig. 6.6a). When only the ion pump is in operation, this strong background is gone.

6.4 THERMAL NOISE IN AIR AND VACUUM

In a vacuum environment there is no additional viscous damping to the cantilever, hence the amplitude at resonance is limited by internal damping of the cantilever ma-

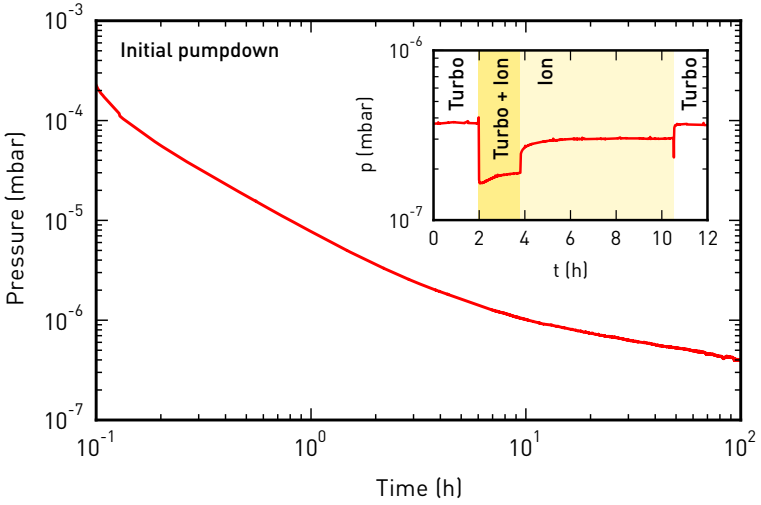

FIGURE 6.5: Pressure in the measurement chamber over time after venting with N_2, using only the prevacuum and turbo pump. A pressure of 8×10^{-6} mbar is reached after one hour. Further pumping reduces the pressure below 1×10^{-6} mbar after 10 hours and 4×10^{-7} mbar after 100 hours. The inset shows how adding the ion pump affects pressure.

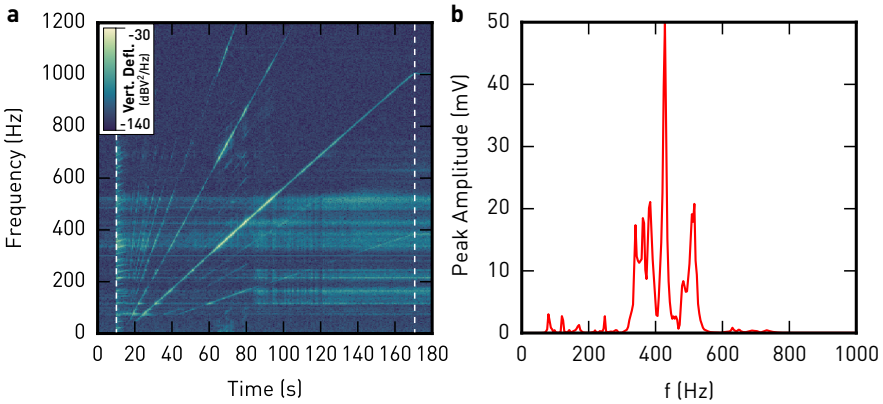

FIGURE 6.6: (a) Power spectral density of the vertical deflection signal over time. After switching on the prevacuum and turbo pump at $t = 10$ s, the turbo pump frequency increased to 1000 Hz at $t = 170$ s. (b) By plotting the excited amplitude over the turbo pump frequency, mechanical resonances in the setup can be identified.

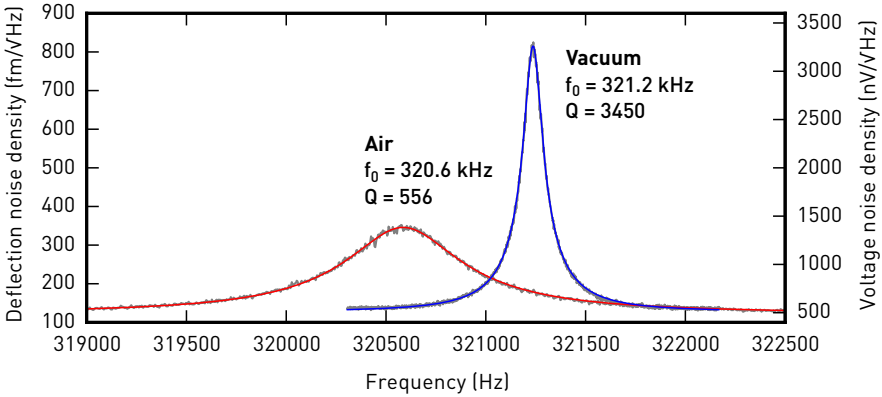

FIGURE 6.7: Vertical deflection power spectral densities near the first eigenmode of an AC160TS-R3 cantilever in air and vacuum. From the thermal noise measurement in air, the cantilever spring constant is $k = 43\,\mathrm{N\,m^{-1}}$ as determined from f_0 and Q using the Sader method [43]. The beam deflection sensitivity and noise floor is at $250\,\mathrm{nm\,V^{-1}}$ and $125\,\mathrm{fm\,Hz^{-0.5}}$, respectively.

terial only. In fig. 6.7 we show vertical deflection power spectral densities (PSD) of an Olympus AC160TS-R3 cantilever measured in our setup at a laser power of ≈1 mW. From the thermal peak at resonance, we find a resonant frequency of 320.6 kHz in air with a quality factor of ≈560. These values are typical for this kind of cantilever. The spectrum is free from discrete noise peaks. Using the Sader method [43], eq. (2.26), we estimate a spring constant of $\approx 43\,\mathrm{N\,m^{-1}}$. From a fit of white detection noise and thermal noise, according to eq. (2.18), we obtain a beam deflection sensitivity of $250\,\mathrm{nm\,V^{-1}}$ and a detection noise floor of $500\,\mathrm{nV\,Hz^{-0.5}}$ (equivalent to $125\,\mathrm{fm\,Hz^{-0.5}}$). These cantilevers are approximately 160 µm long, and therefore our laser spot fills them to less than one tenth. Using short cantilevers on the order of 10 µm length, we expect to find detection noise levels below $10\,\mathrm{fm\,Hz^{-0.5}}$ as demonstrated for our readout circuit [68].

After pumping down to 1×10^{-6} mbar, the thermal peak shifted to a higher frequency of 321.2 kHz for the same cantilever, and the quality factor increased to about 3500; both effects are due to the lack of viscous damping. One reason for the still rather low Q factor could be losses in the cantilever mount. A large spread in Q for cantilevers clamped by springs has been noticed before [165]. Best results are expected for cantilevers glued to the shaker piezo.

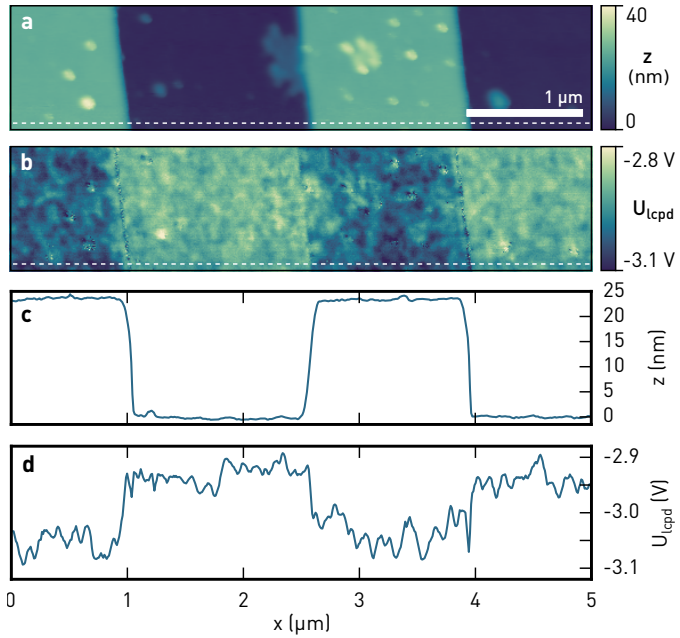

FIGURE 6.8: (a,c) Topography and (b,d) surface potential of a TGZ01 calibration grating (MikroMasch) showing 23 nm-high lines etched into SiO_2 on a Si wafer at a pitch of 3 µm. The line profiles in (c,d) are taken along the dashed lines indicated in (a,b). (Scan parameters: $\Delta f = -20$ Hz, $A \approx 7$ nm, $U_{ac} = 2$ V, $f_m = 1$ kHz, $f_0 = 317.6$ kHz, $Q = 2290$, $v_{tip} = 626$ nm/s)

6.5 SCAN OF A CALIBRATION GRATING

We show a FM-AFM scan of a calibration grating in fig. 6.8. The grating features lines of ≈23 nm height etched into SiO_2 on a Si wafer (TGZ01, Mikromasch, Bulgaria). The structure repeats every 3 µm. The topography image (fig. 6.8a) shows the grating as expected. We did not need to adjust the *x*, *y*, and *z* axis calibration as provided by the scanner manufacturer. The topography also shows a few spots of adsorbed debris since the surface was not cleaned prior to the measurement.

In addition to topography, we also obtained the surface potential using the Kalman-KFM controller (fig. 6.8b). The elevated regions in the topography are about 100 mV lower in surface potential. All regions show a locally fluctuating surface potential of ≈25 mV *rms* with patches on the order of 100 nm in size. These are likely caused by charges trapped in SiO_2. The adsorbates seen in the topography scan appear only

slightly higher in surface potential, but overall do not dominate the measurement. While the calibration grating was grounded on the back side, the measured U_{lcpd} is at $\approx -3\,\mathrm{V}$. Both tip and grating are made from silicon; hence the large negative background is a result of a net negative surface charge on the grating.

6.6 POTENTIAL DROP IN NANOPOROUS FULLERENE NETWORKS

Similar to the nanoparticle networks in chapter 5, an irregular potential drop is expected in every percolating system. We have performed first experiments on devices with nanoporous networks of buckminsterfullerene, C_{60}. Due to their increased interfacial area, C_{60} networks can be used, for example, to improve charge separation in organic solar cells [166].

In our case, a single-layer two-dimensional C_{60} network self-assembled on the water-air interface, as for the formation of nanoparticle arrays [109]. Rapid evaporation of solvent causes the C_{60} nanoparticles to form interdigitated networks typical of diffusion-limited aggregation [166]. We transferred the network from the water/air interface onto a Si/SiO_2 wafer piece with gold electrodes defined by electron-beam lithography.

The patterned electrodes were contacted by the probe card, as shown in fig. 6.4b. Figure 6.9 shows single-scan FM-AFM and KFM of the device. The network is composed of C_{60} particles of $\approx$10 nm height, which aggregate and fuse to form a percolating network on top of the electrodes and in between, spanning a gap of 1 µm.

The left electrode was grounded during this scan, whereas the right electrode was biased at −1 V. This is also seen in the obtained surface potential, fig. 6.9b. On top of the gold electrodes, the C_{60} network appears $\approx$450 mV higher on average, indicating a reduced work function. Between the electrodes, the surface potential drops smoothly. Differences between C_{60} and the exposed oxide are not as pronounced as on top of the metallic electrodes.

In order to remove the static offset of the work function, we obtained another scan in a double-pass setup. Each scan line is obtained first at an electrode bias of 0 V; then, the line is scanned a second time at a bias of −1 V. Topography and Kelvin feedback remained enabled for both passes. By taking the difference of both scan lines, we can obtain an image of the voltage-induced surface potential only. The result is depicted in fig. 6.10. The electrodes now appear uniform in potential, indicating that the static offsets were successfully eliminated. The smooth potential drop in between the gold electrodes indicates conduction well above the percolation threshold. This is expected, since the nanoporous network exhibits good surface coverage and connectivity. Some local variations in the potential drop can still be seen, as indicated by the equipotential lines. Potential drops of $\approx$0.25 V appear on both electrode edges,

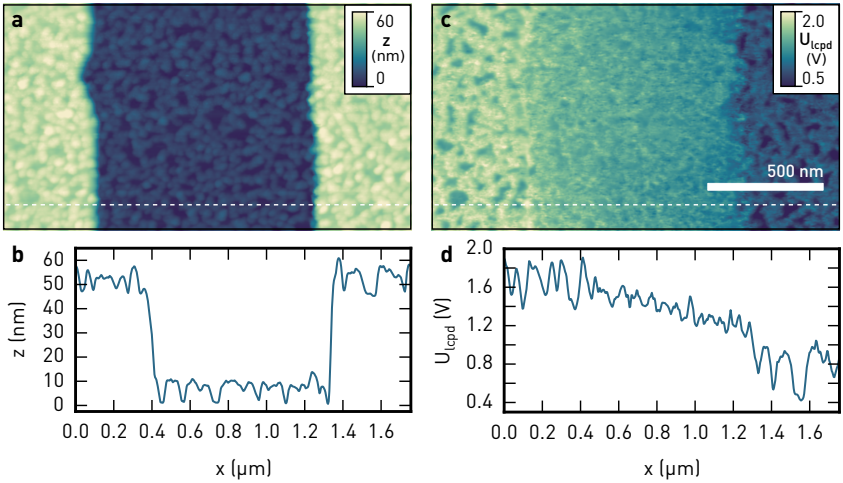

FIGURE 6.9: (a,b) Topography and (c,d) surface potential of a nanoporous network of C_{60} deposited onto a patterned substrate with 45 nm-high gold electrodes. The device is biased at −1 V on the right electrode. The left electrode is grounded. (Scan parameters: $\Delta f = -8$ Hz, $A \approx 8$ nm, $U_{ac} = 1$ V, $f_m = 1$ kHz, $f_0 = 341.7$ kHz, $Q = 4600$, $v_{tip} = 250$ nm/s)

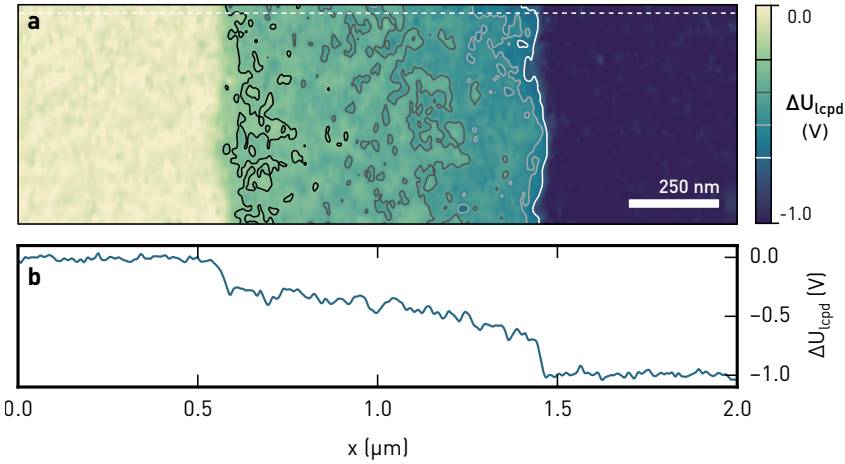

FIGURE 6.10: Voltage drop within the C_{60} network introduced by an externally applied voltage. Each line is scanned twice: first at 0 V, then at −1 V bias on the right electrode; only the difference is plotted. The contours in (a) are equipotential lines between −0.7 V and −0.25 V and highlight the irregular voltage drop within the junction. (b) Line profile.

hinting at a total contact resistance on the order of the channel resistance. This could be caused by the large height of the gold electrodes compared to the C_{60} film, causing it to rupture near the edges.

6.7 CONCLUSION

In this chapter, we have described in detail the design and construction of an AFM for operation in high vacuum. The vacuum chamber can be pumped down over night to pressures below 10^{-6} mbar using a turbomolecular pump. To reduce mechanical vibrations due to mechanical pumps, we also integrated an ion pump which can sustain the high vacuum pressure alone.

Our design is based on an optical beam deflection to detect the cantilever oscillation. The translinear photodiode readout allows the use of high frequency cantilevers, while its noise level stays close to the shot noise limit. The sensitivity and expected optical shot noise were derived for our detector.

The AFM integrates an optical microscope for sample positioning and laser spot alignment. All positioners are remote controlled for beam deflection realignment and repositioning the sample under vacuum conditions.

We have demonstrated the AFM operation on a calibration grating and on a two-terminal device with the channel formed by a nanoporous C_{60} film. In both cases, we performed FM-KFM using the Kalman-KFM feedback loop developed earlier. The nanoporous C_{60} network is an example of devices which will benefit from measurements under vacuum conditions. Since the film is kept protected from environmental influences, degradation or doping from ambient oxygen and water is inhibited. From the potential drop in the electrically biased network, we found contact resistances comparable to the channel resistance, and we could resolve the slightly irregular voltage drop due to the network structure.

7

SUMMARY

The future belongs to those who believe in the beauty of their dreams.

— Eleanor Roosevelt

The focus of this thesis was the characterisation of active nanoelectronic devices by Kelvin probe force microscopy. Owing to the long-range electrostatic interaction between different parts of the scanning probe and the surface, it was necessary to utilise force gradient sensitive detection techniques.

Quantitative measurements, enabled through the force gradient sensitivity in FM-KFM, were in the past performed mainly in ultra-high vacuum environments and in conjunction with FM topography feedback, thereby limiting scans to mostly flat surfaces or slow scanning speeds. However, FM-AFM topography brings only little benefit for device characterisation.

Making direct use of the sidebands appearing with every modulation of the force gradient, our approach decouples KFM signals from the choice of topography feedback. For operation in air, we could thus make use of robust AM-AFM topography. The detailed understanding of the sidebands furthermore helped us to devise and implement a novel KFM feedback scheme based on stochastically optimal control. This Kalman-KFM controller integrates the information from the $2\omega_\mathrm{m}$ sidebands for continuous sensitivity adjustments, thereby reducing geometrical crosstalk due to topography. At the same time, it ensures more accurate surface potential measurements at lower noise than conventional Kelvin feedback based on PID control.

We demonstrated the controller performance on an indium arsenide nanowire as a prototypical device with electrode structures and rough topography. From line profiles of the surface potential measured at different source–drain currents, we could separate the contact resistances from the channel behaviour itself. Such investigations traditionally require four-point probe or transmission line measurements and purpose-made electrode structures, which become difficult to implement as devices shrink further to the nanoscale. We could trace back the non-linear two-terminal output characteristic of the nanowire to effects at the contacts alone, while the channel behaviour remained linear. Furthermore, the pair of contacts was found to display unequal contact resistances.

As a second set of devices, we focused on two-dimensional networks of gold nanoparticles. Due to structural disorder and the tunnelling characteristics between

adjacent particles, these devices exhibit a terrace-like surface potential landscape. The terrace formation was explained by an analogy to percolation in random resistor networks. The nanoscale junctions in these networks also allow the integration of functional molecules to modulate the device conductance. Previous investigations of nanoparticle networks focused only on the macroscopic current flow through two terminals, whereas by KFM we could observe the behaviour at the level of individual junctions within the networks. KFM was also used to investigate the contact resistance to bottom-contact graphene electrodes in nanoparticle devices. Furthermore, we compared the surface potential in devices before and after introducing conjugated molecules. In accordance to the higher two-terminal conductance, we found more terraces of smaller size in the network. Through a reconstruction technique, we could find an arrangement of conductors to reproduce the measured surface potential and thereby visualise dominant current paths in the network.

Finally, an AFM for operation in high vacuum was built for this thesis, in order to enable measurement of devices free of ambient influences. The AFM was designed from the ground up to include a top-view optical microscope for sample and probe alignment. Large survey scans, which might damage the probe, are thus not required. For highest sensitivity to weak attractive forces, we included an optical beam deflection. With a laser spot size below 10 µm and a high-frequency low-noise photodiode readout, small cantilevers with resonant frequencies in the megahertz range can be used. We obtained topography and KFM scans on a device with a nanoporous fullerene network and observed the slightly irregular potential drop within the micron-sized electrode gap. Contact resistances were found to be on the order of the channel resistance itself.

Because of its capability of separating contact effects and mapping the local electrochemical potential in devices under operating conditions, KFM will be an indispensable tool for nanoscale electronic device characterisation in the future. There are many more interesting effects to explore on nanoscale electronic devices. The techniques implemented and advanced in this thesis will make them accessible.

A

APPENDIX

A.1 EFFECTIVE ELECTROSTATIC TIP–SAMPLE FORCES AND FORCE GRADIENTS

In fig. 3.1, we showed the effective C' and C'' as a function of tip–sample distance, calculated for different amplitudes from an analytical approximation of the electrostatic force. We use the following expressions for the electrostatic force, derived by Hudlet *et al.* [62], for the spherical apex and cone

$$F_{\text{apex}}(z) = -\pi\epsilon_0\, U_{\text{ts}}^2 \frac{R\tilde{R}}{z(z+\tilde{R})} = -\pi\epsilon_0 R\, U_{\text{ts}}^2 \left(\frac{1}{z} - \frac{1}{z+\tilde{R}}\right) \tag{A.1}$$

$$F_{\text{cone}}(z) = -\pi\epsilon_0 k^2\, U_{\text{ts}}^2 \left[\ln\frac{H}{z+\tilde{R}} - 1 + \frac{R\cos^2\theta_0/\sin\theta_0}{z+\tilde{R}}\right], \tag{A.2}$$

where $k^2 = (\ln\tan\theta_0/2)^{-2}$, $\tilde{R} = R(1-\sin\theta_0)$, R is the radius of the apex, θ_0 is the half opening angle of the cone, H is the total height of the tip formed by apex and cone, and z is the distance of the apex to the sample plane. In addition, we consider the contribution of the cantilever as a plate capacitor (effective area A) with a separation of $z + H$,

$$F_{\text{lever}}(z) = -\frac{1}{2}\frac{\epsilon_0 A}{(z+H)^2}\, U_{\text{ts}}^2. \tag{A.3}$$

The forces as given above include only terms following either a power law or logarithmic dependence on the distance. In these cases, the integrals for the effective force and force gradient during an oscillation $z = d + A(1+\cos\omega t)$, can be solved as follows. For an inverse power law, $F_{\text{ts}}(z) = -C(z+h)^{-n}$, we find using eqs. (2.3) and (2.4)

$$\begin{aligned}\langle F_{\text{ts}}\rangle(d) = -C\frac{\sqrt{2}}{\pi}(d+h)^{-n+\frac{1}{2}}A^{-\frac{1}{2}} \\ \cdot \int_0^{\sqrt{\frac{2A}{d+h}}} \mathrm{d}y\,(1+y^2)^{-n}\left(1-\frac{d+h}{2A}\,y^2\right)^{-\frac{1}{2}}\end{aligned} \tag{A.4}$$

$$k_{\mathrm{ts}}(d) = C\frac{\sqrt{2}}{\pi}(d+h)^{-n+\frac{1}{2}}A^{-\frac{3}{2}} \cdot 4n\int_0^{\sqrt{\frac{2A}{d+h}}} \mathrm{d}y\, y^2(1+y^2)^{-n-1}\left(1-\frac{d+h}{2A}\,y^2\right)^{\frac{1}{2}}. \tag{A.5}$$

The definite integrals can be expressed[1] in terms of Gauss' hypergeometric function, ${}_2F_1(a,b;c;z)$; thus,

$$\langle F_{\mathrm{ts}}\rangle(d) = -C(d+h)^{-n}\,{}_2F_1\left(\frac{1}{2}, n; 1; -\frac{2A}{d+h}\right) \tag{A.6}$$

$$= -C(d+A+h)^{-n}\,{}_2F_1\left(\frac{n}{2}, \frac{n+1}{2}; 1; \frac{A^2}{(d+A+h)^2}\right) \tag{A.7}$$

$$k_{\mathrm{ts}}(d) = nC(d+h)^{-n-1}\,{}_2F_1\left(\frac{3}{2}, n+1; 3; -\frac{2A}{d+h}\right) \tag{A.8}$$

$$= nC(d+A+h)^{-n-1}\,{}_2F_1\left(\frac{n+1}{2}, \frac{n+2}{2}; 2; \frac{A^2}{(d+A+h)^2}\right). \tag{A.9}$$

For large amplitudes $A \gg d+h$, the integrals above may be approximated in terms of the gamma function:[2]

$$\langle F_{\mathrm{ts}}\rangle(d) \approx -\frac{C}{\sqrt{2\pi}}(d+h)^{-n+\frac{1}{2}}A^{-\frac{1}{2}}\frac{\Gamma(n-\frac{1}{2})}{\Gamma(n)} \tag{A.10}$$

$$k_{\mathrm{ts}}(d) \approx C\sqrt{\frac{2}{\pi}}(d+h)^{-n+\frac{1}{2}}A^{-\frac{3}{2}}\frac{\Gamma(n-\frac{1}{2})}{\Gamma(n)}. \tag{A.11}$$

An equivalent expression for the force gradient (eq. (A.11)) is also given by Giessibl [10], and motivates the normalised frequency shift in frequency modulated AFM, $\gamma = kA^{3/2}\Delta f/f_0$. Similarly, a normalised force would be $\propto \sqrt{A}$.

With the wide range of values for $(d+h)/2A$, as required for fig. 3.1 in the main text, above approximations do not necessarily hold. For an estimate of the error, see fig. A.1. We therefore evaluate ${}_2F_1$ numerically for exact results.

1 Substitute $t = (d+h)y^2/2A$ and use the integral formula [33]

$${}_2F_1(a,b;c;z) = \frac{\Gamma(c)}{\Gamma(b)\Gamma(c-b)}\int_0^1 \mathrm{d}t\, t^{b-1}(1-t)^{c-b-1}(1-zt)^{-a}.$$

Equations (A.7) and (A.9) are obtained by applying the quadratic transformation formula 15.3.16 in Abramowitz & Stegun [33]. The latter step returns the argument of ${}_2F_1$ into the unit circle, such that an evaluation is possible in terms of its series definition

$${}_2F_1(a,b;c;z) = \sum_{k=0}^{\infty}\frac{(a)_k(b)_k}{(c)_k}\frac{z^k}{k!} \quad \text{for} \quad |z|<1.$$

2 Let $(d+h)/A \to 0$ and use $\int_0^1 \mathrm{d}x\, x^a(1-x)^b = \frac{\Gamma(a+1)\Gamma(b+1)}{\Gamma(a+b+2)}$ [167].

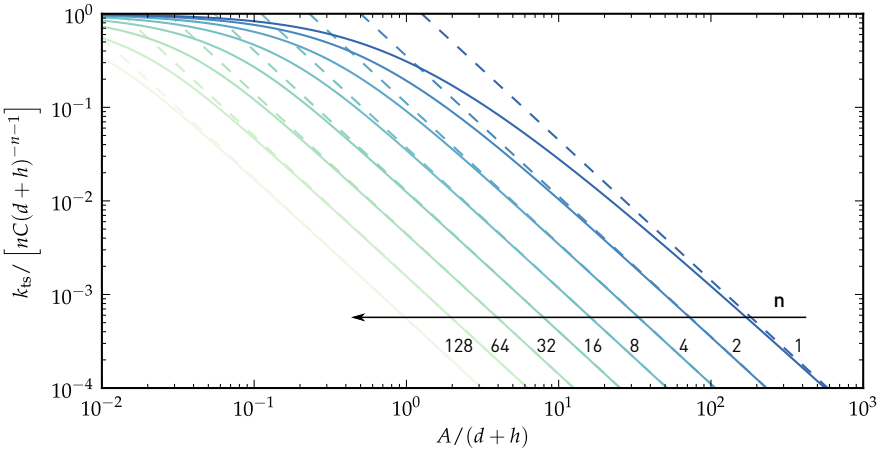

FIGURE A.1: Effective force gradient for an inverse power law, $F_{ts} = -C(z+h)^{-n}$, exact (solid, eq. (A.8)) and approximated for large amplitudes (dashed, eq. (A.11)) for different powers n. k_{ts} is normalised to the corresponding expression at vanishing oscillation amplitudes.

For a logarithmic law, $F_{ts}(z) = C\ln(z+h)$, we get

$$\langle F_{ts}\rangle(d) = C\ln(d+h) + 2C\ln\left[\frac{1}{2}\left(1+\sqrt{1+\frac{2A}{d+h}}\right)\right] \tag{A.12}$$

$$k_{ts}(d) = C(d+h)^{-1}{}_2F_1\left(\frac{3}{2},1;3;-\frac{2A}{d+h}\right) \tag{A.13}$$

$$= \frac{2C}{A}\left[1+\frac{d+h}{A}\left(1-\sqrt{1+\frac{2A}{d+h}}\right)\right]. \tag{A.14}$$

The total electrostatic force is $F_{el} = F_{apex} + F_{cone} + F_{lever}$. Since $F_{el} = C'U_{ts}^2/2$, the capacitance gradients C' and C'' follow straightforwardly from the expressions of the electrostatic forces and force gradients, respectively.

A.2 DERIVATION OF THE STATE-SPACE FM-KFM CONTROLLER

We have shown in section 3.6 that the sideband dynamics after lock-in detection can be modelled as a n-th order critically damped low-pass filter with the transfer

function $G(s) = K(1+\tau s)^{-n}$. In state space, the same system can be written as $\dot{\mathbf{x}}^\circ = \mathbf{A}^\circ\mathbf{x}^\circ + \mathbf{B}^\circ u^\circ$ and $y = \mathbf{C}^\circ\mathbf{x}^\circ$ with the input $u^\circ = U_{\mathrm{dc}} - U_{\mathrm{lcpd}}$ and the system matrices

$$\mathbf{A}^\circ = \frac{1}{\tau}\begin{pmatrix} -1 & 0 & \cdots & 0 \\ 1 & -1 & \cdots & 0 \\ \vdots & & \ddots & 0 \\ 0 & \cdots & 1 & -1 \end{pmatrix} \in \mathbb{R}^{n\times n}, \tag{A.15}$$

$$\mathbf{B}^\circ = \begin{pmatrix} \frac{1}{\tau} & 0 & \cdots & 0 \end{pmatrix}^\top \in \mathbb{R}^{n\times 1}, \text{ and} \tag{A.16}$$

$$\mathbf{C}^\circ = \begin{pmatrix} 0 & \cdots & 0 & K \end{pmatrix} \in \mathbb{R}^{1\times n}. \tag{A.17}$$

In this formulation, each element of the state vector $\mathbf{x}^\circ$ describes the input signal after each filter stage. By rewriting the system to include the surface potential as the *hidden* state $x_{n+1} = U_{\mathrm{lcpd}}$, the new system is $\dot{\mathbf{x}} = \mathbf{A}\mathbf{x} + \mathbf{B}u$, $y = \mathbf{C}\mathbf{x}$, with the input $u = U_{\mathrm{dc}}$ and the system matrices

$$\mathbf{A} = \begin{pmatrix} \mathbf{A}^\circ & \begin{matrix} -\frac{1}{\tau} \\ \vdots \\ 0 \end{matrix} \\ \mathbf{0} & 0 \end{pmatrix} \in \mathbb{R}^{n+1\times n+1}, \tag{A.18}$$

$$\mathbf{B} = \begin{pmatrix} \mathbf{B}^{\circ\top} & 0 \end{pmatrix}^\top \in \mathbb{R}^{n+1\times 1}, \text{ and} \tag{A.19}$$

$$\mathbf{C} = \begin{pmatrix} \mathbf{C}^\circ & 0 \end{pmatrix} \in \mathbb{R}^{1\times n+1}. \tag{A.20}$$

The task of finding the surface potential is therefore reduced to estimating the hidden state, U_{lcpd}, from the observation y.

We include measurement noise in the observations y and the uncertainty of the surface potential as white noise sources. Therefore

$$\dot{\mathbf{x}} = \mathbf{A}\mathbf{x} + \mathbf{B}u + v \tag{A.21}$$

$$y = \mathbf{C}\mathbf{x} + w, \tag{A.22}$$

where v and w are white noise processes with known spectral densities and covariance matrices $\mathbf{V}$ and $\mathbf{W}$, respectively.

An estimate of the state, $\hat{\mathbf{x}}$, is derived from the observations, y, using an observer: It uses the information about the dynamics of the state, modelled within the matrices $\mathbf{A}$ and $\mathbf{B}$, and adds to it a scaled version of the residual, $y - \mathbf{C}\hat{\mathbf{x}}$:

$$\dot{\hat{\mathbf{x}}} = \mathbf{A}\hat{\mathbf{x}} + \mathbf{B}u + \mathbf{L}(y - \mathbf{C}\hat{\mathbf{x}}), \tag{A.23}$$

where **L** is the filter gain. That is, knowledge about the system is used to derive a state estimate from measurements.

The optimum observer minimises the sum of the squared residuals over time. Given that in our case the system is perturbed by white noise, the optimum observer is the Kalman filter [82] with

$$\mathbf{L} = \mathbf{P}\mathbf{C}^\top \mathbf{W}^{-1}, \tag{A.24}$$

where **P** is the covariance matrix of the state estimate, which is found from the solution of the differential Riccati equation [78]

$$\dot{\mathbf{P}} = \mathbf{A}\mathbf{P} + \mathbf{P}\mathbf{A}^\top - \mathbf{P}\mathbf{C}^\top \mathbf{W}^{-1}\mathbf{C}\mathbf{P} + \mathbf{V}. \tag{A.25}$$

With $\dot{\mathbf{P}} = 0$, a steady-state solution can be found, allowing one to derive steady-state transfer functions and simplified state update equations.

A.3 RECONSTRUCTION OF VOLTAGE PROFILES

The quantity measured by KFM is the contact potential difference between the AFM tip and the surface underneath. But when analysing voltage profiles along a section that are induced by an externally applied voltage, voltages produced by charges trapped in a capping oxide layer or the difference in work function need to be removed for quantitative analysis.

Here, we show how the offset independent of the externally applied bias can be obtained from a set of voltage profiles at different bias. Such measurements thus only require line scans along e.g. a nanowire during a bias sweep.

Let us assume that the line profile $c(x, V)$ is a superposition of noise, an offset, $o(x)$, and a voltage-dependent potential value, $p(x, V)$:

$$c(x, V) = p(x, V) + o(x) \tag{A.26}$$

Assuming there are no negative differential resistances, the voltage is required to increase (decrease) along the profile for positive (negative) biases:

$$\frac{1}{V}\frac{\mathrm{d}}{\mathrm{d}x} p(x, V) > 0 \tag{A.27}$$

$$\frac{1}{V}\left(p(x + \Delta x, V) - p(x, V)\right) \geq 0 \tag{A.28}$$

We also require $p(0, V) = 0$. At the electrodes, the potential gradient should be zero, $\mathrm{d}/\mathrm{d}x\, p(x, V) = 0$, and the averaged offsets on both electrodes should be equal,

$\langle o(x \in \text{left electrode})\rangle = \langle o(x \in \text{right electrode})\rangle$. This ensures that the offset does not reduce the total voltage drop across the device.

Each $p(x, V)$ is decomposed into a power series:

$$p(x, V) = \alpha(x)V + \beta(x)V^2 + \gamma(x)V^3 + \dots \tag{A.29}$$

Discretising $p(x, V)$ yields the profile vector:

$$\mathbf{p}(V) = \begin{pmatrix} V\mathbf{I} & V^2\mathbf{I} & V^3\mathbf{I} & \dots \end{pmatrix} \begin{pmatrix} \alpha \\ \beta \\ \gamma \\ \vdots \end{pmatrix} = \mathbf{M}\,\mathbf{a} \tag{A.30}$$

For the line profile vector, we get:

$$\mathbf{c}(V) = \mathbf{p}(V) + \mathbf{o} = \begin{pmatrix} \mathbf{M} & \mathbf{I} \end{pmatrix} \begin{pmatrix} \mathbf{a} \\ \mathbf{o} \end{pmatrix} = \mathbf{A}\,\mathbf{x} \tag{A.31}$$

The condition of no negative differential resistances leads to

$$\frac{1}{V}(p_i(V) - p_{i+1}(V)) = \frac{1}{V}(\mathbf{M}_i - \mathbf{M}_{i+1})\,\mathbf{a} \le 0 \quad \forall V \tag{A.32}$$

$$\Leftrightarrow \quad \mathbf{C}\,\mathbf{a} \le 0, \tag{A.33}$$

where $\mathbf{M}_i$ denotes the i-th row of $\mathbf{M}$. With N_x samples per line, these are $N_x - 1$ conditions per voltage value. $\mathbf{C}$ is the resulting matrix of all conditions. The equality conditions are

$$\mathbf{M}_1\,\mathbf{a} = 0, \tag{A.34}$$

$$\mathbf{D}\,\mathbf{o} = 0, \tag{A.35}$$

$$(\mathbf{M}_i - \mathbf{M}_{i+1})\,\mathbf{a} = 0 \qquad \forall (i, i+1) \in \text{electrodes} \tag{A.36}$$

$$\Leftrightarrow \quad \mathbf{E}\,\mathbf{x} = \mathbf{b}. \tag{A.37}$$

Here, $\mathbf{D}$ is an operator that takes the difference of the average of all values on the left and right electrode.

We use the measured voltage profiles $\mathbf{y}(V)$ to perform a constrained least-squares optimisation:

$$\begin{aligned}
\text{min.} \quad & \frac{1}{2}\sum_V \left(\mathbf{c}(V) - \mathbf{y}(V)\right)^2 \\
& = \frac{1}{2}\mathbf{x}^\top \left(\sum_V \mathbf{A}^\top(V)\mathbf{A}(V)\right)\mathbf{x} - \left(\sum_V \mathbf{y}^\top(V)\mathbf{A}(V)\right)\mathbf{x} && \text{(A.38)} \\
\text{s.t.} \quad & \mathbf{C}\,\mathbf{a} \leq 0 && \text{(A.39)} \\
& \mathbf{E}\,\mathbf{x} = 0 && \text{(A.40)}
\end{aligned}$$

Weights $\sigma(x)$ can be incorporated as follows:

$$\begin{aligned}
& \mathbf{W} = \text{diag}(\sigma^2)^{-1} && \text{(A.41)} \\
\text{min.} \quad & \frac{1}{2}\mathbf{x}^\top \left(\sum_V \mathbf{A}^\top(V)\mathbf{W}\mathbf{A}(V)\right)\mathbf{x} - \left(\sum_V \mathbf{y}^\top(V)\mathbf{W}\mathbf{A}(V)\right)\mathbf{x} && \text{(A.42)} \\
\text{s.t.} \quad & \mathbf{C}\,\mathbf{a} \leq 0 && \text{(A.43)} \\
& \mathbf{E}\,\mathbf{x} = 0 && \text{(A.44)}
\end{aligned}$$

Model extension to asymmetric profiles

The above reconstruction works well when an applied voltage induces a voltage in the profile whose magnitude $|\mathbf{c}|$ only depends on $|V|$. We may however change the underlying model such that different coefficients $\mathbf{a}$ are used for positive and negative applied voltages: $\mathbf{a}_+$ and $\mathbf{a}_-$. Then,

$$\mathbf{p}'(V) = \begin{pmatrix}\mathbf{M}\,\delta_V & \mathbf{M}\,\delta_{-V}\end{pmatrix}\begin{pmatrix}\mathbf{a}_+ \\ \mathbf{a}_-\end{pmatrix} = \mathbf{M}'\,\mathbf{a}', \tag{A.45}$$

$$\mathbf{c}'(V) = \mathbf{p}'(V) + \mathbf{o} = \begin{pmatrix}\mathbf{M}' & \mathbf{I}\end{pmatrix}\begin{pmatrix}\mathbf{a}' \\ \mathbf{o}\end{pmatrix} = \mathbf{A}'\,\mathbf{x}'. \tag{A.46}$$

Similarly, the equality and inequality conditions are modified to match the partition of the $\mathbf{x}'$ vector.

Resistor model

$p(x, I)$ can alternatively be modelled as a linear chain of (non-linear) resistors. With U_k, the voltage before the k-th resistor, the voltage differences along the chain are

$$\Delta U_k = U_{k+1} - U_k = I\,R_k = \alpha_k I + \beta_k I^2 + \gamma_k I^3 + \ldots. \tag{A.47}$$

Thus, $U_k = \sum_{n=1}^{k-1} \Delta U_n$. Equivalently, a matrix equation for the profile, $\mathbf{p}$, is

$$\mathbf{p} = \mathbf{S}\,\Delta\mathbf{U} \tag{A.48}$$

$$= \begin{pmatrix} I\mathbf{S} & I^2\mathbf{S} & I^3\mathbf{S} & \dots \end{pmatrix} \begin{pmatrix} \alpha \\ \beta \\ \gamma \\ \vdots \end{pmatrix} = \mathbf{M}\,\mathbf{a}, \tag{A.49}$$

where $\mathbf{S}$ is a matrix producing the cumulative sum of the multiplied vector's elements[3].

Implementation

We have implemented the profile estimation algorithm outlined above for $p(x, V)$ based on a power series, eq. (A.29), and a linear chain of resistors. The constrained optimisation is performed using the quadratic program solver of CVXOPT [148].

3 That is, it is the $N_x \times N_x - 1$ matrix with a unity lower triangle and a zero main diagonal.

BIBLIOGRAPHY

1. Mohr, P., Taylor, B. & Newell, D. *2014 CODATA Recommended Values of the Fundamental Physical Constants* `http://physics.nist.gov/constants`. (Online; accessed 2015-11-26). 2015.
2. Wagner, T., Beyer, H., Reissner, P., Mensch, P., Riel, H., Gotsmann, B. & Stemmer, A. Kelvin probe force microscopy for local characterisation of active nanoelectronic devices. *Beilstein J. Nanotechnol.* **6**, 2193 (2015).
3. Binnig, G., Rohrer, H., Gerber, C. & Weibel, E. Tunneling through a controllable vacuum gap. *Appl. Phys. Lett.* **40**, 178 (1982).
4. Binnig, G., Rohrer, H., Gerber, C. & Weibel, E. Surface Studies by Scanning Tunneling Microscopy. *Phys. Rev. Lett.* **49**, 57 (1982).
5. Binnig, G., Rohrer, H., Gerber, C. & Weibel, E. 7×7 Reconstruction on Si(111) Resolved in Real Space. *Phys. Rev. Lett.* **50**, 120 (1983).
6. Binnig, G. & Rohrer, H. Scanning Tunneling Microscopy – From Birth To Adolescence. *Rev. Mod. Phys.* **59**, 615 (1987).
7. Binnig, G., Quate, C. & Gerber, C. Atomic force microscope. *Phys. Rev. Lett.* **56**, 930 (1986).
8. Giessibl, F. J. Atomic resolution on Si(111)-(7×7) by noncontact atomic force microscopy with a force sensor based on a quartz tuning fork. *Appl. Phys. Lett.* **76**, 1470 (2000).
9. Gross, L., Mohn, F., Moll, N., Liljeroth, P. & Meyer, G. The Chemical Structure of a Molecule Resolved by Atomic Force Microscopy. *Science* **325**, 1110 (2009).
10. Giessibl, F. J. Forces and frequency shifts in atomic-resolution dynamic-force microscopy. *Phys. Rev. B* **56**, 90128 (1997).
11. Göddenhenrich, T., Lemke, H., Hartmann, U. & Heiden, C. Force microscope with capacitive displacement detection. *J. Vac. Sci. Technol. A* **8**, 383 (1990).
12. Martin, Y., Williams, C. C. & Wickramasinghe, H. K. Atomic force microscope–force mapping and profiling on a sub 100-Å scale. *J. Appl. Phys.* **61**, 4723 (1987).
13. Meyer, G. & Amer, N. M. Novel optical approach to atomic force microscopy. *Appl. Phys. Lett.* **53**, 1045 (1988).

14. Giessibl, F. J., Pielmeier, F., Eguchi, T., An, T. & Hasegawa, Y. Comparison of force sensors for atomic force microscopy based on quartz tuning forks and length-extensional resonators. *Phys. Rev. B* **84**, 125409 (2011).

15. Schneiderbauer, M., Wastl, D. & Giessibl, F. J. qPlus magnetic force microscopy in frequency-modulation mode with millihertz resolution. *Beilstein J. Nanotechnol.* **3**, 174 (2012).

16. Mohn, F., Gross, L., Moll, N. & Meyer, G. Imaging the charge distribution within a single molecule. *Nat. Nanotechnol.* **7**, 227 (2012).

17. Lee, C., Wei, X., Kysar, J. W. & Hone, J. Measurement of the Elastic Properties and Intrinsic Strength of Monolayer Graphene. *Science* **321**, 385 (2008).

18. Güthner, P. & Dransfeld, K. Local poling of ferroelectric polymers by scanning force microscopy. *Appl. Phys. Lett.* **61**, 1137 (1992).

19. Martin, Y., Abraham, D. W. & Wickramasinghe, H. K. High-resolution capacitance measurement and potentiometry by force microscopy. *Appl. Phys. Lett.* **52**, 1103 (1988).

20. Nonnenmacher, M., O'Boyle, M. P. & Wickramasinghe, H. K. Kelvin probe force microscopy. *Appl. Phys. Lett.* **58**, 2921 (1991).

21. Martin, Y. & Wickramasinghe, H. K. Magnetic imaging by "force microscopy" with 1000 Å resolution. *Appl. Phys. Lett.* **50**, 1455 (1987).

22. Umeda, N., Ishizaki, S. & Uwai, H. Scanning attractive force microscope using photothermal vibration. *J. Vac. Sci. Technol. B* **9**, 1318 (1991).

23. Ratcliff, G. C., Erie, D. A. & Superfine, R. Photothermal modulation for oscillating mode atomic force microscopy in solution. *Appl. Phys. Lett.* **72**, 1911 (1998).

24. Giessibl, F. J. A direct method to calculate tip-sample forces from frequency shifts in frequency-modulation atomic force microscopy. *Appl. Phys. Lett.* **78**, 123 (2001).

25. Albrecht, T. R., Grütter, P., Horne, D. & Rugar, D. Frequency modulation detection using high-Q cantilevers for enhanced force microscope sensitivity. *J. Appl. Phys.* **69**, 668 (1991).

26. Garcıa, R. Dynamic atomic force microscopy methods. *Surf. Sci. Rep.* **47**, 197 (2002).

27. Paulo, Á. & Garcia, R. Unifying theory of tapping-mode atomic-force microscopy. *Phys. Rev. B* **66**, 041406 (2002).

28. Cleveland, J. P., Anczykowski, B., Schmid, A. E. & Elings, V. B. Energy dissipation in tapping-mode atomic force microscopy. *Appl. Phys. Lett.* **72**, 2613 (1998).

29. Anczykowski, B., Gotsmann, B., Fuchs, H., Cleveland, J. P. & Elings, V. B. How to measure energy dissipation in dynamic mode atomic force microscopy. *Appl. Surf. Sci.* **140**, 376 (1999).

30. Sader, J. E. & Jarvis, S. P. Accurate formulas for interaction force and energy in frequency modulation force spectroscopy. *Appl. Phys. Lett.* **84**, 1801 (2004).

31. Carlson, A. B. & Crilly, P. B. *Communication Systems* 5th ed. (McGraw Hill Higher Education, 2009).

32. Lübbe, J., Temmen, M., Rode, S., Rahe, P., Kühnle, A. & Reichling, M. Thermal noise limit for ultra-high vacuum noncontact atomic force microscopy. *Beilstein J. Nanotechnol.* **4**, 32 (2013).

33. Abramowitz, M. & Stegun, I. A. *Handbook of Mathematical Functions* (Dover New York, 1972).

34. Johnson, J. B. Thermal Agitation of Electricity in Conductors. *Phys. Rev.* **32**, 97 (1928).

35. Nyquist, H. Thermal Agitation of Electric Charge in Conductors. *Phys. Rev.* **32**, 110 (1928).

36. Schottky, W. Über spontane Stromschwankungen in verschiedenen Elektrizitätsleitern. *Ann. Phys. (Berlin)* **362**, 541 (1918).

37. Putman, C. A. J., de Grooth, B. G., van Hulst, N. F. & Greve, J. A theoretical comparison between interferometric and optical beam deflection technique for the measurement of cantilever displacement in AFM. *Ultramicroscopy* **42-44**, 1509 (1992).

38. Giessibl, F. J., Bielefeldt, H., Hembacher, S. & Mannhart, J. Calculation of the optimal imaging parameters for frequency modulation atomic force microscopy. *Appl. Surf. Sci.* **140**, 352 (1999).

39. Giessibl, F. J. Advances in atomic force microscopy. *Rev. Mod. Phys.* **75**, 949 (2003).

40. Dürig, U., Steinauer, H. R. & Blanc, N. Dynamic force microscopy by means of the phase-controlled oscillator method. *J. Appl. Phys.* **82**, 3641 (1997).

41. Kawai, S., Held, C. & Glatzel, T. *Nanonis Application Note: Automated amplitude calibration in non-contact AFM mode* (2009).

42. Sader, J. E., Chon, J. W. M. & Mulvaney, P. Calibration of rectangular atomic force microscope cantilevers. *Rev. Sci. Instrum.* **70**, 3967 (1999).

43. Sader, J. E., Sanelli, J. A., Adamson, B. D., Monty, J. P., Wei, X., Crawford, S. A., Friend, J. R., Marusic, I., Mulvaney, P. & Bieske, E. J. Spring constant calibration of atomic force microscope cantilevers of arbitrary shape. *Rev. Sci. Instrum.* **83**, 103705 (2012).

44. Weaver, J. M. R. & Abraham, D. W. High resolution atomic force microscopy potentiometry. *J. Vac. Sci. Technol. B* **9**, 1559 (1991).

45. Jacobs, H. O., Knapp, H. F. & Stemmer, A. Practical aspects of Kelvin probe force microscopy. *Rev. Sci. Instrum.* **70**, 1756 (1999).

46. Halpern, E., Cohen, G., Gross, S., Henning, A., Matok, M., Kretinin, A. V., Shtrikman, H. & Rosenwaks, Y. Measuring surface state density and energy distribution in InAs nanowires. *Phys. Status Solidi A* **211**, 473 (2014).

47. Koren, E., Berkovitch, N., Azriel, O., Boag, A., Rosenwaks, Y., Hemesath, E. R. & Lauhon, L. J. Direct measurement of nanowire Schottky junction depletion region. *Appl. Phys. Lett.* **99**, 3511 (2011).

48. Fuller, E. J., Pan, D., Corso, B. L., Gul, O. T. & Collins, P. G. Mean free paths in single-walled carbon nanotubes measured by Kelvin probe force microscopy. *Phys. Rev. B* **89**, 245450 (2014).

49. Ziegler, D., Gava, P., Guttinger, J., Molitor, F., Wirtz, L., Lazzeri, M., Saitta, A. M., Stemmer, A., Mauri, F. & Stampfer, C. Variations in the work function of doped single- and few-layer graphene assessed by Kelvin probe force microscopy and density functional theory. *Phys. Rev. B* **83**, 235434 (2011).

50. Wagner, T., Köhler, D., Milde, P. & Eng, L. M. Probing the local surface potential and quantum capacitance in single and multi-layer graphene. *Appl. Phys. Lett.* **103**, 3102 (2013).

51. Gross, L., Schuler, B., Mohn, F., Moll, N., Pavliček, N., Steurer, W., Scivetti, I., Kotsis, K., Persson, M. & Meyer, G. Investigating atomic contrast in atomic force microscopy and Kelvin probe force microscopy on ionic systems using functionalized tips. *Phys. Rev. B* **90**, 155455 (2014).

52. Kelvin, L. Contact Electricity of Metals. *Philos. Mag.* **46**, 82 (1898).

53. Kantorovich, L. N., Livshits, A. I. & Stoneham, M. Electrostatic energy calculation for the interpretation of scanning probe microscopy experiments. *J. Phys.: Condens. Matter* **12**, 795 (2000).

54. Kitamura, S. & Iwatsuki, M. High-resolution imaging of contact potential difference with ultrahigh vacuum noncontact atomic force microscope. *Appl. Phys. Lett.* **72**, 3154 (1998).

55. Jacobs, H. O., Leuchtmann, P., Homan, O. J. & Stemmer, A. Resolution and contrast in Kelvin probe force microscopy. *J. Appl. Phys.* **84**, 1168 (1998).

56. Ziegler, D. & Stemmer, A. Force gradient sensitive detection in lift-mode Kelvin probe force microscopy. *Nanotechnology* **22**, 075501 (2011).

57. Strassburg, E., Boag, A. & Rosenwaks, Y. Reconstruction of electrostatic force microscopy images. *Rev. Sci. Instrum.* **76**, 083705–083705 (2005).

58. Cohen, G., Halpern, E., Nanayakkara, S. U., Luther, J. M., Held, C., Bennewitz, R., Boag, A. & Rosenwaks, Y. Reconstruction of surface potential from Kelvin probe force microscopy images. *Nanotechnology* **24**, 295702 (2013).

59. Sadewasser, S. & Lux-Steiner, M. C. Correct Height Measurement in Noncontact Atomic Force Microscopy. *Phys. Rev. Lett.* **91**, 266101 (2003).

60. Ziegler, D., Rychen, J., Naujoks, N. & Stemmer, A. Compensating electrostatic forces by single-scan Kelvin probe force microscopy. *Nanotechnology* **18**, 5505 (2007).

61. Kitamura, S., Suzuki, K. & Iwatsuki, M. High resolution imaging of contact potential difference using a novel ultrahigh vacuum non-contact atomic force microscope technique. *Appl. Surf. Sci.* **140**, 265 (1999).

62. Hudlet, S., Saint Jean, M., Guthmann, C. & Berger, J. Evaluation of the capacitive force between an atomic force microscopy tip and a metallic surface. *Eur. Phys. J. B* **2**, 5 (1998).

63. Diesinger, H., Deresmes, D. & Mélin, T. Noise performance of frequency modulation Kelvin force microscopy. *Beilstein J. Nanotechnol.* **5**, 1 (2014).

64. Zerweck, U., Loppacher, C., Otto, T., Grafström, S. & Eng, L. M. Accuracy and resolution limits of Kelvin probe force microscopy. *Phys. Rev. B* **71**, 125424 (2005).

65. Barbet, S., Popoff, M., Diesinger, H., Deresmes, D., Théron, D. & Mélin, T. Cross-talk artefacts in Kelvin probe force microscopy imaging: A comprehensive study. *J. Appl. Phys.* **115**, 144313 (2014).

66. Abraham, D. W., Williams, C., Slinkman, J. & Wickramasinghe, H. K. Lateral dopant profiling in semiconductors by force microscopy using capacitive detection. *J. Vac. Sci. Technol. B* **9**, 703 (1991).

67. Enning, R. *High Frequency Atomic Force Microscopy* PhD thesis (ETH Zürich, 2011).

68. Enning, R., Ziegler, D., Nievergelt, A., Friedlos, R., Venkataramani, K. & Stemmer, A. A high frequency sensor for optical beam deflection atomic force microscopy. *Rev. Sci. Instrum.* **82**, 043705–043705 (2011).

69. Kou, L., Ma, Z., Li, Y. J., Naitoh, Y., Komiyama, M. & Sugawara, Y. Surface potential imaging with atomic resolution by frequency-modulation Kelvin probe force microscopy without bias voltage feedback. *Nanotechnology* **26**, 195701 (2015).

70. Sadewasser, S., Carl, P., Glatzel, T. & Lux-Steiner, M. C. Influence of uncompensated electrostatic force on height measurements in non-contact atomic force microscopy. *Nanotechnology* **15**, S14 (2004).

71. Ziegler, D., Naujoks, N. & Stemmer, A. Feed-forward compensation of surface potential in atomic force microscopy. *Rev. Sci. Instrum.* **79**, 3704 (2008).

72. Efimov, A. & Cohen, S. R. Simulation and correction of geometric distortions in scanning Kelvin probe microscopy. *J. Vac. Sci. Technol. A* **18**, 1051 (2000).

73. *Kelvin Probe Force Microscopy* (eds Sadewasser, S. & Glatzel, T.) (Springer, 2012).

74. Polak, L., de Man, S. & Wijngaarden, R. J. Note: Switching crosstalk on and off in Kelvin probe force microscopy. *Rev. Sci. Instrum.* **85**, 046111 (2014).

75. Lee, M., Lee, W. & Prinz, F. B. Geometric artefact suppressed surface potential measurements. *Nanotechnology* **17**, 3728 (2006).

76. Ziegler, J. G. & Nichols, N. B. Optimum settings for automatic controllers. *Trans. ASME* **64**, 759 (1942).

77. Bechhoefer, J. Feedback for physicists: A tutorial essay on control. *Rev. Mod. Phys.* **77**, 783 (2005).

78. Friedland, B. *Control System Design: An Introduction to State-Space Methods* (Dover, 2005).

79. Degen, C. L., Meier, U., Lin, Q., Hunkeler, A. & Meier, B. H. Digital feedback controller for force microscope cantilevers. *Rev. Sci. Instrum.* **77**, 043707 (2006).

80. Schitter, G., Menold, P., Knapp, H. F., Allgöwer, F. & Stemmer, A. High performance feedback for fast scanning atomic force microscopes. *Rev. Sci. Instrum.* **72**, 3320 (2001).

81. Kalman, R. E. A new approach to linear filtering and prediction problems. *J. Basic Eng.* **82**, 35 (1960).

82. Kalman, R. E. & Bucy, R. S. New Results in Linear Filtering and Prediction Theory. *J. Basic Eng.* **83**, 95 (1961).

83. Simon, D. *Optimal State Estimation* 1st ed. (Wiley-Interscience, 2006).

84. Guennebaud, G., Jacob, B., *et al. Eigen v3* <http://eigen.tuxfamily.org> (2010).

85. Sulchek, T., Hsieh, R., Adams, J. D., Yaralioglu, G. G., Minne, S. C., Quate, C. F., Cleveland, J. P., Atalar, A. & Adderton, D. M. High-speed tapping mode imaging with active Q control for atomic force microscopy. *Appl. Phys. Lett.* **76**, 1473 (2000).

86. Hölscher, H. & Schwarz, U. D. Theory of amplitude modulation atomic force microscopy with and without Q-Control. *Internat. J. Nonlin. Mech.* **42**, 608 (2007).

87. Sugawara, Y., Kou, L., Ma, Z., Kamijo, T., Naitoh, Y. & Jun Li, Y. High potential sensitivity in heterodyne amplitude-modulation Kelvin probe force microscopy. *Appl. Phys. Lett.* **100**, 3104 (2012).

88. Magonov, S. & Alexander, J. Single-pass Kelvin force microscopy and dC/dZ measurements in the intermittent contact: applications to polymer materials. *Beilstein J. Nanotechnol.* **2**, 15 (2011).

89. Halpern, E., Henning, A., Shtrikman, H., Rurali, R., Cartoixà, X. & Rosenwaks, Y. Room Temperature Observation of Quantum Confinement in Single InAs Nanowires. *Nano Lett.* **15**, 481 (2014).

90. Quitoriano, N. J., Sanderson, R. N., Bae, S.-S. & Ragan, R. Interpreting Kelvin probe force microscopy under an applied electric field: local electronic behavior of vapor–liquid–solid Si nanowires. *Nanotechnology* **24**, 205704 (2013).

91. Fuller, E. J., Pan, D., Corso, B. L., Tolga Gul, O., Gomez, J. R. & Collins, P. G. Quantitative Kelvin probe force microscopy of current-carrying devices. *Appl. Phys. Lett.* **102**, 083503 (2013).

92. Ihn, T. *Semiconductor Nanostructures* (Oxford University Press, Oxford, 2010).

93. Datta, S. *Electronic Transport in Mesoscopic Systems* (Cambridge University Press, Cambridge, 1995).

94. Robinett, R. W. Quantum mechanics of the two-dimensional circular billiard plus baffle system and half-integral angular momentum. *Eur. J. Phys.* **24**, 231 (2003).

95. Mensch, P. *Thermoelectric Characterization of InAs Nanowires* PhD thesis (ETH Zürich, 2015).

96. Cuevas, J. C. & Scheer, E. *Molecular Electronics: An Introduction to Theory and Experiment* (World Scientific, Singapore, 2010).

97. Menges, F., Riel, H., Stemmer, A. & Gotsmann, B. Quantitative Thermometry of Nanoscale Hot Spots. *Nano Lett.* **12**, 596 (2012).

98. Menges, F. *Scanning Probe Thermometry of Nanosystems* PhD thesis (ETH Zürich, 2015).

99. Aviram, A. & Ratner, M. A. Molecular rectifiers. *Chem. Phys. Lett.* **29**, 277 (1974).

100. Cui, X. D., Primak, A., Zarate, X., Tomfohr, J., Sankey, O. F., Moore, A. L., Moore, T. A., Gust, D., Harris, G. & Lindsay, S. M. Reproducible measurement of single-molecule conductivity. *Science* **294**, 571 (2001).

101. Joachim, C. & Gimzewski, J. K. An electromechanical amplifier using a single molecule. *Chem. Phys. Lett.* **265**, 353 (1997).

102. Zabet-Khosousi, A. & Dhirani, A.-A. Charge Transport in Nanoparticle Assemblies. *Chem. Rev.* **108**, 4072 (2008).

103. Liao, J., Blok, S., van der Molen, S. J., Diefenbach, S., Holleitner, A. W., Schönenberger, C., Vladyka, A. & Calame, M. Ordered nanoparticle arrays interconnected by molecular linkers: electronic and optoelectronic properties. *Chem. Soc. Rev.* (2014).

104. Parthasarathy, R., Lin, X.-M. & Jaeger, H. Electronic Transport in Metal Nanocrystal Arrays: The Effect of Structural Disorder on Scaling Behavior. *Phys. Rev. Lett.* **87**, 186807 (2001).

105. Liao, J., Bernard, L., Langer, M., Schönenberger, C. & Calame, M. Reversible Formation of Molecular Junctions in 2D Nanoparticle Arrays. *Adv. Mater.* **18**, 2444 (2006).

106. Blunt, M. O., Suvakov, M., Pulizzi, F., Martin, C. P., Pauliac-Vaujour, E., Stannard, A., Rushforth, A. W., Tadić, B. & Moriarty, P. Charge transport in cellular nanoparticle networks: Meandering through nanoscale mazes. *Nano Lett.* **7**, 855 (2007).

107. Slot, J. W. & Geuze, H. J. A new method of preparing gold probes for multiple-labeling cytochemistry. *Eur. J. Cell Biol.* **38**, 87 (1985).

108. Huang, S., Tsutsui, G., Sakaue, H., Shingubara, S. & Takahagi, T. Formation of a large-scale Langmuir–Blodgett monolayer of alkanethiol-encapsulated gold particles. *J. Vac. Sci. Technol. B* **19**, 115 (2001).

109. Santhanam, V., Liu, J., Agarwal, R. & Andres, R. P. Self-Assembly of Uniform Monolayer Arrays of Nanoparticles. *Langmuir* **19**, 7881 (2003).

110. Santhanam, V. & Andres, R. P. Microcontact Printing of Uniform Nanoparticle Arrays. *Nano Lett.* **4**, 41 (2004).

111. Ruiz-Vargas, C. S., Reissner, P. A., Wagner, T., Wyss, R. M., Park, H. G. & Stemmer, A. Contact transfer length investigation of a 2D nanoparticle network by scanning probe microscopy. *Nanotechnology* **26**, 365701 (2015).

112. Chen, C. J. *Introduction to Scanning Tunneling Microscopy* (Oxford University Press, New York, 1993).

113. Lekner. Capacitance coefficients of two spheres. *J. Electrostat.* **69**, 4 (2011).

114. Rampi, M. A., Schueller, O. J. A. & Whitesides, G. M. Alkanethiol self-assembled monolayers as the dielectric of capacitors with nanoscale thickness. *Appl. Phys. Lett.* **72**, 1781 (1998).

115. Middleton, A. & Wingreen, N. Collective transport in arrays of small metallic dots. *Phys. Rev. Lett.* **71**, 3198 (1993).

116. Suvakov, M. & Tadić, B. Modeling collective charge transport in nanoparticle assemblies. *J. Phys.: Condens. Matter* **22**, 163201 (2010).

117. Parthasarathy, R., Lin, X.-M., Elteto, K., Rosenbaum, T. F. & Jaeger, H. M. Percolating through Networks of Random Thresholds: Finite Temperature Electron Tunneling in Metal Nanocrystal Arrays. *Phys. Rev. Lett.* **92**, 076801 (2004).

118. Elteto, K., Antonyan, E., Nguyen, T. & Jaeger, H. Model for the onset of transport in systems with distributed thresholds for conduction. *Phys. Rev. B* **71**, 064206 (2005).

119. Peixoto, T. P. *The graph-tool python library* `http://graph-tool.skewed.de/`. (Online; accessed 2015-12-31). 2014.

120. Jones, E., Oliphant, T., Peterson, P., *et al. SciPy: Open source scientific tools for Python* `http://www.scipy.org/`. (Online; accessed 2015-12-31). 2001–.

121. Stauffer, D. & Aharony, A. *Introduction to Percolation Theory* (Taylor & Francis, 1994).

122. Hausdorff, F. Dimension und äußeres Maß. *Math. Ann.* **79**, 157 (1918).

123. Mandelbrot, B. How Long Is the Coast of Britain? Statistical Self-Similarity and Fractional Dimension. *Science* **156**, 636 (1967).

124. Last, B. J. & Thouless, D. J. Percolation Theory and Electrical Conductivity. *Phys. Rev. Lett.* **27**, 1719 (1971).

125. Normand, J. M., Herrmann, H. J. & Hajjar, M. Precise calculation of the dynamical exponent of two-dimensional percolation. *J. Stat. Phys.* **52**, 441 (1988).

126. Sykes, M. F. & Essam, J. W. Exact Critical Percolation Probabilities for Site and Bond Problems in Two Dimensions. *J. Math. Phys.* **5**, 1117 (1964).

127. Kirkpatrick, S. Percolation and Conduction. *Rev. Mod. Phys.* **45**, 574 (1973).

128. Straley, J. P. The ant in the labyrinth: diffusion in random networks near the percolation threshold. *J. Phys. C: Solid State Phys.* **13**, 2991 (1980).

129. Redner, S. *Fractal and Multifractal Scaling of Electrical Conduction in Random Resistor Networks* in *Encyclopedia of Complexity and Systems Science* 3737 (Springer New York, New York, NY, 2009).

130. Stanley, H. E. Cluster shapes at the percolation threshold: and effective cluster dimensionality and its connection with critical-point exponents. *J. Phys. A: Math. Gen.* **10**, L211 (1977).

131. Coniglio, A. Cluster structure near the percolation threshold. *J. Phys. A: Math. Gen.* **15**, 3829 (1982).

132. Herrmann, H. J. & Stanley, H. E. The fractal dimension of the minimum path in two- and three-dimensional percolation. *J. Phys. A: Math. Gen.* **21**, L829 (1988).

133. Grassberger, P. Spreading and backbone dimensions of 2D percolation. *J. Phys. A: Math. Gen.* **25**, 5475 (1992).

134. Tyč, S. & Halperin, B. I. Random resistor network with an exponentially wide distribution of bond conductances. *Phys. Rev. B* **39**, 877 (1989).

135. Roux, S. & Herrmann, H. J. Disorder-Induced Nonlinear Conductivity. *EPL* **4**, 1227 (1987).

136. De Arcangelis, L., Redner, S. & Herrmann, H. J. A random fuse model for breaking processes. *J. Phyique Lett.* **46**, 585 (1985).

137. Cheianov, V. V., Fal'Ko, V. I., Altshuler, B. L. & Aleiner, I. L. Random resistor network model of minimal conductivity in graphene. *Phys. Rev. Lett.* **99** (2007).

138. Murawski, J., Graupner, T., Milde, P., Raupach, R., Zerweck-Trogisch, U. & Eng, L. M. Pump-probe Kelvin-probe force microscopy: Principle of operation and resolution limits. *J. Appl. Phys.* **118**, 154302 (2015).

139. Coffey, D. C. & Ginger, D. S. Time-resolved electrostatic force microscopy of polymer solar cells. *Nat. Mater.* **5**, 735 (2006).

140. Giridharagopal, R., Rayermann, G. E., Shao, G., Moore, D. T., Reid, O. G., Tillack, A. F., Masiello, D. J. & Ginger, D. S. Submicrosecond Time Resolution Atomic Force Microscopy for Probing Nanoscale Dynamics. *Nano Lett.* **12**, 893 (2012).

141. Yao, J., Zhong, L., Natelson, D. & Tour, J. M. Silicon Oxide: A Non-innocent Surface for Molecular Electronics and Nanoelectronics Studies. *J. Am. Chem. Soc.* **133**, 941 (2011).

142. Berger, H. H. Models for contacts to planar devices. *Solid-State Electron.* **15**, 145 (1972).

143. Hostetler, M. J., Templeton, A. C. & Murray, R. W. Dynamics of Place-Exchange Reactions on Monolayer-Protected Gold Cluster Molecules. *Langmuir* **15**, 3782 (1999).

144. Bernard, L., Kamdzhilov, Y., Calame, M., van der Molen, S. J., Liao, J. & Schönenberger, C. Spectroscopy of Molecular Junction Networks Obtained by Place Exchange in 2D Nanoparticle Arrays. *J. Phys. Chem. C* **111**, 18445 (2007).

145. Luo, L., Choi, S. H. & Frisbie, C. D. Probing Hopping Conduction in Conjugated Molecular Wires Connected to Metal Electrodes. *Chem. Mater.* **23**, 631 (2011).

146. Liao, J., Mangold, M. A., Grunder, S., Mayor, M., Schönenberger, C. & Calame, M. Interlinking Au nanoparticles in 2D arrays via conjugated dithiolated molecules. *New J. Phys.* **10**, 5019 (2008).

147. Mangold, M. A., Calame, M., Mayor, M. & Holleitner, A. W. Negative Differential Photoconductance in Gold Nanoparticle Arrays in the Coulomb Blockade Regime. *ACS Nano* **6**, 4181 (2012).

148. Andersen, M. S., Dahl, J. & Vandenberghe, L. *CVXOPT: A Python package for convex optimization, version 1.1.7* <http://cvxopt.org/> (2014).

149. Halgren, T. A. Merck molecular force field. I. Basis, form, scope, parameterization, and performance of MMFF94. *J. Comput. Chem.* **17**, 490 (1996).

150. Wu, S., González, M. T., Huber, R., Grunder, S., Mayor, M., Schönenberger, C. & Calame, M. Molecular junctions based on aromatic coupling. *Nat. Nanotechnol.* **3**, 569 (2008).

151. Hassenkam, T., Moth-Poulsen, K., Stuhr-Hansen, N., Nørgaard, K., Kabir, M. S. & Bjørnholm, T. Self-Assembly and Conductive Properties of Molecularly Linked Gold Nanowires. *Nano Lett.* **4**, 19 (2004).

152. Kronemeijer, A. J., Huisman, E. H., Akkerman, H. B., Goossens, A. M., Katsouras, I., van Hal, P. A., Geuns, T. C. T., van der Molen, S. J., Blom, P. W. M. & de Leeuw, D. M. Electrical characteristics of conjugated self-assembled monolayers in large-area molecular junctions. *Appl. Phys. Lett.* **97**, 173302 (2010).

153. Neubeck, S., Freitag, F., Yang, R. & Novoselov, K. Scanning probe lithography on graphene. *Phys. Status Solidi B* **247**, 2904 (2010).

154. Scharnetzky, J. *Graphene/graphene oxide junctions as test beds for local conductivity measurements of interlinked nanoparticle networks with Kelvin probe force microscopy* MA thesis (ETH Zürich, 2015).

155. Shipway, A. N., Katz, E. & Willner, I. Nanoparticle arrays on surfaces for electronic, optical, and sensor applications. *ChemPhysChem* **1**, 18 (2000).

156. Saha, K., Agasti, S. S., Kim, C., Li, X. & Rotello, V. M. Gold Nanoparticles in Chemical and Biological Sensing. *Chem. Rev.* **112**, 2739 (2012).

157. Hu, Z., Fischbein, M. D. & Drndić, M. Local Charge Transport in Two-Dimensional PbSe Nanocrystal Arrays Studied by Electrostatic Force Microscopy. *Nano Lett.* **5**, 1463 (2005).

158. Fischbein, M. D., Puster, M. & Drndić, M. Monolayer Suppression of Transport Imaged in Annealed PbSe Nanocrystal Arrays. *Nano Lett.* **10**, 2155 (2010).

159. Lei, C. H., Das, A., Elliott, M. & Macdonald, J. E. Conductivity of macromolecular networks measured by electrostatic force microscopy. *Appl. Phys. Lett.* **83**, 482 (2003).

160. Bobbert, P. A., Sharma, A., Mathijssen, S. G. J., Kemerink, M. & de Leeuw, D. M. Operational Stability of Organic Field-Effect Transistors. *Adv. Mater.* **24**, 1146 (2012).

161. Nonnenmacher, M., O'Boyle, M. & Wickramasinghe, H. K. Surface investigations with a Kelvin probe force microscope. *Ultramicroscopy* **42**, 268 (1992).

162. Nakagiri, N., Sugimura, H., Ishida, Y., Hayashi, K. & Takai, O. Effects of an adsorbed water layer and self-assembled organosilane monolayers on scanning probe microscopy of silicon pn structures. *Surf. Sci.* **532-535**, 999 (2003).

163. Saleh, B. E. A. & Teich, M. C. *Fundamentals of Photonics* (Wiley, New York, 1991).

164. Putman, C. A. J., De Grooth, B. G., Van Hulst, N. F. & Greve, J. A Detailed Analysis of the Optical Beam Deflection Technique for Use in Atomic Force Microscopy. *J. Appl. Phys.* **72**, 6 (1992).

165. Lübbe, J., Tröger, L., Torbrügge, S., Bechstein, R., Richter, C., Kühnle, A. & Reichling, M. Achieving high effective Q-factors in ultra-high vacuum dynamic force microscopy. *Meas. Sci. Technol.* **21**, 125501 (2010).

166. Tisserant, J.-N., Reissner, P. A., Jenatsch, S., Beyer, H., Hany, R. & Stemmer, A. Interfacial self-assembly of nanoporous C60 thin films. *RSC Adv.* **6**, 23141 (2016).

167. Bronstein, I. N., Semendjaew, K. A., Grosche, G., Ziegler, V. & Ziegler, D. *Springer-Taschenbuch der Mathematik* 3rd ed. (ed Zeidler, E.) (Springer Fachmedien Wiesbaden, Wiesbaden, 2013).

CURRICULUM VITAE

PERSONAL DATA

Name	Tino Wagner
Date of Birth	October 6, 1986
Place of Birth	Lichtenstein, Germany
Citizen of	Germany

EDUCATION

February 2012 – January 2016	PhD candidate at the Chair of Nanotechnology, *Department of Mechanical and Process Engineering* *ETH Zürich*, Zürich, Switzerland
October 2006 – January 2012	Undergraduate and graduate studies in Physics, *Dresden University of Technology*, Dresden, Germany *Final degree:* Dipl.-Phys.
July 2005	Grammar school "Prof. Dr. Max Schneider" Lichtenstein, Germany *Final degree:* Abitur

EMPLOYMENT

May 2010 – September 2010	Internship; Research on gas sensors for fire detection *Siemens AG, Building Technologies Division*, Zug, Switzerland
July 2005 – March 2006	Civilian service *PKP Seniorenbetreuung GmbH*, Hohenstein-Ernstthal, Germany

PUBLICATIONS

Articles in peer-reviewed journals:

1. Beyer, H., Wagner, T. & Stemmer, A. Length-extension resonator as a force sensor for high-resolution frequency-modulation atomic force microscopy in air. *Beilstein J. Nanotechnol.* **7**, 432 (2016).
2. Wagner, T., Beyer, H., Reissner, P., Mensch, P., Riel, H., Gotsmann, B. & Stemmer, A. Kelvin probe force microscopy for local characterisation of active nanoelectronic devices. *Beilstein J. Nanotechnol.* **6**, 2193 (2015).
3. Ruiz-Vargas, C. S., Reissner, P. A., Wagner, T., Wyss, R. M., Park, H. G. & Stemmer, A. Contact transfer length investigation of a 2D nanoparticle network by scanning probe microscopy. *Nanotechnology* **26**, 365701 (2015).
4. Wagner, T., Köhler, D., Milde, P. & Eng, L. M. Probing the local surface potential and quantum capacitance in single and multi-layer graphene. *Appl. Phys. Lett.* **103**, 023102 (2013).

Poster contributions to conferences:

5. Wagner, T., Tian, J.-H., Kaja, K. & Stemmer, A. *Imaging source-drain potential in arrays of linked gold nanoparticles* in *ElecMol* Dec. 3–7, 2012 (6th International Meeting on Molecular Electronics, Grenoble, France).
6. Wagner, T., Tian, J.-H., Reissner, P., Ruiz-Vargas, C. & Stemmer, A. *Imaging local charge transport in arrays of linked gold nanoparticles* in *ECME* Sept. 3–7, 2013 (12th European Conference on Molecular Electronics, London, United Kingdom).
7. Wagner, T., Tian, J.-H., Ruiz-Vargas, C., Gotsmann, B. & Stemmer, A. *Kelvin probe force microscopy for local characterisation of active nanoelectronic devices* in *ElecMol* Aug. 24–29, 2014 (7th International Conference on Molecular Electronics, Strasbourg, France).
8. Wagner, T., Reissner, P., Ruiz-Vargas, C. & Stemmer, A. *Frequency modulated Kelvin probe force microscopy on active devices* in *ncAFM* Sept. 7–11, 2015 (18th International Conference on non-contact Atomic Force Microscopy, Cassis, France).